A STUDY OF TURBULENT AND IONIZED MATERIAL IN THE CIRCUMGALACTIC MEDIUM

by

CHEN WANG

(Under the Direction of Robin Shelton)

This dissertation investigates gas surrounding galaxies. We started by running hydrodynamic simulations with the FLASH computational code. We modeled how cold, dense clouds mix with hot, diffuse ambient material, using a variety of initial parameters based on observations. Then, we developed a method to calculate the amount of material in observed clouds, from the observed O VI column density and our calculated O VI ionization fraction. We found that the O VI ionization fraction calculated with our non-equilibrium ionization methodology is much lower than that found from the standard approximation, which is the peak value from a collisional ionization equilibrium model. The lower O VI ionization fraction suggests that the clouds contain a higher amount of material than existing estimates. In addition, the simulations show that O VI exists in a wider temperature range than expected from the standard approximation. To further study the wide distribution of O VI over the temperature range, we examined spectra from our simulated clouds. We created synthetic O VI absorption spectra, from which we derived the Doppler broadening parameters (b values). We found a large fraction of relatively small b values, which implies a substantial amount of O VI in cool gas. This result is consistent with our earlier finding of O VI in cool regions. We also extended our analysis of ionization fractions by adding carbon and silicon to our simulations and found that the CIV and SiIV ionization fractions are also much lower

than determined from the standard approximation. During this process, we also studied O VI emission from the edge region of starburst galaxies.

INDEX WORDS: High-velocity clouds, Intergalactic Clouds, Hydrodynamic simulations,
Intergalactic Medium, Circumgalactic Medium

A STUDY OF TURBULENT AND IONIZED MATERIAL IN THE CIRCUMGALACTIC MEDIUM

by

CHEN WANG

B.S., University of California, Irvine, 2019

A Dissertation to be submitted to the Graduate Faculty of the University of Georgia in Partial Fulfillment of the Requirements for the Degree.

Doctor of Philosophy

ATHENS, GEORGIA

©2025 Chen Wang

All Rights Reserved

A STUDY OF TURBULENT AND IONIZED MATERIAL IN THE CIRCUMGALACTIC MEDIUM

by

CHEN WANG

Major Professor: Robin Shelton

Committee: Loris Magnani

Michael Geller

Electronic Version Approved:

Ron Walcott

Dean of the Graduate School

The University of Georgia

August 2025

DEDICATION

For my family, who have always been my greatest supporters. Your love, understanding, and support are the constant motivation that inspires me to always go forward.

ACKNOWLEDGMENTS

I would first like to express my deepest gratitude to my major advisor, Dr. Robin Shelton. Throughout my six-year Ph.D. journey at the University of Georgia, her guidance has been invaluable. With immense patience, she helped me establish my research program from the very beginning, guiding me step by step. Her precious advice was very important in my development, not only as a student but also as a researcher. I am profoundly thankful for her mentorship and unwavering support.

I extend my sincere thanks to the other members of my advisory committee, Dr. Loris Magnani and Dr. Michael Geller, for their insightful feedback and encouragement throughout this process.

My thanks go to several other individuals whose collaboration and support were critical to my work. I am grateful to Eric Goetz for his help and cooperation throughout my entire Ph.D. program. I would also like to acknowledge M. Elliott Williams for his detailed assistance and instruction on setting up and running the hydrodynamic simulations, which became the foundation for the projects in this dissertation. My appreciation also goes to Ashton Rutkowski for coding analysis, which was helpful as I began my research, and to Sydney Whilden for the conversations we had regarding my first project.

I am also very grateful for the excellent technical support I received. I would particularly like to thank Dr. Shan-ho Tsai for her expert assistance with the Georgia Advanced Computing Resource Center (GACRC). Her patient explanations of essential skills for High Performance Computing on the Sapelo2 cluster were incredibly valuable, and I deeply appreciate her guidance.

I would like to extend my sincere gratitude to the Flash Center for Computational Science, based at the University of Rochester, for giving me permission to use the FLASH software in this research. The development of this code at the Center is made possible through the support of the U.S. Department of Energy and the National Science Foundation.

Finally, I am grateful to the University of Georgia Graduate School and the Department of Physics and Astronomy for providing the teaching assistantship and travel funding that allowed me to complete my research and to present my work at several academic conferences.

Contents

A	cknow	ledgments	v
Li	st of l	Figures	ix
Li	st of '	Tables	xv
I	Intr	oduction	1
2	Unv	eiling the Hidden Mass Associated with Observed O VI in Intergalactic and Circum-	-
	gala	ctic High Velocity Clouds	5
	2. I	Introduction	7
	2.2	Methods	9
	2.3	Results	14
	2.4	Discussion	24
	2.5	Author Contributions	27
3	Den	nystifying Strange O VI Line Widths with Hydrodynamic Simulations	31
	3. I	Introduction	33
	3.2	Model	34
	3.3	Results	36
	3.4	Discussion	47
	3.5	Summary	5 1

		iography				
A	Fitti	ing and Estimated Results for Run 2 to Run 10	85			
6	Con	clusion	83			
	5.5	Author Contributions	79			
	5.4	Discussion	79			
	5.3	Results	75			
	5.2	Observation	73			
	5.1	Introduction	71			
5	The	O VI Emission from the Extended Disk of NGC 1068	69			
	4.5	Author Contributions	56			
	4.4	Discussion	55			
	4.3	Results	55			
	4.2	Methods	55			
	4.I	Introduction	54			
	Velo	city Clouds	52			
4	A St	rudy of C IV and Si IV Ions Distributed Over a Wide Temperature Range in High	1			
	3.6	Author Contributions	51			
	26	Author Contributions	CT			

LIST OF FIGURES

2. I	Hydrogen column density plots for Run 1 at 5 epochs (0, 50, 100, 150, and 200 Myr). The	
	column densities are calculated by integrating the hydrogen number density along sight	
	lines directed into the page. These sight lines are in the \hat{y} direction, which is the direction	
	in which only half the cloud was simulated. So, we have multiplied the column densities	
	by 2 to account for having simulated only 1/2 of the cloud. The ambient gas moves to	
	the right, interacting with the cloud gas. The resulting tail formation and hydrodynamic	
	instabilities are apparent in this figure	19
2.2	Hydrogen column density plots for Run 1 at 5 epochs (0, 50, 100, 150, and 200 Myr) for	
	material whose velocity in the \hat{z} direction differs by more than 100 km s $^{-1}$ from that of	
	the ambient material. As in Figure 2.1, the column densities include a factor of 2. At late	
	times, part of the cloud's tail has slowed too much to be considered part of the cloud.	
	This can be seen by comparing Figure 2.2 with Figure 2.1	16
2.3	The number density and temperature of the gas in the domain at $x=0$ kpc. The	
	left panel is for O VI and the right panel is for O III. The color bar represents the	
	number density and the contours show the gas temperature. The four contour levels	
	are 2×10^3 K, 2×10^4 K, 2×10^5 K and 2×10^6 K. Substantial fractions of O VI and	
	O III can be seen across a wide range of temperatures, from less than $2\times10^3~\mathrm{K}$ to more	
	than 2×10^5 K. There is significant overlap between O VI-rich gas and O III-rich gas	28

2.4	Top panel: the $f_{ m OVI}$ and temperature are plotted with a blue dot for every cell in the cloud.	
	Bottom panel: the $f_{ m OVI}$ and temperature are plotted with a blue dot for every sight line	
	through the cloud. The sight lines are oriented parallel to the \boldsymbol{x} axis and the temperature	
	is the mass-weighted average temperature along the line of sight. Both plots were made	
	from Run 1 at 100 Myr. Only the material that met the cloud's velocity criterion was used	
	to make these plots. For comparison, the $f_{ m OVI}$ vs T curve for static gas is plotted in red.	
	It was adopted from Gnat & Sternberg (2007a). O VIis confined to a narrower range of	
	temperatures in the static curve than in our simulations, which include dynamic mixing	
	of warm and hot gas.	29
2.5	Plot of the cloud-averaged $f_{ m OVI}$ for each simulation as a function of time. Generally,	
	$f_{ m OVI}$ increases with time as the cloud mixes with the ambient material	30
2.6	Plots of H I/O VIfor each simulation as a function of time. Generally, H I/O VIdecreases	
	with time as hydrogen is ionized and $f_{ m OVI}$ increases (see Figure 2.5). Also shown are the	
	average observed H I/O VI ratios for Complex C (Sembach et al., 2003a). The discussion	
	for Magellanic Stream can be seen in Goetz et al. (2024a)	30
3. I	Column density map of O VIat 100, 150 and 200 Myrs for Run 1. The color bar presents	
	the value of the O VIcolumn density, N(O VI). The contour lines and their labeled values	
	represent the hydrogen column density	36
3.2	Left Panel: O VInumber density in the cloud, along a slice through the domain in the	
	x=0 plane at 150 Myrs from Run 1. The color bar displays the O VInumber density. Mid-	
	dle Panel: Temperature in the cloud, along a slice through the domain in the x=0 plane	
	at 150 Myrs from Run 1. The color bar displays the temperature. Right Panel: Metallicity	
	in the cloud, along a slice through the domain in the x=0 plane at 150 Myrs from Run	
	1. The color bar displays the metallicity. The red, blue and orange lines are the simulated	
	sight lines. The orange line in the middle panel is the sight line in Figure 3.3, and the blue	
	line in the left panel is the sight line in Figure 3.4	37

3.3	Maxwell-Boltzmann distributions for all the cells along a sight line, calculated from their	
	temperatures and bulk velocities. Each curve is for a single cell. The location of this	
	sight line is marked in orange in the second panel of Figure 3.2. In this plot, we can see	
	two obvious clusters of cool gas with one centered around 20 ${\rm km}\ {\rm s}^{-1}$ and the other one	
	centered around 45 ${\rm km~s^{-1}}$ The curves have various colors in order to separate them	
	visually	38
3.4	Maxwell-Boltzmann distributions for all the cells along a sight line, calculated from their	
	temperatures and bulk velocities. Each curve is for a single cell. The location of this sight	
	line is marked in blue in the first panel of Figure 3.2. The curves have various colors in	
	order to separate them visually.	38
3.5	O VIdistributions for individual cells along a sight line. Each curve is for a single cell.	
	The location of this sight line is marked in orange in the middle panel of Figure 3.2. The	
	curves have various colors in order to separate them visually.	39
3.6	O VI spectrum for the sight line that is identified in Figure 3.2. It is calculated by summing	
	the individual curves in Figure 3.5	40
3.7	O VIspectrum from the sight line that is identified in Figure 3.2. It is calculated by using	
	the same method as for Figure 3.6 but with its own O VI distributions for individual cell.	4 I
3.8	Plot of optical depth, τ vs. velocity from Trident results. Trident models the LSF effect	
	and this is why the shape of the curve here is slightly different from the one in Figure 3.6.	42
3.9	Plot of optical depth, τ vs. velocity from Trident results. Trident models the LSF effect	
	and this is why the shape of the curve here is slightly different from the one in Figure 3.7.	43
3.10	Final O VI absorption spectrum for the sight line in orange labeled in Figure 3.2. The	
	total line profile and each component are fitted by a Voigt profile in the SciPy library in	
	Python	44
3.11	Final O VI absorption spectrum for the sight line in blue labeled in Figure 3.2. The total	
	line profile and each component are fitted by a Voigt profile in the SciPy library in Python.	45

4.I	C IVcolumn density plots for Run 1 at 5 epochs (0, 50, 100, 150, and 200 Myr). The	
	column densities are calculated by integrating the C IVnumber density along sight lines	
	directed into the page. These sight lines are in the \hat{y} direction, which is the direction in	
	which only half the cloud was simulated. So, we have multiplied the column densities	
	by 2 to account for having simulated only 1/2 of the cloud. The ambient gas moves to	
	the right, interacting with the cloud gas. The resulting tail formation and hydrodynamic	
	instabilities are apparent in this figure	58
4.2	Si IVcolumn density plots for Run 1 at 5 epochs (0, 50, 100, 150, and 200 Myr). The	
	column densities are calculated by integrating the Si IV number density along sight lines	
	directed into the page. These sight lines are in the \hat{x} direction. The ambient gas moves to	
	the right, interacting with the cloud gas. The resulting tail formation and hydrodynamic	
	instabilities are apparent in this figure	59
4.3	C IVcolumn density plots for Run 1 at 5 epochs (0, 50, 100, 150, and 200 Myr) for	
	material whose velocity in the \hat{z} direction differs by more than 100 km s $^{-1}$ from that of	
	the ambient material. As in Figure 4.1, the column densities include a factor of 2. At late	
	times, part of the cloud's tail has slowed too much to be considered part of the cloud.	
	This can be seen by comparing Figure 4.3 with Figure 4.1	60
4.4	Left: Metallicity plot of the cloud in the domain at $x=0\mathrm{kpc}$. Right: Temperature plot	
	of the cloud in the domain at $r=0$ kpc	61

4.5	Top panel: the $f_{\rm CIV}$ and temperature are plotted with a blue dot for every cell in the cloud.	
	Bottom panel: the $f_{ m CIV}$ and temperature are plotted with a blue dot for every sight line	
	through the cloud. The sight lines are oriented parallel to the \boldsymbol{x} axis and the temperature	
	is the mass-weighted average temperature along the line of sight. Both plots were made	
	from Run 1 at 100 Myr. Only the material that met the cloud's velocity criterion was used	
	to make these plots. For comparison, the $f_{\rm CIV}$ vs T curve for static gas is plotted in red.	
	It was adopted from Gnat & Sternberg (2007a). C IVis confined to a narrower range of	
	temperatures in the static curve than in our simulations, which include dynamic mixing	
	of warm and hot gas.	62
4.6	Top panel: the $f_{ m SiIV}$ and temperature are plotted with a blue dot for every cell in the cloud.	
	Bottom panel: the $f_{ m SiIV}$ and temperature are plotted with a blue dot for every sight line	
	through the cloud. The sight lines are oriented parallel to the \boldsymbol{x} axis and the temperature	
	is the mass-weighted average temperature along the line of sight. Both plots were made	
	from Run 1 at 100 Myr. Only the material that met the cloud's velocity criterion was used	
	to make these plots. For comparison, the $f_{ m SiIV}$ vs T curve for static gas is plotted in red.	
	It was adopted from Gnat & Sternberg (2007a). Si IVis confined to a narrower range of	
	temperatures in the static curve than in our simulations, which include dynamic mixing	
	of warm and hot gas.	63
4.7	Plot of the cloud-averaged $f_{ m CIV}$ for each simulation as a function of time. Generally,	
	$f_{ m CIV}$ increases with time as the cloud mixes with the ambient material. $\dots \dots$	64
4.8	Plot of the cloud-averaged $f_{ m SiIV}$ for each simulation as a function of time. Generally,	
	$f_{ m SiIV}$ increases with time as the cloud mixes with the ambient material	64
4.9	Plots of H I/C IV for each simulation as a function of time. Generally, H I/C IV decreases	
	with time as hydrogen is ionized and $f_{ m CIV}$ increases (see Figure 4.7)	65
4.10	Plots of H I/Si IV for each simulation as a function of time. Generally, H I/Si IV decreases	
	with time as hydrogen is ionized and $f_{ m SiIV}$ increases (see Figure 4.8)	65

4. II	Plot of $f_{\rm CIV}$ for Run 1 for a variety of cloud and ambient metallicities. Changing the	
	ambient metallicity has little effect on the curve. Changing the cloud metallicity has a	
	more noticeable but still insignificant effect	67
4. I2	Plot of $f_{ m SiIV}$ for Run 1 for a variety of cloud and ambient metallicities. Changing the	
	ambient metallicity has little effect on the curve. Changing the cloud metallicity has a	
	more noticeable but still insignificant effect	67
4.13	Plots of H I/C IVfor Run 1 for a variety of cloud and ambient metallicities. As for	
	$f_{ m CIV}$, changing the ambient metallicity has little effect on the curve. Changing the cloud	
	metallicity has a more noticeable, but still small effect.	68
4.I4	Plots of H I/Si IVfor Run 1 for a variety of cloud and ambient metallicities. As for	
	$f_{ m SiIV}$, changing the ambient metallicity has little effect on the curve. Changing the cloud	
	metallicity has a more noticeable, but still small effect.	68
5. I	Optical image of NGC 1068 from GALEX. The purple cross marks the center location	
	of the FUSE LWRS aperture.	79

LIST OF TABLES

2. I	Simulation Parameters	12
2.2	$f_{ m OVI}$	18
2.3	Complex C Log Column Densities	22
3. I	Simulation Parameters	35
3.2	Run 1 at 100 Myrs	46
3.3	Run 1 at 150 Myrs	47
3.4	Run 1 at 200 Myrs	48
4. I	Simulation Parameters	56
4.2	$f_{ m CIV}$	57
4.3	$f_{ m SiIV}$	66
5.1	O VIemission	81
5.2	FUSE LWRS Apertures toward Galaxies	82
А.1	Run 2 at 100 Myrs	85
A.2	Run 2 at 150 Myrs	86
A.3	Run 2 at 200 Myrs	86
A.4	Run 3 at 100 Myrs	87
A.5	Run 3 at 150 Myrs	87
A.6	Run 3 at 200 Myrs	88
A.7	Run 4 at 100 Myrs	88

A.8	Run 4 at 150 Myrs	89
A.9	Run 4 at 200 Myrs	89
А.10	Run 5 at 100 Myrs	90
А.п	Run 5 at 150 Myrs	90
A.12	Run 5 at 200 Myrs	90
A.13	Run 6 at 100 Myrs	91
A.14	Run 6 at 150 Myrs	91
A.15	Run 6 at 200 Myrs	92
A.16	Run 7 at 100 Myrs	92
A.17	Run 7 at 150 Myrs	93
A.18	Run 7 at 200 Myrs	94
A.19	Run 8 at 100 Myrs	94
A.20	Run 8 at 150 Myrs	95
A.21	Run 8 at 200 Myrs	95
A.22	Run 9 at 100 Myrs	96
A.23	Run 9 at 150 Myrs	97
A.24	Run 9 at 200 Myrs	98
A.25	Run 10 at 100 Myrs	99
A.26	Run 10 at 150 Myrs	99
۸ ۵.	Cup to at 200 Myrs	~~

CHAPTERI

Introduction

Galaxies like our own Milky Way are not isolated islands in the cosmos. Instead, they are deeply embedded within vast, diffuse halo gas whose outer regions are known as the circumgalactic medium (CGM). The CGM acts as a crucial reservoir of baryons, extending for hundreds of kiloparsecs and containing a mass of gas comparable to, or even exceeding, the stellar mass of the galaxy itself (Tumlinson et al., 2017). This massive reservoir is the dynamic interface between a galaxy and the wider intergalactic medium (IGM) (Putman et al., 2012), serving as both a repository for powerful galactic outflows driven by star formation and active galactic nuclei, and as the source of fuel for future star formation through accretion (Heckman et al., 2017; Harrison, 2017). Therefore, understanding the physical processes that govern the CGM is fundamental to developing a complete picture of galaxy evolution.

A significant feature of the CGM is the presence of High-Velocity Clouds (HVCs), which are distinct clouds of gas observed in the halo whose velocities differ significantly from those predicted by a simple model of Galactic rotation (Wakker & van Woerden, 1997). HVCs represent the coldest and densest component of the halo gas and are understood to be a combination of material accreting from the IGM and recycled feedback material from the galactic disk (Putman et al., 2012). Both the extended CGM and the individual HVCs within it are characterized by their complex, multiphase structure. Observations reveal gas across a vast range of temperatures and densities, broadly classified into a cool phase ($T \sim 10^4$ K), traced by neutral hydrogen (H I) and low-ionization metals; a hot phase ($T > 10^6$ K), detected through

its X-ray emission; and a warm-hot phase ($T\sim 10^5-10^6$ K) that appears to contain a substantial fraction of the CGM's mass (Tumlinson et al., 2017; Hafen et al., 2019).

Tracing the warm-hot gas is a key challenge in astrophysics. One of the most powerful tools for this purpose is the highly ionized oxygen ion, O VI. With its doublet absorption lines at wavelengths of $\lambda\lambda 1032$, 1038 Å, O VI is readily detectable in the ultraviolet (UV) spectra of distant background sources like quasars. The \sim 114 eV required to ionize O⁴⁺ to O⁵⁺ means it is an excellent tracer of the mixing between different gas phases. In a gas in thermal equilibrium, O VI abundance peaks at a temperature of approximately 3×10^5 K, making it an ideal probe of the warm-hot phase of the CGM and the interfaces of HVCs (Savage et al., 2003; Heckman et al., 2002a).

The interpretation of the observed amount of O VI, however, depends critically on the assumed ionization population state of oxygen ions. The simplest model assumes the conditions of Collisional Ionization Equilibrium (CIE), where the population of ions has stabilized such that rate of ionization by collisions is balanced by the rate of recombination. While CIE is a useful baseline, the CGM is a dynamic environment where gas can be heated or cooled on timescales shorter than the ionization and recombination timescales. Such conditions, where ionization and recombination are out of balance, are known as Non-Equilibrium Ionization (NEI). (Gnat & Sternberg, 2007b). For example, in rapidly cooling gas, ions can remain "over-ionized" relative to their CIE state at a given temperature. This has a profound impact on the O VI ionization fraction, $f_{\rm OVI} = N({\rm O\,VI})/N({\rm O})$, which can be significantly different in NEI conditions from the fraction in CIE at the same temperature. Understanding the ionization state is essential for correctly inferring the total amount of hydrogen and therefore the mass of the systems associated with the observed O VI absorption. In this thesis, we develop a methodology to estimate the value of $f_{\rm OVI}$ from our simulations and then use it to estimate the amount of hydrogen along the observed sight lines. In addition to using O VI as a tracer, we apply the same methodology to C IV and Si IV, which are also very well-observed ions.

An important physical mechanism for producing both the multiphase structure of the CGM and the significant amounts of observed O VI is the dynamic mixing that occurs at the interface of different gas phases. Specifically, the interaction between cool, dense clouds (like HVCs) and the hot, diffuse ambient

halo generates turbulent mixing layers. Within these layers, the hot and cool gas mix, producing significant quantities of gas at intermediate temperatures ($10^5-10^6\,\mathrm{K}$). This process is inherently dynamic and likely proceeds under NEI conditions, making these mixing layers prime locations for O VI production (Ji et al., 2019; Begelman & Fabian, 1990; Fielding et al., 2020). This thesis will employ hydrodynamic simulations using the FLASH code (Fryxell et al., 2000a) with adaptive mesh refinement and NEI to model the creation and evolution of these turbulent interfaces and study the resulting ionization structure of the HVCs.

The primary observational data for studying this warm-hot gas comes from absorption line spectroscopy. The profiles of absorption lines, such as those from O VI, reveal key details about the physical conditions of the gas they trace. The width of a spectral line is governed by the Doppler broadening parameter, b, which reflects the velocity distribution of the absorbing ions along a sight line. This parameter has contributions from both thermal effects and non-thermal effects:

$$b^2 = b_{ ext{thermal}}^2 + b_{ ext{non-thermal}}^2 = \frac{2k_BT}{m_{ ext{ion}}} + b_{ ext{non-thermal}}^2$$

Here, k_B is the Boltzmann constant, T is the kinetic temperature of the gas, and $m_{\rm ion}$ is the mass of the absorbing ion (in this case, oxygen). The $b_{\rm non-thermal}$ term accounts for velocity gradients within the absorbing gas along the sight line. This broadening is due to the dispersion of bulk velocity flows, which can be produced by processes such as turbulent mixing between different gas phases.

While many O VI absorption line features are broad, observational surveys have also found some O VI systems exhibiting narrow line widths that are well-aligned in velocity with co-spatial H I absorption (Tripp et al., 2008a). These narrow profiles often imply cool gas temperatures ($T \ll 10^5$ K), substantially lower than the $\sim 3 \times 10^5$ K temperature where the $f_{\rm OVI}$ value peaks in the static model (Gnat & Sternberg, 2007b). This temperature discrepancy is strong evidence that the O VI-bearing gas is out of CIE. The origin of this non-equilibrium O VI is a key area of debate. One possibility is photoionization of cool ($\sim 10^4$ K) gas, but models only including the extragalactic UV background are generally insufficient to explain the observed column densities (Werk et al., 2016). Another significant challenge for this theory

is its requirement for an extremely low-density gas. In order to produce the observed absorption-line strengths, such a diffuse cloud requires an exceptionally large path length, which is considered physically unlikely. (Savage et al., 2014)

An alternative physical mechanism is the turbulent mixing between gas in different phases. This dynamic process with NEI can cause O VI to exist in cool regions of the gas at temperatures far below $\sim 3 \times 10^5$ K. Modern, high-resolution simulations of these turbulent interfaces confirm they are highly effective at producing significant quantities of O VI as the gas mixes (Kwak & Shelton, 2010a; Kwak et al., 2011; Ji et al., 2019; Fielding et al., 2020). Building on this framework, this thesis will demonstrate through simulations of HVCs how dynamic mixing, coupled with NEI modules, can naturally reproduce the narrow O VI line widths observed in the CGM.

We aim to connect theory and observation by investigating the relationship between hydrodynamic processes in the CGM and their observational signatures. By using the FLASH code to perform hydrodynamic simulations of the interaction between HVCs and the ambient gas, we study the generation of turbulence and the production of O VI and other ions in the resulting mixing layers. We then generate synthetic absorption line spectra from these simulations and analyze the *b* values of the O VI lines. The goal is to understand how the thermal and non-thermal components of the line width are related to the complex, multiphase, and turbulent gas structures produced in the simulations. This work will provide a more detailed physical interpretation of the observed O VI absorption systems and shed light on the crucial role of turbulent mixing in shaping the CGM.

Lastly, we extend the scope of this dissertation to the O VI emission intensity from the extended disk of the starburst galaxy, NGC 1068. This study gives us a sense on the unusual nature of the physical feedback from the NGC 1068's starburst activity and AGN.

CHAPTER 2

Unveiling the Hidden Mass Associated with Observed O VI in Intergalactic and Circumgalactic High Velocity Clouds ¹

¹Goetz, E., Wang, C., & Shelton, R. L. 2024, ApJ, 960, 66,389 doi: 10.3847/1538-4357/adodf7390. Reproduced with permission from the Astrophysical Journal. This chapter has been modified to reflect my individual contributions.

Abstract

We present a new method to calculate the total amount of material in clouds quickly moving through circumgalactic and intergalactic medium from O VI measurements. We use FLASH hydrodynamic code to simulate high-velocity clouds (HVCs) and calculate the time-dependent oxygen ionization populations. After calculating the O VI/oxygen ratio (f_{OVI}) within the dynamic NEI clouds, we find that it is significantly different from that in static gas. We find that the existence of O VI spans a wide temperature range from cool, medium to hot gas in the clouds. As a result, O VI can trace all the hydrogen including both neutral and ionized hydrogen, but not only the ionized hydrogen. The observed O VI column density, metallicity, and our estimated $f_{
m OVI}$ can be used to calculate the amount of hydrogen along an observed sight line through a cloud. Here we present our $f_{\rm OVI}$ calculated from the simulations. We also provide a prescription to identify $f_{\rm OVI}$ for observed dynamic clouds. In addition, we develop a methodology to calculate the total hydrogen column density from our f_{OVI} and the OVI column density from observations. To illustrate how it works, we calculate the total hydrogen column densities along different observed sight lines through Complex C and the Magellanic Stream, two very famous HVCs, by using our f_{OVI} . Our results reveal that there are more material than the previous lower limits predict in these two HVCs. We also analyze the low-redshift intergalactic O VI clouds with this method, showing that these systems have several times more baryonic material than previously thought and thus can explain a large fraction of the baryonic material in the Universe.

2.1 Introduction

Gaseous clouds are ubiquitous across the Universe. They are found in nearly every type of structure, from protostellar objects to galaxy clusters. They are of obvious importance to their hosts. Clouds in and near our Galaxy, for example, affect the star formation rate and galactic evolution while clouds throughout intergalactic space contribute to the tally of baryonic mass in the Universe (Richter et al., 2004). Examples of the former are high-velocity clouds (HVCs), clouds with $|v_{LSR}| \ge 90 \text{ km s}^{-1}$ (Wakker & van Woerden, 1997) or 100 km s⁻¹ (Richter, 2017). They affect our Galaxy's evolution by providing gas that can be used in the future to form additional stars (Putman et al., 2012; Fox et al., 2019).

In general, HVCs are multi-structured and multiphase. They can contain neutral gas such as H I and O I, but can also contain low ions such as H II, C II and O II, and even high ions such as C IV, O VI and Si IV.

Many HVCs appear to be out of collisional ionization equilibrium (CIE). This is because their absorption features have such narrow line widths that their temperatures must be well below their CIE temperatures (e.g., Yao et al. (2011a); Tripp (2022)). Photoionization has been suggested as a possible way to highly ionize the gas without substantially heating it. However, the photon field at 114 eV is generally considered too weak to ionize substantial amounts of O V to O VI (Tripp et al. (2003), Sembach et al. (2003a), hereafter Sembach et al. (2003a), Fox et al. (2004), Ganguly et al. (2005), Fox et al. (2010a), hereafter Fox et al. (2010a). Cooling flow models have also been considered (Heckman et al., 2002b; Tripp, 2022), because they naturally explain high ions at temperatures below their CIE temperatures. The mixing between hot ambient gas and cooler HVC gas will also yield large numbers of cool high ions (Kwak & Shelton, 2010a).

Additional indications that the gas is out of CIE come from line ratios, such as Si IV/C IV and C IV/O VI. Simultaneous fitting of these line ratios shows that the predictions of non-equilibrium ionization (NEI) models are closer to observational data than those from CIE models (Tripp, 2022).

Of the high ions present in HVCs, O VI is often chosen as a tracer of highly ionized HVC gas (Sembach et al. (2003a); Fox et al. (2006); Fox et al. (2010a); Cashman et al. (2023)). because oxygen is the most

abundant metal in HVCs and because its large oscillator strength allows for easier observations (Morton, 1991). The Hubble Space Telescope and the Far Ultraviolet Spectroscopic Explorer have detected O VI in HVCs along sight lines toward many AGNs.

Once an O VI column density has been observed, it can be used to estimate the associated hydrogen column density if the oxygen metallicity and O VI ionization fraction (O VI/oxygen, $f_{\rm OVI}$) of the cloud are also given. In the past, the hydrogen associated with O VI had been assumed to be hot and ionized (e.g. Sembach et al. (2003a); Sembach et al. (2004); Fox et al. (2010a)) because according to CIE and NEI calculations of static gas (Sutherland & Dopita, 1993a; Gnat & Sternberg, 2007a), O VI only exists at temperatures on the order of 10^5 K. Once calculated, the resulting H II column density was then added to the H I column density measured from observations of the 21 cm lines or the hydrogen Lyman series lines, if available, to estimate the total hydrogen column density. Some authors also added components related to Si IV and/or other ions (e.g. Fox et al. (2010a)). Until now, calculations of the H II column density have adopted as an upper limit the maximum value of $f_{\rm OVI}$ from static gas models such as Sutherland & Dopita (1993a); Gnat & Sternberg (2007a). The peak $f_{\rm OVI}$ in those models is ~ 0.2 and occurs at a temperature of $\sim 3 \times 10^5$ K.

We set about to calculate the average $f_{\rm OVI}$ for dynamic NEI gas, with the awareness that since some O VI exists at temperatures above and below 3×10^5 K, the average $f_{\rm OVI}$ will be below the peak value. This new value of $f_{\rm OVI}$ results from FLASH simulations of the ionization and recombination of oxygen in HVCs. The FLASH code (Fryxell et al., 2000b) has been used previously to study HVCs (Kwak et al., 2011; Plöckinger & Hensler, 2012; Gritton et al., 2014a, 2017; Galyardt & Shelton, 2016; Sander & Hensler, 2021). Considering the variety of individual HVCs and the uncertainty in the density, temperature, size, and velocity of specific HVCs, we simulate ten HVCs spanning a range of initial cloud parameters. We track their evolutions over time as they interact with the ambient medium. The dynamic nature of these simulations allows for mixing between the cold cloud and the hot ambient material. This mixing allows ambient material to become entrained within the cloud. These interactions, combined with the non-equilibrium nature of ionization and recombination, have significant effects on the ionization fraction of O VI.

We find that O VI physically overlaps with both neutral and ionized hydrogen in the cloud. Therefore, the entire cloud must be considered when finding the average $f_{\rm OVI}$. We calculate $f_{\rm OVI}$ from the ratio of the number of O VI ions in the cloud to the number of oxygen atoms in the cloud. The hydrogen column density calculated from this $f_{\rm OVI}$ and O VI measurements must therefore be reinterpreted. It is the hydrogen in all phases rather than merely the $\sim 3 \times 10^5$ K component of the hydrogen.

This paper develops a methodology for calculating the total amount of hydrogen from an observed O VI column density. This new methodology requires an estimate of the average $f_{\rm OVI}$ across the cloud, which we have extracted from the simulations presented in this paper. We present a prescription for determining the $f_{\rm OVI}$ pertaining to a given line of sight from the observed column densities of O VI and H I on the sight line.

We describe our setup and state our simulation parameters for our 10 FLASH simulations in Section 2.2. In Section 2.3, we present the results of the simulations and the post-processing steps we take. We also present our updated methodology for calculating the total hydrogen column density and apply it to two example clouds: Complex C and the Magellanic Stream (MS). Our method yields more material than do previous methods based on the peak value of the static CIE or NEI $f_{\rm OVI}$. In Section 2.4 we present our prescription for determining $f_{\rm OVI}$ from observed H I/O VI ratios on other sight lines and show that there is much more material in HVCs and low-redshift intergalactic O VI clouds than previously thought.

2.2 Methods

The simulations are done by using FLASH version 4.6.2 (Fryxell et al., 2000b). We utilize FLASH's hydrodynamic and NEI modules to compute the time-dependent ionization states of oxygen. Radiative cooling is determined by a lookup table based on the CIE cooling curve for [Fe/H] = -0.5 as provided by Sutherland & Dopita (1993a).

The simulations are performed in 3D Cartesian coordinates with adaptive mesh refinement. Each simulation domain is a rectangular cuboid with dimensions of 2.4 kpc \times 1.2 kpc \times 10.8 kpc along the \hat{x} ,

 \hat{y} , and \hat{z} axes, respectively. The domain is equally divided into 18 square blocks arranged in a 2 × 1 × 9 configuration. Every cell has a maximum spatial resolution of 9.375 pc per cell in each direction.

The simulations are set up in a wind tunnel configuration, where ambient material enters through the lower z-boundary and exits through the upper z-boundary. Additionally, material can flow out of the domain though the lower and upper x-boundaries as well as the y-boundaries. To use the cloud's assumed symmetry, the cloud's center is aligned with the lower y-boundary, and only half of the cloud is simulated within the domain. The lower y-boundary is set as a reflecting boundary.

At the start of the simulation, the cloud's center is positioned 1.2 kpc above the lower z-boundary, corresponding to the coordinates (x=0 kpc,y=0 kpc z=0 kpc) in the simulation domain. From the domain's perspective, the cloud remains stationary at the start of the simulation. However, relative to the ambient gas, the cloud appears to move with the same velocity as the wind speed in the $-\hat{z}$ direction.

In this study, O VI is utilized as a tracer for hydrogen in regions of highly ionized gas. Therefore, it is crucial to incorporate an appropriate estimate for the oxygen metallicity in our calculations. Our choice of metallicity is guided by values observed in comparison clouds such as the MS and Complex C. The oxygen metallicity is various within both the MS and Complex C (Fox et al. (2013b); Sembach et al. (2003a)), and different researchers have reported slightly different values. Fox et al. (2010a) adopted a metallicity of 0.1 solar for the MS, which was also used by Sembach et al. (2003a) for Complex C. In their work, Fox et al. (2010a) relied on the Asplund et al. (2009a) abundance table, which suggests that there are 4.89×10^{-4} oxygen atoms per hydrogen atom. On the other hand, Sembach et al. (2003a) used the Holweger (2001) abundance table, which estimates 5.45×10^{-4} oxygen atoms per hydrogen atom. However, Holweger (2001) did not calculated the sightlines' hydrogen column densities, but the total hydrogen mass of the cloud. We adopt the same metallicity and abundance table Fox et al. (2010a) used for the consistency. The related O/H value aligns closely with values reported by Fox et al. (2013a) and Howk et al. (2017) for the MS, and Collins et al. (2007) from Complex C. Although a 0.1 solar metallicity is also searched by Wakker et al. (1999) and Richter et al. (2001), they referenced the abundance table from Anders & Grevesse (1989), which estimates approximately 1.6 times more oxygen atoms per hydrogen atom. Several other observations have suggested that the metallicity of Complex C might be higher (up to 0.3 solar (Tripp

et al. (2003), Shull et al. (2011))), based on the Holweger (2001) and Asplund et al. (2009a) abundance tables, respectively. According to this, we also explore the impact of adopting different metallicity values for the cloud.

The metallicity of the ambient medium remains uncertain, with a broad range of values reported in different studies. Miller & Bregman (2015), using O VIII emission lines and adopting the abundances from Anders & Grevesse (1989), estimated the circumgalactic medium (CGM) metallicity to be at least 0.3 times the solar value. Similarly, Troitsky (2017) modeled the density of the CGM and identified a best-fit metallicity of approximately 0.5 solar at a height of 10 kpc, although the uncertainties were considerable. Their analysis builds upon the results of Miller & Bregman (2015), and assumes the Anders & Grevesse (1989) abundance. In contrast, Miller et al. (2016) analyzed O VII absorption features in combination with pulsar dispersion measures, finding a metallicity estimate for the halo gas of at least 0.6 solar, based on the abundances from Holweger (2001). The studies which compare between observational data and simulations also offer us insights. Henley et al. (2017), using simulations performed with FLASH which typically employs the Anders & Grevesse (1989) abundances, found results consistent with a halo metallicity of roughly 0.7 solar. Additionally, Henley & Shelton (2015) modeled the X-ray emission from the halo using solar metallicity across several oxygen abundance tables, obtaining good reduced χ^2 values in all cases. This outcome highlights the difficulty in tightly constraining the oxygen abundance through such emission modeling.

Given this diversity of derived metallicities, we adopt a fiducial ambient metallicity of 0.7 solar in our analysis. Nonetheless, we also examine the implications of varying the ambient metallicity across a plausible range.

To incorporate these metallicities into our analysis, we follow a two-step procedure. In the first step, we assign simple, convenient initial metallicity values to the cloud and ambient gas within the FLASH simulations. Specifically, we set the cloud to an initial metallicity of 10^{-3} times solar, and the ambient medium to 1 times solar. In the second step, during post-processing, we re-scale these initial values to match the desired metallicities, 0.1 solar for the cloud and 0.7 solar for the ambient medium. As noted previously, we also apply additional re-scalings to explore how variations in the cloud and ambient metallicities affect

0. 1 .	TT.			Parameters		
Simulation	$T_{ m cloud}$	$n(H)_{cloud}$	$T_{ m ambient}$	$n(H)_{ambient}$	$v_{ m inflow}$	$r_{ m cloud}$
	(K)	(cm^{-3})	(K)	$(cm^{-3})(K)$	$(\mathrm{km} \mathrm{s}^{-1})$	(pc)
Run 1	5000	0.4	2×10^{6}	0.001	150	500
Run 2	5000	0.4	2×10^{6}	0.001	100	500
Run 3	5000	0.4	2×10^6	0.001	150	300
Run 4	5000	0.4	2×10^6	0.001	300	500
Run 5	5000	0.04	2×10^{6}	0.0001	150	300
Run 6	5000	0.2	1×10^{6}	0.001	150	500
Run 7	1000	2.0	2×10^{6}	0.001	150	500
Run 8	1000	I.O	1×10^{6}	0.001	150	500
Run 9	3000	0.67	2×10^{6}	0.001	300	500
Run 10	9000	0.222	2×10^{6}	0.001	150	500

our results. Although FLASH adopts the abundance table of Anders & Grevesse (1989) by default, during post-processing we adjust the results to be consistent with the abundances of Asplund et al. (2009a).

To study the mixing, cooling, ionization, and recombination processes between the cloud and ambient medium, we model ten simulations with varying initial conditions (see Table 2.1). Cloud hydrogen densities, n(H) cloud, span 0.04–2 cm⁻³, and cloud temperatures, T cloud, range from 1000 K to 9000 K. The ambient medium is set to either $T_{ambient} = 10^6$ K or 2×10^6 K, and $n(H)_{ambient} = 10^{-3}$ cm⁻³ or 10^{-4} cm⁻³. Each simulation begins with the cloud in pressure equilibrium with the ambient gas, which determines the cloud density once its temperature and the ambient parameters are fixed. Previous studies (Grønnow et al., 2017; Gritton et al., 2017), along with our preliminary tests, indicate that the initial cloud radius significantly influences its evolution, particularly in terms of mixing and ionization. Therefore, we adopt two cloud radius, 300 pc and 500 pc, and explore three wind velocities: 100, 150, and 300 km s⁻¹, to study how ambient inflow speed impacts mixing. All simulations are designed to run for 200 Myr, allowing sufficient time for each cloud to interact with the surrounding medium and evolve. Due to computational constraints, Runs 4 and 5 ended earlier, at 185 Myr and 128 Myr, respectively, though both progressed far enough for the clouds to reach a fully evolved state.

Table 2.1 lists the cloud parameters which refer to values at the cloud center. Toward the cloud's edging regions, both density and temperature gradually transition into those of the ambient medium. The density

profile follows the hyperbolic tangent function described by Gritton et al. (2014a), with a scale length of 50 pc. To maintain pressure equilibrium across this interface, the temperature increases inversely with the density, ensuring a smooth match to ambient conditions. The transition in chemical abundance from cloud to ambient values is defined at the point where the hydrogen density equals 0.99, $n_{\rm ambient} + 0.01$, $n_{\rm cloud}$, with the velocity profile transitioning at the same location.

At the beginning of each simulation, the ambient materials have the same initial speeds as the wind speeds listed in Table 2.1. At later epochs, material is stripped from the cloud and meanwhile ambient gas becomes entrained within the cloud. This interaction between the cloud and environmental gas leads to some computational cells containing comparable fractions of cloud and ambient material, progressively erasing the clear boundary between them. As a result, a new criterion for identifying cloud material is required, one that aligns with observational practices and remains computationally practical. In observational studies, velocity contrast is commonly used to distinguish cloud materials from the ambient materials. HVCs are typically defined as objects whose velocities are different from the local standard of rest by at least 90 or 100 kms⁻¹ (Wakker & van Woerden, 1997; Richter, 2017). Following this approach, we define cloud material in our simulations as any gas whose velocity in the \hat{z} direction differs by more than 100 kms⁻¹ from that of the ambient medium. Since the ambient flow gradually accelerates during the simulation, we consider this evolution when applying the velocity criterion.

Our simulations explicitly track the mass contributions of hydrogen and helium, with heavier elements making negligible contributions to the total mass budget. Within each simulation, the ionization state populations of helium and oxygen are evolved in a time-dependent manner, governed by collisional ionization and recombination rates. However, the ionization states of hydrogen are not directly calculated. To address this issue in the post-processing, we use the assumption that the fraction of neutral hydrogen relative to the total hydrogen ions is equal to the fraction of neutral oxygen relative to the total oxygen ions. This assumption is supported by the nearly identical first ionization potentials of hydrogen and oxygen (Cox, 2000) and by the prevalence of charge exchange processes between the two species (Field & Steigman, 1971).

High-velocity clouds are exposed to photon fields from both extragalactic and Galactic sources, which affects their ionization state. To quantify this photoionization effect, we conduct Cloudy simulations (Ferland et al., 2017) during post-processing. The incident radiation field combines the extragalactic background (EGB), modeled using the HMo5 spectrum (Ferland et al., 2017), with ionizing photons escaping the Milky Way, for which we adopt the Fox et al. (2005a) model. We use the same value for total ionizing fluxes as the one from Fox et al. (2010a), which used the same elemental abundance table (Asplund et al., 2009a) as we used in our calculations.

We validate our setup by reproducing portions of Figure 5 in Fox et al. (2010a), confirming that our radiation field implementation is consistent with previous work. Each simulation treats the cloud as a uniform-density slab, initialized with the same density and temperature as in the corresponding FLASH model. From these Cloudy runs, we figure out the column of hydrogen ionized by the combined radiation fields. Then we incorporate these values into our post-processing analysis (Section 2.3).

2.3 Results

2.3.1 Simulation Results

First, we will describe the clouds' dynamics. As the simulations progress, material is ablated from the cloud. This deforms the cloud from its initial spherical shape into a more elongated structure. The ablated material forms a tail, as can be seen in Figure 2.1 for a representative simulation (Run 1 in Table 2.1). All figures and analyses were done with the YT software package (Turk et al., 2011). The interaction between the ambient gas and the tail decelerates the tail. Over time, the tail will approach the speed of the ambient gas and so will no longer meet the cloud criterion. This is shown by comparing Figure 2.1 with Figure 2.2 for which the velocity criterion has been applied to the domain.

Hydrodynamic instabilities such as the Rayleigh-Taylor and Kelvin-Helmholtz instabilities also affect the cloud. Rayleigh-Taylor instabilities are due to the head-on collisions between cloud and ambient material (Drazin, 2002). Kelvin-Helmholtz instabilities are due to the velocity shear at the boundary of the cloud and ambient material (Drazin, 2002). These instabilities tear material from the cloud and

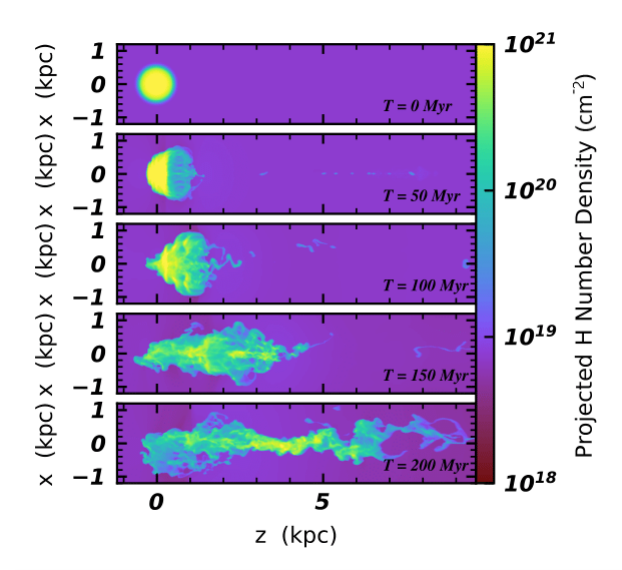


Figure 2.1: Hydrogen column density plots for Run 1 at 5 epochs (0, 50, 100, 150, and 200 Myr). The column densities are calculated by integrating the hydrogen number density along sight lines directed into the page. These sight lines are in the \hat{y} direction, which is the direction in which only half the cloud was simulated. So, we have multiplied the column densities by 2 to account for having simulated only 1/2 of the cloud. The ambient gas moves to the right, interacting with the cloud gas. The resulting tail formation and hydrodynamic instabilities are apparent in this figure.

incorporate hot, ambient material into the cloud. Because the ambient material is very hot, it contains high ions of oxygen such as O VII to O IX. Once entrained in the cloud, the hot gas transfers heat to the cold gas and both components radiatively cool. Consequently, the high ions from the entrained ambient gas begin to recombine and the neutral and low ions in the cloud begin to ionize (Kwak & Shelton, 2010a; Kwak et al., 2011).

As a result of this mixing, ionization, and recombination, O VI exists throughout the cloud and at a wide range of temperatures. The left panel of Figure 2.3 shows the O VI spatial distribution and the temperature distribution for Run 1 at 100 Myr. Due to their dynamic nature, our set of simulations contains O VI across a wide temperature range of $\sim 2,000$ K to $\sim 2,000,000$ K. In contrast, static CIE and NEI models, such as those of Sutherland & Dopita (1993a) and Gnat & Sternberg (2007a), predict that O VI exists in a comparatively narrow temperature range of $\sim 150,000$ K to $\sim 1,000,000$ K.

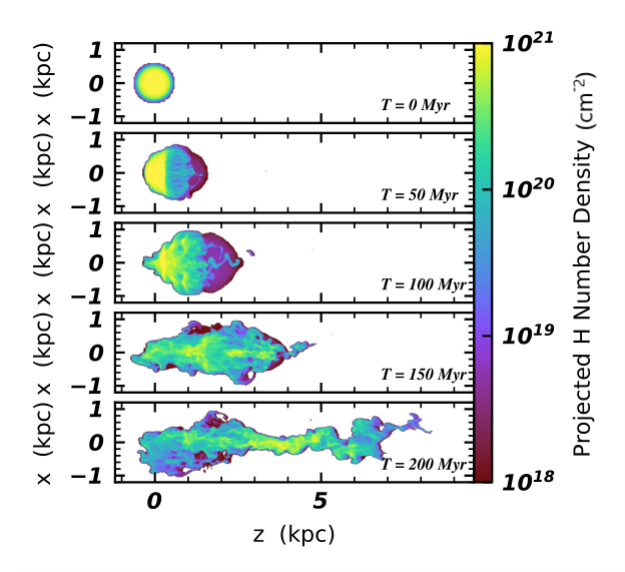


Figure 2.2: Hydrogen column density plots for Run 1 at 5 epochs (0, 50, 100, 150, and 200 Myr) for material whose velocity in the \hat{z} direction differs by more than 100 km s⁻¹ from that of the ambient material. As in Figure 2.1, the column densities include a factor of 2. At late times, part of the cloud's tail has slowed too much to be considered part of the cloud. This can be seen by comparing Figure 2.2 with Figure 2.1.

The fact that we find O VI at a wide range of temperatures is important because it means that O VI does not solely trace hot, ionized hydrogen, but instead exists in all phases of gas. It also has implications for the calculation of the hydrogen column density, which will be discussed later in this section. Furthermore, the oxygen atoms in the O VI state, $f_{\rm OVI}$, is significant across the entire temperature range found in the cloud. This is true both when examining cells and when examining sight lines through the clouds (see Figure 2.4). The evolution of the $f_{\rm OVI}$ is shown in Figure 2.5. At the beginning of each simulation, $f_{\rm OVI}$ is small. Over time, the cloud mixes with the ambient gas, causing $f_{\rm OVI}$ to rise. At even later epochs, $f_{\rm OVI}$ stabilizes.

For comparison with observations, we estimate the column density of H I using the following method. Although FLASH cannot distinguish H I from H II in each cell, it can track the ionization and recombination of other elements. We therefore use O I to trace H I. We calculate the quantity of H I in collisionally ionized gas from the ratio of O I to all oxygen in the cell times the quantity of hydrogen in each cell. This calculation is justified because the ratio of H I to all hydrogen is approximately equal to

the ratio of O I to all oxygen, since oxygen and hydrogen have very similar first ionization potentials (Cox, 2000) and charge exchange between O II and H I particles is common (Field & Steigman, 1971). We use this procedure to calculate the column densities of neutral hydrogen for every sightline through the HVC; these are the column densities in collisionally ionized gas. Then, in order to approximate the effect of photoionization, we subtract from these column densities the column density of hydrogen that has been photoionized. We use the resulting H I to calculate the ratio of H I to O VI.

For each epoch in a simulation, we calculate the ratio of H I to O VI over the entire cloud. These curves can be seen in Figure 2.6. This ratio is highest at the start of the simulation; this is because there has been little mixing and so the cloud consists of mostly cool, neutral gas. As the simulation evolves, the cloud mixes with the ambient gas, causing this ratio to decline until it reaches an asymptote. For comparison, the ratio of H I to O VI in the MS and Complex C are 1.7×10^4 Foxio and 5.6×10^5 Sembacho3. These two values are shown in Figure 2.6 as horizontal lines. Our simulations best replicate the MS and Complex C during the epochs when they have the same H I/O VI ratios as these clouds.

Table 2.2 lists the 12 sight lines through Complex C and the MS for which H I and O VI have been measured by Sembach et al. (2003a) and Fox et al. (2010a). We use the ratios of these observed H I and O VI column densities to determine the most appropriate epochs in the simulations for further analysis. We then determine the value of $f_{\rm OVI}$ at the corresponding epoch for each simulation for each sight line, using the values plotted in Figure 2.5. Note that $f_{\rm OVI}$ is not very sensitive to the choice of epoch. We then determine the average value of $f_{\rm OVI}$ for each sight line by averaging the corresponding $f_{\rm OVI}$ s from the ten simulations at the epochs when their H I/O VI ratio matches that of the sight line. Our results are shown in Table 2.2. Our ionization fractions are significantly lower than the maximum value of 0.22 predicted from CIE and NEI models of static gas (Sutherland & Dopita, 1993a; Gnat & Sternberg, 2007a). Until now, the maximum $f_{\rm OVI}$ in static gas has been used to determine the mass of hot ionized hydrogen in HVCs (Fox et al., 2010a; Sembach et al., 2003a). The ratio of the maximum $f_{\rm OVI}$ in static gas to our average $f_{\rm OVI}$ in dynamic gas ranges from 6.3 (Mrk 335) to 22.2 (PG1259+593). This result leads to a related increase in the mass of HVCs, as shown below.

	Table 2.2: $f_{ m OVI}$	
Clouds	Sight lines	$f_{\rm OVI}^{\rm a}$
Complex C	Mrk 279	0.023
	Mrk 290	0.019
	Mrk 501	0.031
	Mrk 506	0.036
	Mrk 817	0.023
	Mrk 876	0.031
	PG 1259+593	0.0099
	PG 1351+640	0.014
	PG 1626+554	0.031
	Average $f_{ m OVI}{}^{ m b}$	0.024
	$f_{ m OVI}$ from average H I/O VI $^{ m c}$	0.020

^a The $f_{\rm OVI}$ for each individual sight line is calculated using the H I/O VI of individual sight lines from Sembach et al. (2003a) and Fox et al. (2010a). It is the average of the values obtained from the ten simulations.

2.3.2 New Methodology for Calculating N(H)

Until now the typical method for calculating the amount of ionized hydrogen associated with observed column densities of O VI has been:

$$N(\text{H II}) = \frac{N(\text{O VI})}{\left(\frac{\text{O}}{\text{H}}\right)\left(\frac{\text{O VI}}{\text{O}}\right)}$$
(2.1)

e.g., Sembach et al. (2003a); Fox et al. (2010a) where N(O VI) is the column density of O VI, (O/H) is the metallicity, and (O VI/O) is $f_{\rm OVI}$. Without specific knowledge of the temperature distribution of gas in a cloud, it is common for researchers to adopt $f_{\rm OVI}$ as less than or equal to the maximum value

^b This $f_{\rm OVI}$ is the average value of the $f_{\rm OVI}$ of the nine sight lines in Complex C. It is calculated from the unrounded values.

^c This $f_{\rm OVI}$ is the average value of those calculated from the simulations at the epochs when H I/O VI matches the mean value of H I/O VI for the 9 sight lines listed.

in the theoretical $f_{\rm OVI}$ curve for static gas. When Fox et al. (2010a) used this method for the MS, they adopted $f_{\rm OVI} \leq 0.22$ from a static gas model (Gnat & Sternberg, 2007a). Figure 2.4 compares $f_{\rm OVI}$ vs temperature for that static model with our dynamic results. In the static model, O VI only exists in a narrow temperature range around $10^{5.5}$ K, where nearly all of the hydrogen is expected to be ionized. Hence, typically the left side of Equation 2.1 is N(H II) rather than N(H) (e.g., Fox et al. (2010a)). Sembach et al. (2003a) adopted $f_{\rm OVI} \leq 0.2$ in their analysis in Complex C and used Equation 2.1.

Fox et al. (2010a) also calculated the column densities of ionized hydrogen associated with Si IV and low ions. Their H II column densities associated with Si IV and O VI are also lower limits because the ionization fractions used are upper limits. Recognizing that there is a wide range of temperatures in a cloud, they then summed the H II column densities associated with low ions, Si IV, and O VI to achieve the total H II column density.

They made this summation because they assume that the low ions, Si IV, and O VI trace different temperature regimes and therefore different populations of H II. However, the turbulent mixing layer simulations of Kwak & Shelton (2010a) show that this is not always the case. Individual cells can have populations in several ionization states. Likewise, an example side-by-side comparison of O III and O VI from our fiducial run (Figure 2.3) shows that the spatial distributions of intermediate and high ions greatly overlap. In addition, 97% of the cloud material has an O VI volume density of 10^{-9} cm⁻³ in the same simulation and epoch.

These points raise the question of how well adding temperature phase components reproduces the total amount of hydrogen. As a simple example, consider a cloud in which there is an equal amount of oxygen in each ionization state. For the sake of argument, the total amount of hydrogen might be calculated in the following way:

$$N(\mathsf{H})_{\mathrm{calc}} = \sum_{i=1}^{9} \frac{N(\mathsf{O}_i)}{Zf_{i,max}},$$

where $N(O_i)$ is the column density of the ith oxygen ion, Z is the oxygen metallicity, and $f_{i,max}$ is the maximum ionization fraction for the ith ionization state of oxygen. Note that this $f_{i,max}$ is different

from the actual fraction of ions in the ith ionization state in this example, which is $\frac{1}{9}$. Since Z is a constant and $N(O_i)$ is equal to $\frac{1}{9}$ th of the total oxygen column density, N(O), the above equation reduces to

$$N(H)_{\text{calc}} = \frac{N(O)}{9Z} \sum_{i=1}^{9} \frac{1}{f_{i,max}}.$$

Since $\frac{N(O)}{Z}$ is equal to the actual column density of hydrogen, $N(H)_{act}$, the expression further reduces to:

$$N(H)_{\text{calc}} = \frac{N(H)_{\text{act}}}{9} \sum_{i=1}^{9} \frac{1}{f_{i,max}}.$$

If $f_{i,max}$ were set to the maximum ionization fractions for oxygen ions from the CIE tables of Gnat & Sternberg (2007a), then $\sum_{i=1}^{9} \frac{1}{f_{i,max}} = 15.3$, so $N(H)_{calc} = 1.70N(H)_{act}$. This technique overcounts the actual hydrogen column density by 70%.

Of course, it is unlikely that all 9 ionization states of oxygen would be observed for a sight line. A more practical example would be to use just a few ions that are expected to span the entire temperature range of the cloud. As an example, consider O I, C II, Si IV, and O VI. In this example, the total calculated hydrogen column density might be given as:

$$N(\mathrm{H})_{\mathrm{calc}} = \frac{N(\mathrm{O~I})}{Z_{O}f_{\mathrm{OI,max}}} + \frac{N(\mathrm{C~II})}{Z_{C}f_{\mathrm{CII,max}}} + \frac{N(\mathrm{Si~IV})}{Z_{Si}f_{\mathrm{SiIV,max}}} + \frac{N(\mathrm{O~VI})}{Z_{O}f_{\mathrm{OVI,max}}},\tag{2.2}$$

where Z_O , Z_C , and Z_{Si} are the oxygen, carbon, and silicon metallicities, respectively. As has been done frequently, the ionization fractions used here would be the maxima from Gnat & Sternberg (2007a). This calculation assumes that each ion is found in a disjoint temperature range and traces distinct gas. If each temperature range is in CIE at the temperature that maximizes the ionization fraction from static CIE gas models, then this equation would accurately capture the total hydrogen column density along the sight line. However, our dynamic simulations show that different ions can overlap significantly in temperature. There is also observational evidence of high ions such as O VI existing at a wide range of temperatures (see Section 2.4). Therefore, it is not accurate to assume that each ion traces different populations of gas. To account for this, we can define an ionization fraction of O VI that considers O VI at all temperatures

along a sight line as the total number of O VI ions divided by the total number of oxygen atoms ($f_{\rm OVI,act}$). Suppose that for a given sight line, $f_{\rm OVI,act}$ differs from the maximum ionization fraction predicted from the static gas models of Gnat & Sternberg (2007a) by a factor of $\beta_{\rm OVI}$, i.e., $f_{\rm OVI,act} = \beta_{\rm OVI} f_{\rm OVI,max}$, and likewise for the ionization fractions of O I, C II and Si IV. Then, the previous equation can be re-written as:

$$N(H)_{\text{calc}} = \frac{N(\text{O I})\beta_{\text{OI}}}{Z_O f_{\text{OLact}}} + \frac{N(\text{C II})\beta_{\text{CII}}}{Z_C f_{\text{CII.act}}} + \frac{N(\text{Si IV})\beta_{\text{SiIV}}}{Z_{Si} f_{\text{SiIV.act}}} + \frac{N(\text{O VI})\beta_{\text{OVI}}}{Z_O f_{\text{OVI.act}}}.$$
 (2.3)

However, $\frac{N(\text{O VI})}{f_{\text{OVI,act}}}$ is by definition equal to the actual column density of oxygen along the entire sight line, $N(\text{O})_{\text{act}}$. Additionally, since Z_O is the oxygen abundance along the sight line, $\frac{N(\text{O})_{\text{act}}}{Z_O}$ is equal to the total hydrogen column density along the sight line, $N(\text{H})_{\text{act}}$. The same argument applies to O I, C II and Si IV. This allows a further simplification:

$$N(H)_{\text{calc}} = N(H)_{\text{act}} (\beta_{\text{OI}} + \beta_{\text{CII}} + \beta_{\text{SiIV}} + \beta_{\text{OVI}}).$$

This example highlights the problem with using multiple ions and assuming maximum ionization fractions. As a hypothetical example, consider a sight line that contains a substantial amount of O VI, such that $\beta_{\rm OVI}=\frac{1}{2}$, and lesser amounts of O I, C II, and Si IV, such that $\beta_{\rm OI}=\beta_{\rm CII}=\beta_{\rm SiIV}=\frac{1}{4}$. These choices of values may be realistic for a sight line that contains significant portions of hot gas. Using those β values, the sum of the four actual ionization fractions would be ~ 0.64 , indicating that a substantial percentage of the metals along the sight line are in those ionization states. In this case, this method would overcount the total hydrogen column density by a factor of 1.25. On the other hand, if each ion's ionization fraction is smaller than its CIE maximum value by a factor such as 6.3–22.2, which are the factors found from our simulations for O VI, then this method results in undercounting by a factor of 1.6–5.6.

The above logic would need only slight modification if Cloudy is used to find the low ion column density and the neutral hydrogen column density is observed directly rather than deduced via O I, as in Fox et al. (2010a).

From observations alone, it is not possible to obtain values for β , so it would not be clear whether the calculated hydrogen column density is over or under counting the actual hydrogen column density. However, dynamic NEI computer simulations make it possible to calculate the ionization fraction of O VI (or any other ion) in simulated clouds. This ionization fraction takes into account O VI found throughout the whole cloud and therefore coincident with neutral and ionized hydrogen. As a result, we remove the assumption that O VI only traces hot, ionized gas in Equation 2.1 by replacing N(H II) with N(H) and using the O VI/O from our simulations. The result is Equation 2.4, which is more mathematically accurate since the metallicity is the ratio of the total amount of oxygen to the total amount of hydrogen, not just ionized hydrogen.

$$N(H) = \frac{N(O \text{ VI})}{\left(\frac{O}{H}\right)\left(\frac{O \text{ VI}}{O}\right)}.$$
 (2.4)

Table 2.3: Complex C Log Column Densities

Table 2.3. Complex & Log Column Densities							
Sight Lines	N(O VI) ^a	N(H I) ^a	N(H II) ^b	N(H I)+N(H II)	N(H) ^c	$N(H)_{\rm alt}{}^{\rm d}$	
	(cm^{-2})	(cm^{-2})	(cm^{-2})	(cm^{-2})	(cm^{-2})	(cm^{-2})	
Mrk 279	13.67	19.31	>18.68	>19.40	19.62	19.67	
Mrk 290	14.20	19.98	>19.21	>20.05	20.22	20.21	
Mrk 501	13.81	19.03	>18.82	>19.25	19.63	19.82	
Mrk 506	14.05	18.64	>19.06	>19.20	19.81	20.06	
Mrk 817	13.88	19.51	>18.89	>19.01	19.83	19.89	
Mrk 876	14.05	19.30	>19.06	>19.50	19.87	20.06	
PG 1259+593	13.72	19.95	>18.73	>19.98	20.03	19.73	
PG 1351+640	13.75	19.78	>18.76	>19.90	19.93	19.76	
PG 1626+554	14.22	19.43	>19.23	>19.64	20.04	20.23	

 $^{^{\}rm a}$ The values of N(O VI) and N(H I) are from Sembach et al. (2003a).

Since a single sight line may happen to pass through particularly cool or hot gas, we recommend using multiple sight lines when comparing with our method.

^b The values of N(H II) are calculated based on the N(O VI) and $f_{\rm OVI}$ from Sembach et al. (2003a), using the Asplund et al. (2009a) abundances.

^c For each sight line, the value of N(H) is calculated using $N(O\ VI)$ from Sembach et al. (2003a) and the calculated value of f_{OVI} for that sight line in Table 2.2.

^d For each sight line, the alternate value of N(H) is calculated using N(O VI) from Sembach et al. (2003a) and the " f_{OVI} from average H I/O VI" in Table 2.2.

2.3.3 Comparisons

To see the effect of shifting to this new methodology, we calculate N(H) for the sight lines in Sembach et al. (2003a), using Equation 2.4, our $f_{\rm OVI}$, and N(O VI) taken from the observations reported in Sembach et al. (2003a). These values are shown in column 6 in Table 2.3. We think this is the most accurate method for calculating the total hydrogen densities, but we also provide the values calculated from the averages of the $f_{\rm OVI}$ s extracted from the simulations at the epochs when the values of H I/O VI match the average values of H I/O VI from Sembach et al. (2003a).

First, we compare with published estimates for Complex C. We tabulate the observed N(H I), the N(H II) calculated using the methodologies of Sembach et al. (2003a), and the sum of these column densities. The tabulated values of N(H II) are calculated using Equation 2.1, the upper limits on $f_{\rm OVI}$ from Sutherland & Dopita (1993a) and Gnat & Sternberg (2007a), and the observed N(O VI), which is also tabulated in Table 2.3. Sembach et al. (2003a) calculated the total H II mass of Complex C using the abundances of Holweger (2001), but did not calculate individual H II column densities for their sight lines. To be consistent with our other calculations, we use the Asplund et al. (2009a) abundances to calculate those column densities.

For every sight line, N(H) calculated from Equation 2.4 and our $f_{\rm OVI}$ is larger than the observed N(H I) plus the N(H II) calculated from Equation 2.1 and the value of $f_{\rm OVI}$ chosen by Sembach et al. (2003a). On average, these column densities (column 6) are 2.6 times greater than the column density found from the observed N(H I) plus the N(H II) found from Equation 2.1 (column 5). It should be noted that technically column 5 is a lower limit.

Notice that the last two sight lines for Complex C have very similar calculated N(H). However, PG 1626+554 is O VI-rich whereas PG 1351+640 is O VI-poor. Because of the low H I/O VI ratio of PG 1626+554, it has a higher fraction of ionized gas than PG 1351+640. This is consistent with the PG 1626+554 having a higher ratio of total hydrogen to neutral hydrogen than PG 1351+640. The regions sampled by these two sight lines can be thought of as in different stages of evolution, which our prescription takes into account when calculating the total amount of material.

we make a similar calculation and analysis for Magellanic Stream. In addition, we also test how the varying metallicities of clouds and ambient materials affect the H I/O VI vs time, and thus how the $f_{\rm OVI}$ will be affected. For more details, please see .

2.4 Discussion

We observe that the value of $f_{\rm OVI}$ is strongly influenced by the interaction between hot and cool gas through dynamic mixing. Ionization and recombination under NEI conditions play a very important role in the mixed environments compared to static gas, leading to notable variations in $f_{\rm OVI}$. For static gas, $f_{\rm OVI}$ remains significant only within a narrow temperature range, peaking at a maximum value of 0.22 near 3×10^5 K. This peak value is frequently regarded as an upper limit in calculations. In contrast, our simulations reveal that $f_{\rm OVI}$ retains substantial values across a wide temperature range, spanning from $\sim2\times10^3$ K to $\sim2\times10^6$ K, over three orders of magnitude. Given the large variability of $f_{\rm OVI}$ at different locations and moments, we utilize an averaged value over the entire simulated cloud. This averaged $f_{\rm OVI}$ is calculated at the moment when the simulated H I/O VI ratio is closet the observational sightlight's derived values.

For each of our ten simulations, we calculate a value of $f_{\rm OVI}$ for a given sight line. Then we compare the 10 values of $f_{\rm OVI}$ for each observed sight line. The range for the standard deviation is small (from \sim 5 to \sim 13%), which implies that the initial conditions of the simulated clouds do not affect the $f_{\rm OVI}$ significantly. Our average $f_{\rm OVI}$ s are 4.5% - 15.9% of the peak $f_{\rm OVI}$ for static gas.

Traditionally, estimates of hydrogen content traced by O VI have relied on the value of $f_{\rm OVI}$. Our simulations reveal that O VI substantially exists in cooler regions where neutral hydrogen can also be present. This finding support us to have a new approach, one that accounts for all hydrogen, both ionized and neutral. The distinctions between our revised method (Equation 2.4) and the standard approach (Equation 2.1) are that: (1) we compute the total hydrogen column, whereas the earlier method assumes the gas is fully ionized and limited to a temperature near 3×10^5 K; (2) instead of adopting the theoretical peak

of f_{OVI} under CIE conditions, we derive a cloud-wide average from time-dependent NEI simulations; and (3) rather than yielding only a lower bound, our equation provides a direct quantitative estimate.

We apply our revised methodology to estimate N(H) along sight lines through Complex C, using the observed $N(O\ VI)$ values from Sembach et al. (2003a). Our calculated hydrogen column densities are 2.6 times larger than the combined total of the observed $N(H\ I)$ and the $N(H\ II)$ derived with the previous method discussed in Section 2.3.3.

The values of $f_{\rm OVI}$ from dynamic NEI gas are largely different from the ones from stationary NEI and CIE gas. Most notably, as mentioned above, HVCs contain considerably more hydrogen than earlier estimates predict. Our calculated column densities substantially exceed previous lower limits. As a result, mass estimate for our clouds whose $N({\rm H~II})$ are derived from O VI should also be much larger. Similarly, any HVC can be applied with this logic if its $N({\rm H~II})$ is calculated from O VI.

Another consequence of our findings relate to O VI absorbers in the low-redshift intergalactic medium. Sembach et al. (2004) studied 25 such systems along the sight line to PG1116+215 and noted that their ionization properties were similar to those seen in HVCs. Our result that a substantial fraction of OVI resides in gas cooler than 10⁵K (see Figure 2.4) aligns well with this and other observations of low-redshift extragalactic O VI systems. Tripp et al. (2008b), in their survey of 51 O VI absorbers, reported that at least onethird of the inervening components exhibit "compelling evidence" for cool gas, with temperatures below $\log(T) = 5.0$. Such findings strongly suggest these system are away from thermal equilibrium. Another evidence for cool O VI comes from Savage et al. (2014), who used data from the Hubble Space Telescope's Cosmic Origins Spectrograph (HST/COS) to examine 54 low-redshift O VI absorbers along 14 sight lines. These systems were decomposed into 85 individual components. Among the 45 components that showed a close velocity alignment with H I, 31 exhibited narrow line widths, corresponding to $\log(T) < 4.8$. This is much lower than the typical CIE temperature for O VI, which peaks at $\log(T) = 5.5$. While such narrow features were previously attributed to photoionization, turbulent and mixing between hot and cool gas can also yield O VI-bearing regions with significantly cooler temperatures than predicted by static models (Kwak & Shelton, 2010a). Together, these studies suggest that large quantities of O VI in low-redshift intergalactic absorbers are not in collisional ionization equilibrium. Therefore, we apply

our NEI-based values of $f_{\rm OVI}$ to update and refine estimates of the baryonic mass contained within these systems.

Our derived $f_{\rm OVI}$ indicates that the mass of baryons residing in low-redshift extragalactic space is substantially greater than previously predicted. Historically, estimates of the material in these O VI-bearing regions have been based on the observed O VI column densities, following a methodology analogous to that applied to HVCs (Tripp & Savage, 2000; Tripp et al., 2000; Sembach et al., 2004). In these calculations, $f_{\rm OVI}$ appears in the denominator, meaning that smaller values lead to larger estimated hydrogen columns. We recalculate the amount of materials from those earlier observations using our own values of $f_{\rm OVI}$.

These extragalactic absorbers at low redshift tend to exhibit lower H I/O VI ratios than those seen in Complex C and MS. Although our simulations do not reproduce such low ratios even until the ends of runs, we find that as time progresses, each simulation asymptotically reaches its minimum H I/O VI ratio and maximum $f_{\rm OVI}$. Thus, we adopt the $f_{\rm OVI}$ value from the final epoch of each simulation and compute the mean across all ten runs. This calculation yields an average $f_{\rm OVI}$ of 0.034. We substitute this value into Equation 7 of Sembach et al. (2004), replacing their estimate of $f_{\rm OVI} \leq 0.2$. This revision amplifies the estimated baryonic mass in O VI absorbers by a factor of 5.9, increasing $\Omega_b({\rm O~VI})$ to 0.013 h_{75}^{-1} . Such a result suggests that these absorbers harbor a vast reservoir of contents several times greater than the combined baryonic materials contained in stars and galactic gas, which is estimated to be $0.0032h_{75}^{-1}$ (Fukugita et al., 1998; Fukugita & Kawasaki, 2003). Moreover, this revised value accounts for more than one-third of the total baryonic materials predicted for the Universe (Richter et al., 2006).

A similar conclusion was reached by Shull et al. (2012), who used hydrodynamic simulations incorporating NEI effects. They found that $f_{\rm OVI}$ in dynamic gas is lower than in static models, and when applying these updated values, they also derived an larger Ω_b for the warm-hot intergalactic medium.

Since our simulations show a good correlation between H $\,$ I/O $\,$ VI and $f_{\rm OVI}$, we also develop a prescription to determine $f_{\rm OVI}$ for a sight line based on the observed N(O VI) and N(H I). For more details, please see .

2.5 Author Contributions

Both Eric Goetz and I ran the simulations analyzed in this project. Each of us ran 5 of the simulations. Both of us did the calculations tabulated in this project respectively, and finally we compared our results in order to double check each other's calculations. We also wrote the manuscript separately and then combined and merged our writings together. Eric found an empirical relation between H I/O VI and $f_{\rm OVI}$ which is described in Section 2 in Goetz et al. (2024a). Eric also tested the effect of different metallicities on H I/O VI and $f_{\rm OVI}$ which is described in Section 4 in Goetz et al. (2024b). I designed the velocity criterion described in Section 2.2. All of our post-process analysis and drafting are under the supervision of our major advisor, Dr. Robin Shelton. All co-authors agree that the work can be included in this dissertation.

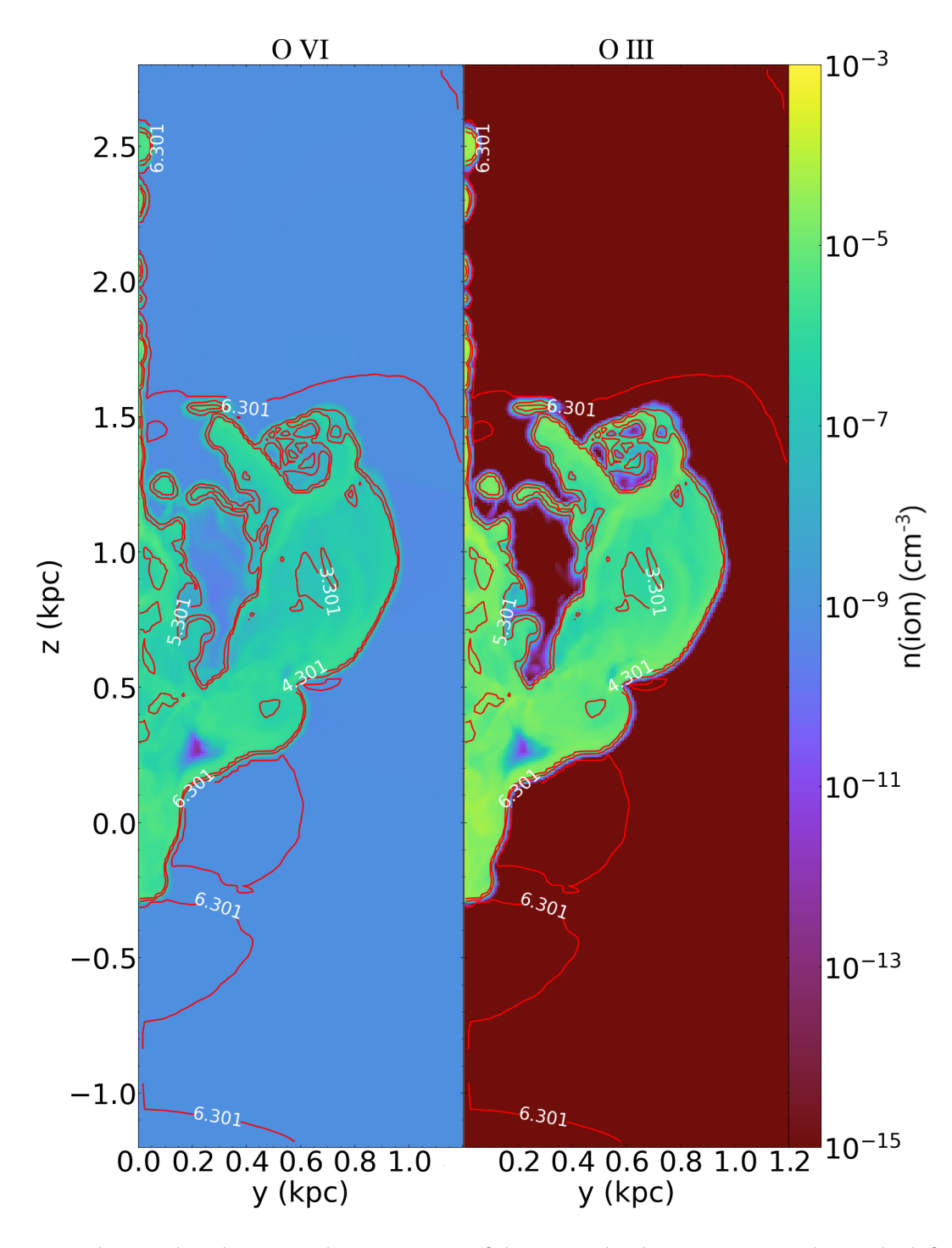


Figure 2.3: The number density and temperature of the gas in the domain at x=0 kpc. The left panel is for O VI and the right panel is for O III. The color bar represents the number density and the contours show the gas temperature. The four contour levels are 2×10^3 K, 2×10^4 K, 2×10^5 K and 2×10^6 K. Substantial fractions of O VI and O III can be seen across a wide range of temperatures, from less than 2×10^3 K to more than 2×10^5 K. There is significant overlap between O VI-rich gas and O III-rich gas.

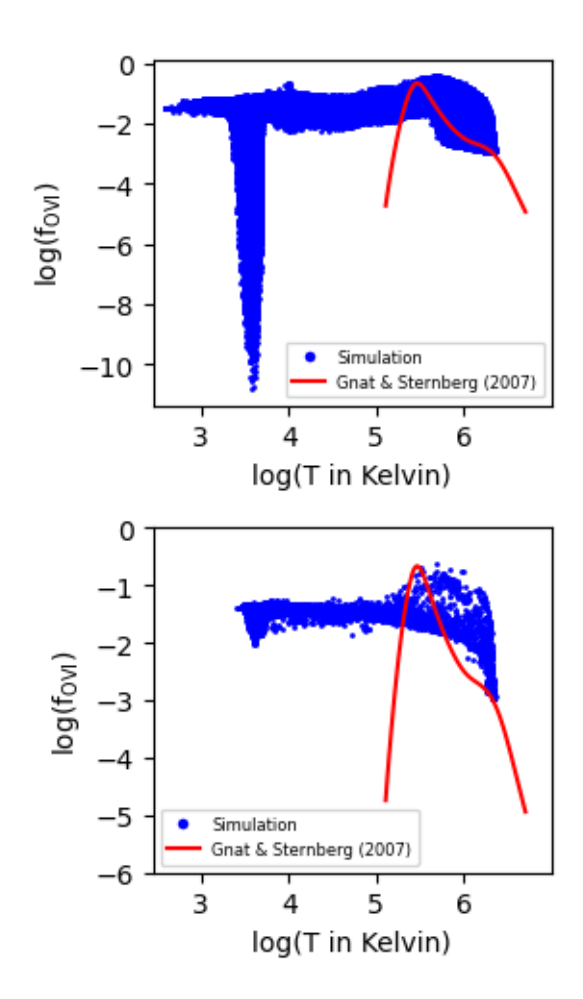


Figure 2.4: Top panel: the $f_{\rm OVI}$ and temperature are plotted with a blue dot for every cell in the cloud. Bottom panel: the $f_{\rm OVI}$ and temperature are plotted with a blue dot for every sight line through the cloud. The sight lines are oriented parallel to the x axis and the temperature is the mass-weighted average temperature along the line of sight. Both plots were made from Run 1 at 100 Myr. Only the material that met the cloud's velocity criterion was used to make these plots. For comparison, the $f_{\rm OVI}$ vs T curve for static gas is plotted in red. It was adopted from Gnat & Sternberg (2007a). O VI is confined to a narrower range of temperatures in the static curve than in our simulations, which include dynamic mixing of warm and hot gas.

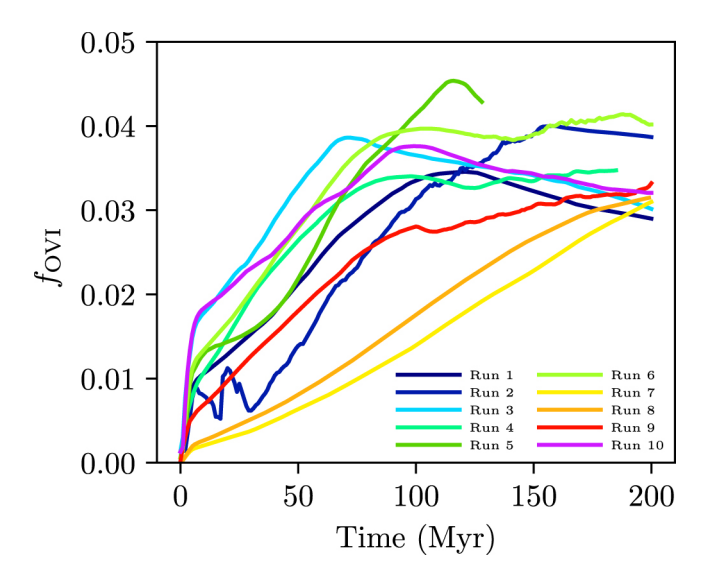


Figure 2.5: Plot of the cloud-averaged $f_{\rm OVI}$ for each simulation as a function of time. Generally, $f_{\rm OVI}$ increases with time as the cloud mixes with the ambient material.

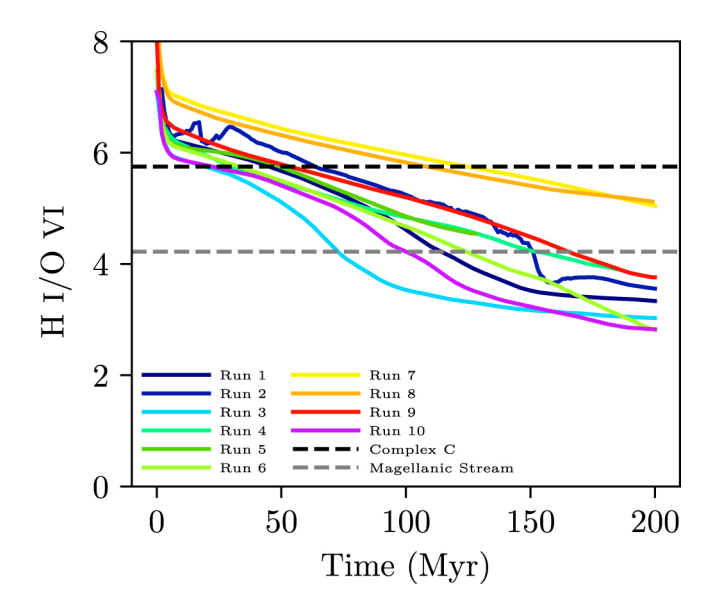


Figure 2.6: Plots of H I/O VI for each simulation as a function of time. Generally, H I/O VI decreases with time as hydrogen is ionized and $f_{\rm OVI}$ increases (see Figure 2.5). Also shown are the average observed H I/O VI ratios for Complex C (Sembach et al., 2003a). The discussion for Magellanic Stream can be seen in Goetz et al. (2024a).

CHAPTER 3

DEMYSTIFYING STRANGE O VI LINE WIDTHS WITH HYDRODYNAMIC SIMULATIONS I

¹Wang, C., Goetz, E. & Shelton, R. L., 2025, Submitted to the Astrophysical Journal and currently is under revision.

Abstract

We present a survey of O VI broadening parameters obtained from hydrodynamic simulations that model the mixing between the High Velocity Clouds and the circumgalactic medium and track the NEI populations of the ions. We run 10 simulations with various physical conditions of the clouds and ambient environments, so that our results can be compared to observations of various cloud environments. Synthetic spectra are created for the simulated sight lines that contain O VI. The range of our Doppler broadening parameter, b, is from \sim_5 km s⁻¹ to \sim 69 km s⁻¹. We calculate the thermal and non-thermal contributions to the b values. Both b and the thermal contribution to b can be substantially less than the CIE value. These narrow line widths are due to the time delay in recombination from O VI to O V in mixing regions, which results in substantial amounts of O VI at temperatures below the 2.93 \times 10⁵ K CIE temperature. Our results show that non equilibrium collisional ionization and mixing can produce the narrow line widths that are seen in multiple observations.

3.1 Introduction

The Doppler broadening parameter, *b*, plays an important role in understanding the thermal and kinematic properties of astrophysical environments. Wide profiles often appear in systems with active heating or strong dynamical interactions, such as the Circumgalactic Medium (CGM) and Intergalactic Medium (IGM) (Werk et al., 2016; Stocke et al., 2019; Qu et al., 2024). High Velocity Clouds (HVCs) interacting with the Galactic halo can also exhibit broad lines, reflecting a combination of thermal motion and turbulence (Lehner & Howk, 2007; Fox et al., 2010b)

An interesting puzzle arises: why are some observed line widths broad and some extremely narrow, when the atoms, such as O VI, are highly ionized and presumably hot? Such narrow line widths are found in the spectra from HVCs (Zech et al., 2008; Yao et al., 2011b), the IGM (Wakker & Savage, 2009; Savage et al., 2014) and the CGM of other galaxies (Ahoranta et al., 2021; Haislmaier et al., 2021; Qu et al., 2024).

To solve this puzzle, we calculate *b* values from hydrodynamic simulations of HVCs moving through the CGM. The simulations track the hydrodynamic evolution as cool cloud material is ablated and hot ambient material is entrained into the cool clouds. The simulations also track the ionization and recombination of oxygen in a time dependent manner, determining the non-equilibrium ionization (NEI) population in every ionization level of oxygen.

As a result of NEI and mixing, there are substantial populations of both cool O VI and hot O VI in the clouds. Meanwhile, there are also strong velocity gradients that contribute to the total line width along some sight lines.

Our simulations reproduce a wide range of line widths, including narrow values (b < 10 km/s) similar to those observed by Savage et al. (2014). We also calculate the thermal broadening. By removing it from the total line width, we determine the contribution from the turbulent mixing.

In Section 3.2, we present our simulation settings and the initial physical conditions. In Section 3.3, we explain our analyses of the simulations and the calculations of the broadening parameters. In Section 3.4, we compare our results to multiple observations and discuss our physical insights.

3.2 Model

We use FLASH version 4.6.2 (Fryxell et al., 2000a) to simulate the hydrodynamics of HVCs moving through the ambient environment. We use FLASH's NEI module to track the time-dependent ionization state populations of the metals. We also include radiative cooling, calculated using the CIE cooling curve from Sutherland & Dopita (1993b) with [Fe/H] = -0.5.

We run our simulations in a rectangular domain with lengths 2.4 kpc \times 1.2 kpc \times 10.8 kpc in the \hat{x} , \hat{y} , and \hat{z} directions, respectively. The domain is subdivided into 18 blocks, each with a length of 1.2 kpc. Each of these blocks is initially subdivided into many small cells. Refinement occurs due to adaptive mesh refinement, leading to a minimum cell size of 9.375 pc in each direction. During the simulations, each cell will also be divided into 8 zones in each direction.

We place the origin midway between the lower and upper x boundaries, on the lower y boundary, and 1.2 kpc above the lower z boundary. We place the center of the cloud at the origin.

Only half of the cloud is within the computational domain. The other half of the cloud is outside the domain, but, owing to the reflection conditions we have imposed at the lower y boundary, is symmetric to the simulated half. We allow material to exit the domain through the upper and lower x boundaries, upper y boundary, and upper z boundary. In order to simulate clouds moving quickly through the ambient material, yet avoid having an impractically large domain, we let the cloud be stationary and the ambient gas move past it with a large velocity. Thus, the simulations use a wind tunnel configuration, with ambient material entering the domain through the lower z boundary. At the beginning of each simulation, the cloud is stationary with respect to the domain.

To distinguish between cloud and ambient gas, we initially set each to have a different metallicity. We start the ambient environment with solar metallicity gas and start the cloud with a I/1000 of that metallicity. During post-processing, we reset the initial cloud metallicity to 0.I solar and the initial ambient metallicity to 0.7 solar, assuming the solar abundances of Asplund et al. (2009b). Details on the metallicity rescaling process can be found in Goetz et al. (2024a).

Table 3.1: Simulation Parameters						
Simulation	$n(H)_{cl}$	$T_{ m cl}$	$n(H)_{am}$	T_{am}	$r_{ m cl}$	velocity
	(cm^{-3})	(K)	(cm^{-3})	(K)	(pc)	(km s^{-1})
Run 1	0.4	5000	0.001	2×10^{6}	500	150
Run 2	0.4	5000	0.001	2×10^{6}	500	100
Run 3	0.4	5000	0.001	2×10^6	300	150
Run 4	0.4	5000	0.001	2×10^{6}	500	300
Run 5	0.04	5000	0.0001	2×10^6	500	150
Run 6	0.2	5000	0.001	1×10^{6}	500	150
Run 7	2.0	1000	0.001	2×10^{6}	500	150
Run 8	I.O	1000	0.001	1×10^{6}	500	150
Run 9	0.67	3000	0.001	2×10^{6}	500	300
Run 10	0.222	9000	0.001	2×10^{6}	500	150

In order to cover a wide range of HVC parameters, we run ten simulations with various cloud and ambient densities and temperatures, cloud radii, and wind speeds. The parameters for these simulations are given in Table 3.1. The cloud density and temperature given in Table 3.1 are the values at the center of the cloud. The cloud density decreases with distance from the center of the cloud until it reaches the ambient values. The shape of the density profile is given by the hyperbolic tangent function described in Gritton et al. (2014b), with a scale length of 50 pc. The cloud and ambient environment start in pressure equilibrium. Therefore, the cloud temperature rises towards the edge of the cloud until it reaches the ambient temperature, governed by a complementary hyperbolic tangent function. At the beginning of the simulation, the metallicity and velocity transition from the cloud's values to the ambient values at the locations where the hydrogen number density is $0.99n_{\rm am} + 0.01n_{\rm cl}$. Here, $n_{\rm am}$ is the initial ambient hydrogen number density and $n_{\rm cl}$ is the initial cloud hydrogen number density.

During the simulations, the cloud material mixes together with the ambient material. In the real world, observers would distinguish the cloud material from the ambient material by differences in velocity. Likewise, we follow similar logic. We define our own velocity criterion. The details of our velocity criterion can be found in (Goetz et al., 2024a).

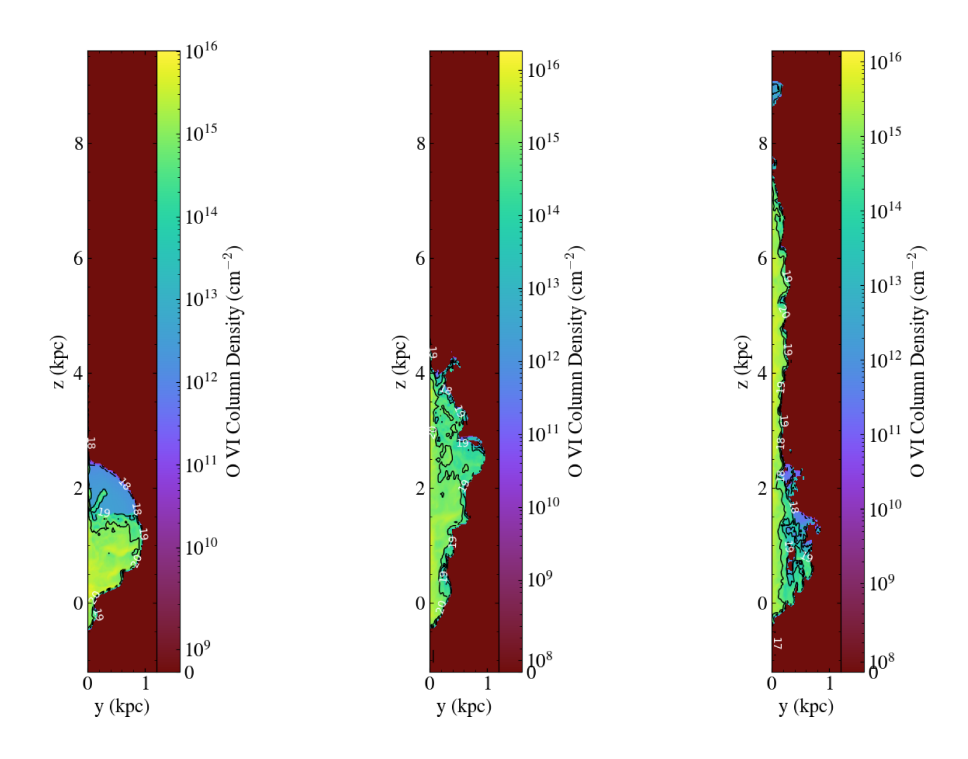


Figure 3.1: Column density map of O VI at 100, 150 and 200 Myrs for Run 1. The color bar presents the value of the O VI column density, N(O VI). The contour lines and their labeled values represent the hydrogen column density

3.3 Results

We created synthetic spectra for every simulation at 3 epochs, t=100, 150, 200 Myrs. Figure 3.1 shows one of our simulations at those three epochs. Each spectrum comes from a sight line that passes horizontally, vertically or diagonally though the cloud. Figure 3.2 shows the sight lines superimposed on a temperature map of Run 1 at 100 Myrs.

In order to calculate the synthetic spectra, we first assumed that the gas in every cell along a line of sight has a Maxwell-Boltzmann distribution of velocities, centered on the cell's bulk velocity. We calculated the Maxwell-Boltzmann distribution along the line of sight from the formula

$$f(v) = \frac{1}{\sigma\sqrt{2\pi}}e^{-\frac{(v-\mu)^2}{2\sigma^2}},\tag{3.1}$$

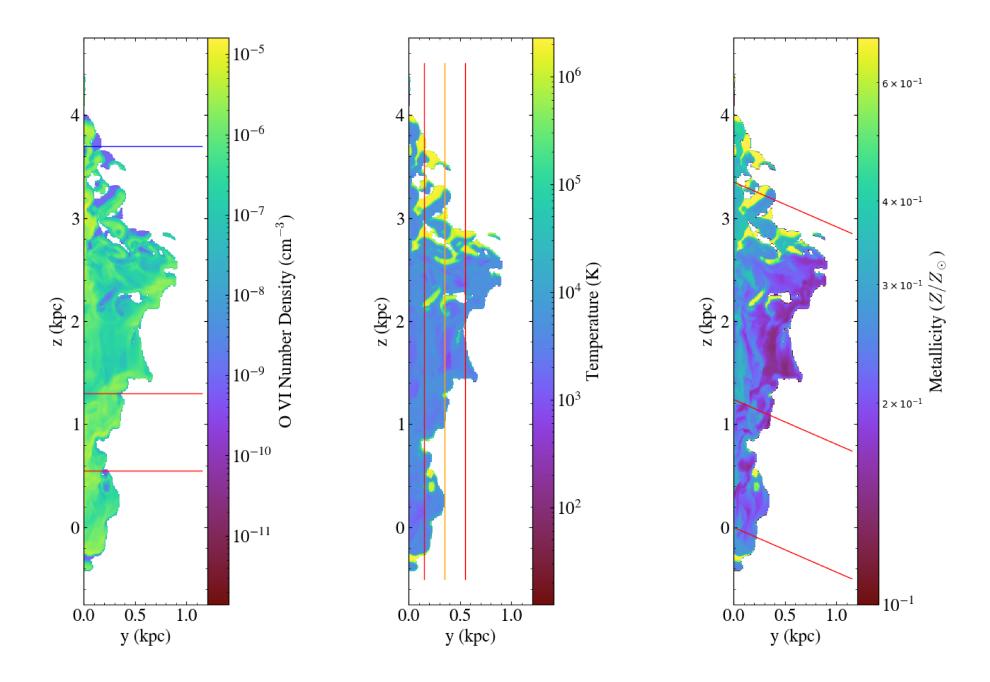


Figure 3.2: Left Panel: O VI number density in the cloud, along a slice through the domain in the x=0 plane at 150 Myrs from Run 1. The color bar displays the O VI number density. Middle Panel: Temperature in the cloud, along a slice through the domain in the x=0 plane at 150 Myrs from Run 1. The color bar displays the temperature. Right Panel: Metallicity in the cloud, along a slice through the domain in the x=0 plane at 150 Myrs from Run 1. The color bar displays the metallicity. The red, blue and orange lines are the simulated sight lines. The orange line in the middle panel is the sight line in Figure 3.3, and the blue line in the left panel is the sight line in Figure 3.4.

where μ is the cell's bulk velocity along the line of sight and σ is the one-dimensional velocity dispersion of gas in the cell due to thermal broadening. The one-dimensional velocity dispersion is calculated by

$$\sigma = \sqrt{\frac{kT}{m}},\tag{3.2}$$

where k is the Boltzmann constant, T is the temperature of the gas in the cell and m is the mass of an oxygen atom.

Figure 3.3 and Figure 3.4 show the one-dimensional Maxwell-Boltzmann distributions of all the cells along the sight lines in z and y directions in Run 1 at 150 Myrs that are identified in Figure 3.2. These plots show the thermal broadening effects for the cells in addition to their bulk velocities.

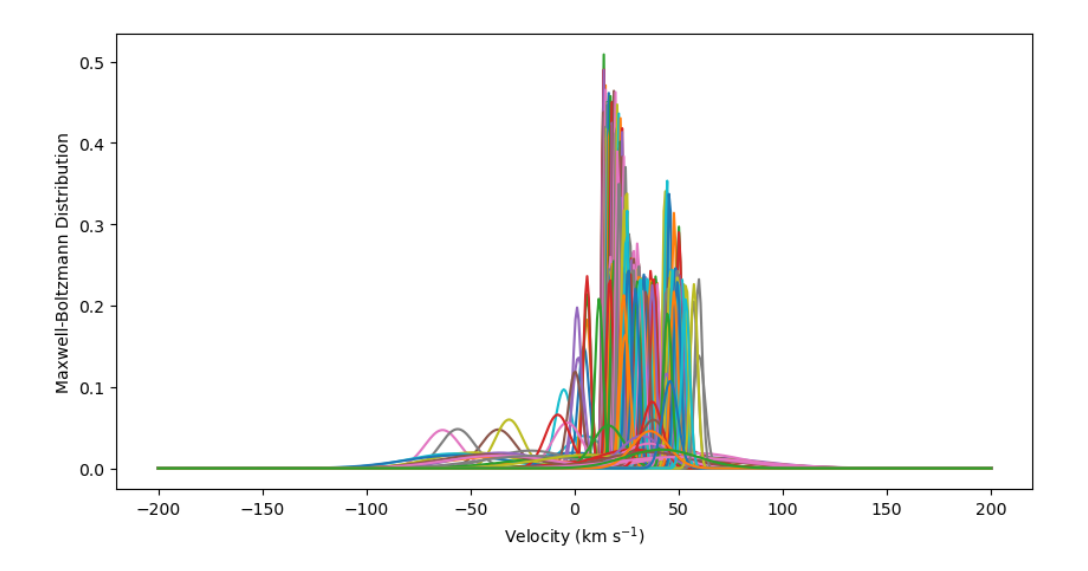


Figure 3.3: Maxwell-Boltzmann distributions for all the cells along a sight line, calculated from their temperatures and bulk velocities. Each curve is for a single cell. The location of this sight line is marked in orange in the second panel of Figure 3.2. In this plot, we can see two obvious clusters of cool gas with one centered around 20 km s⁻¹ and the other one centered around 45 km s⁻¹ The curves have various colors in order to separate them visually.

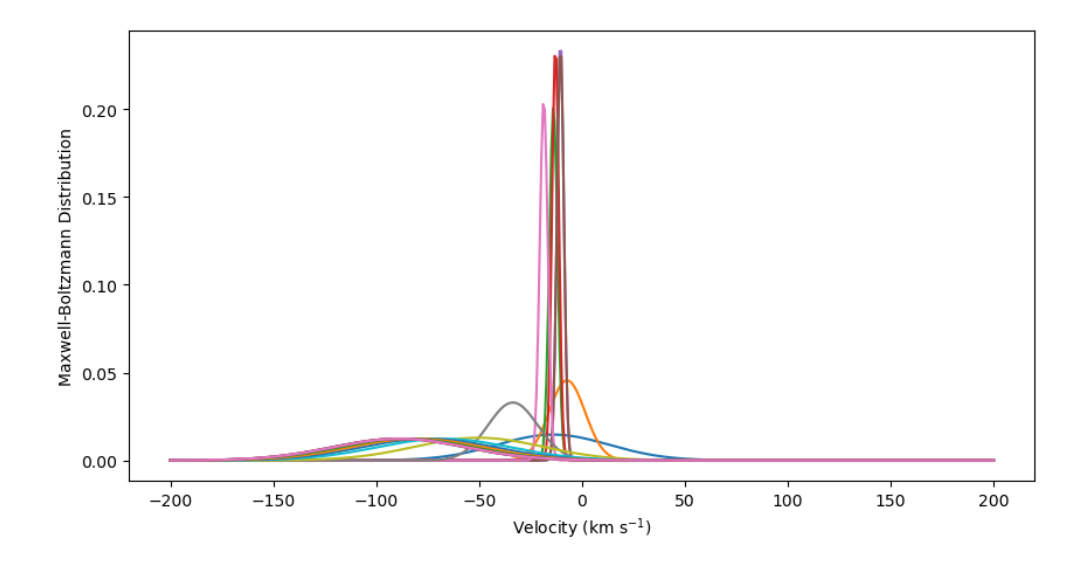


Figure 3.4: Maxwell-Boltzmann distributions for all the cells along a sight line, calculated from their temperatures and bulk velocities. Each curve is for a single cell. The location of this sight line is marked in blue in the first panel of Figure 3.2. The curves have various colors in order to separate them visually.

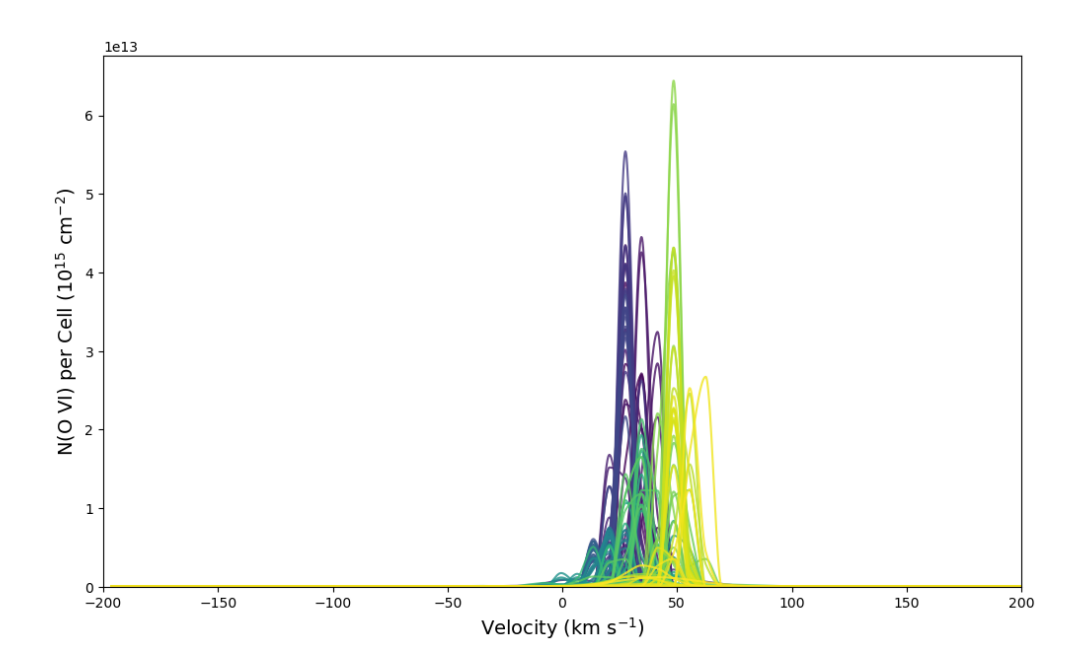


Figure 3.5: O VI distributions for individual cells along a sight line. Each curve is for a single cell. The location of this sight line is marked in orange in the middle panel of Figure 3.2. The curves have various colors in order to separate them visually.

Considering that the bulk velocity of any given cell need not match the bulk velocities of the other cells along the line of sight, we created a column density array in which the contributions of each cell could be combined. The array spans the velocity range expected for the line of sight and is segmented into many "bins", each of which spans I km s $^{-1}$. For any given cell, the fraction of material within any given velocity bin is the integral of f(v)dv between the bin's lower and upper velocity boundaries. We multiplied these fractions by the O VI column density of the cell to get each cell's contribution of N(O VI) within each velocity bin. Thus, every single cell has an array of the amount of O VI with respect to the center value of the velocity bin. Plots of these arrays represent the contribution of O VI gas from individual cell along the sight line with the thermal broadening effect. Figure 3.5 shows an example from the sight line in the z direction which is labeled in Figure 3.2.

These figures give us a clearer sense of the velocity range of the material along the sight lines. The variety of velocity centers of these Maxwell-Boltzmann distributions indicates that there are multiple velocity components. For example, in Figure 3.3 there appear to be two clusters of gas, one centered at

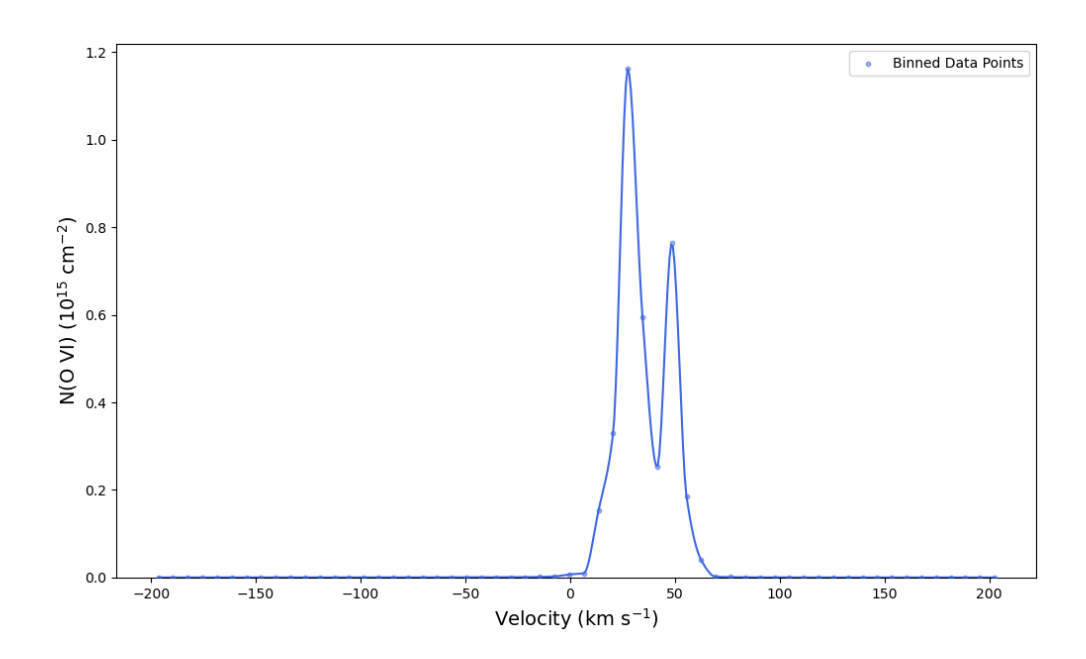


Figure 3.6: O VI spectrum for the sight line that is identified in Figure 3.2. It is calculated by summing the individual curves in Figure 3.5

larger velocity and the other one centered at smaller velocity. We sum the distributions in Figure 3.5 to create the spectra of N(O VI) vs. velocity in Figure 3.6 Here, the two components are obvious, one at higher velocity and the other at lower velocity. They match with the two clusters of cells in Figure 3.3. We find a similar correspondence between clusters of cells in Figure 3.4 and velocity components in the summed spectra (Figure 3.7). These figures further show that there are multiple overlapping components along individual sight lines.

In a real observation, astronomers will extract the summed spectra and then try to disentangle the velocity components. This is often done with absorption spectroscopy. We use Trident (Hummels et al., 2017), to simulate an absorption spectra for sight lines through our domain. The instrument we assume when running Trident to simulate the observational sight line is the Space Telescope Imaging Spectrograph E140M. We choose this instrument because it has a good resolution (7 km s⁻¹) (Rickman & Brown, 2024) and a large amount of O VI observational data has been obtained with it, (e.g. Tripp et al. (2008a)). One issue is that O VI's rest frame wavelengths are outside the bandpass of the E140M grating. Thus, we shift O VI's wavelengths into the E140M grating's bandpass by adjusting the redshift of the simulated material.

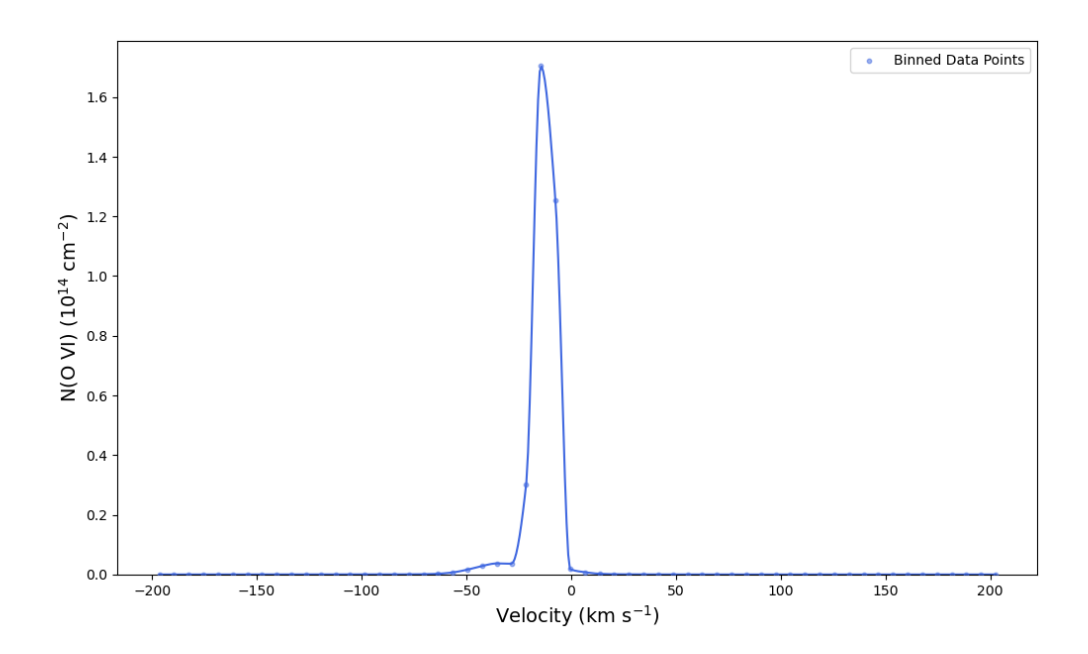


Figure 3.7: O VI spectrum from the sight line that is identified in Figure 3.2. It is calculated by using the same method as for Figure 3.6 but with its own O VI distributions for individual cell.

We use a value of z=0.3 and after this shift our O VI's wavelengths are within the range from 1300 Å to 1350 Å where the E140M grating's sensitivity peaks. In addition, a survey done by Tripp et al. (2008a) found a median redshift of z=0.217 for intervening O VI systems and a median redshift of z=0.267 for proximate absorbers. Considering their redshift values and the E140M sensitivity range, z=0.3 is a reasonable choice. We remove this redshift later in our analysis in order to produce final spectra.

In our Trident analysis, we incorporate the tabulated line spread function (LSF) of the STIS E140M provided by the Space Telescope Science Institute into Trident. We use the $0.06'' \times 0.2''$ aperture, which was the most commonly used aperture in the Tripp et al. (2008a) survey. Combining all of these effects, the resolution of our final spectra is close to 7 km s⁻¹, which is the resolution of the E140M grating.

We use Trident to calculate the optical depth of the O VI material, τ , and make a plot of it vs. velocity (Figure 3.8). Compared with Figure 3.6 made directly from our FLASH data, the general shape and structure of the Trident plot are preserved while the instrumental LSF effect from Trident change the shapes and broaden the line widths in Figure 3.8.

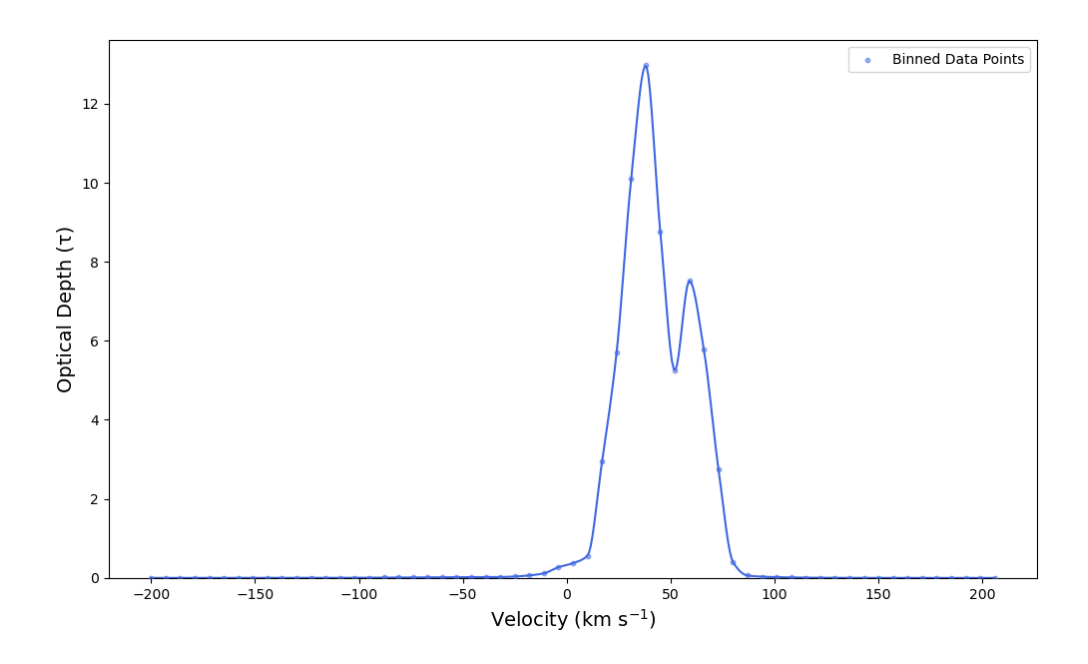


Figure 3.8: Plot of optical depth, τ vs. velocity from Trident results. Trident models the LSF effect and this is why the shape of the curve here is slightly different from the one in Figure 3.6.

We then plot the final spectra of normalized flux vs. velocity and use a Voigt profile in the Python library, SciPy, to identify and fit individual components. Figure 3.10 and Figure 3.11 show the absorption spectra from two sight lines labeled in Figure 3.2. In Figure 3.10, the two deep components are identified; they clearly correspond to the two obvious peaks plotted in Figures 3.5 and 3.8. A third component which has a wide width is also identified. This component represents the mixed gas which is spread out along the sight line and is outside the two clusters of cool gas. Since this sight line is in the z direction, it intersects the most cloud material, as shown in Figure 3.2, resulting in more spectral structures. In Figure 3.11, one deep, narrow component and one shallow, broad component are identified. Similarly, the identified components in Figure 3.11 correspond to the two features in Figure 3.7. The broad component can be explained by the obvious hot gas which is shown in Figure 3.2.

The fitting results also include the estimated velocity centers, v_c , Doppler broadening parameters, b, and $\log N(OVI)$ for individual components. Since b embodies the effects of both thermal broadening and velocity gradients, we separately estimated the contribution from thermal broadening, b_T with the

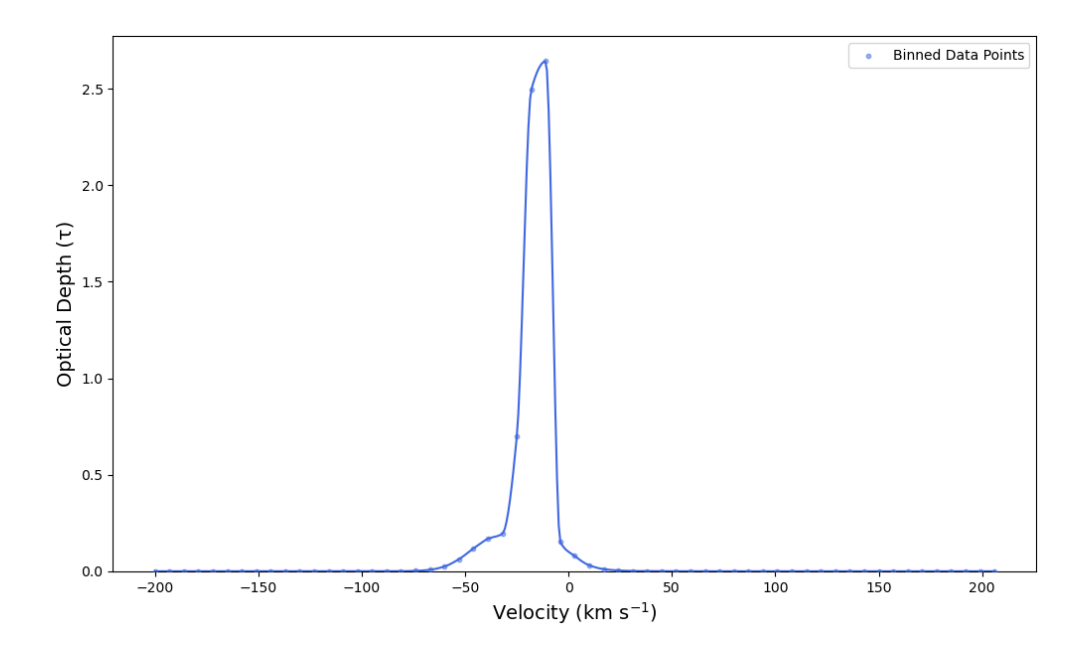


Figure 3.9: Plot of optical depth, τ vs. velocity from Trident results. Trident models the LSF effect and this is why the shape of the curve here is slightly different from the one in Figure 3.7.

following method. We first calculate the velocity range for each component as $(v_c - 2.5 \sigma, v_c + 2.5 \sigma)$, where σ is the standard deviation of the line profile for each component. Then we identify the cells within this range along the sight line in our simulation domain. Next, for each individual velocity component, we calculate the weighted average temperature of O VI in these cells. This weighted average temperature, T_w , is calculated from

$$T_w = \frac{\sum_i N(\text{O VI})_i T_i}{\sum_i N(\text{O VI})_i},$$
(3.3)

where i refers to any given cell that is within the velocity range along the chosen sight line, T_i is the temperature of that cell, and $N(O\ VI)_i$ is the column density of $O\ VI$ of that cell. The calculation of T_w for any given component uses the cells from its specified velocity range. Consequently, for components that overlap, the cells in the shared velocity region would contribute to the calculation for all involved components. However, the shared cells could lead to an underestimate or overestimate of each component's temperature. This is a bigger problem for the calculation of T_w of broad, shallow components from hot,

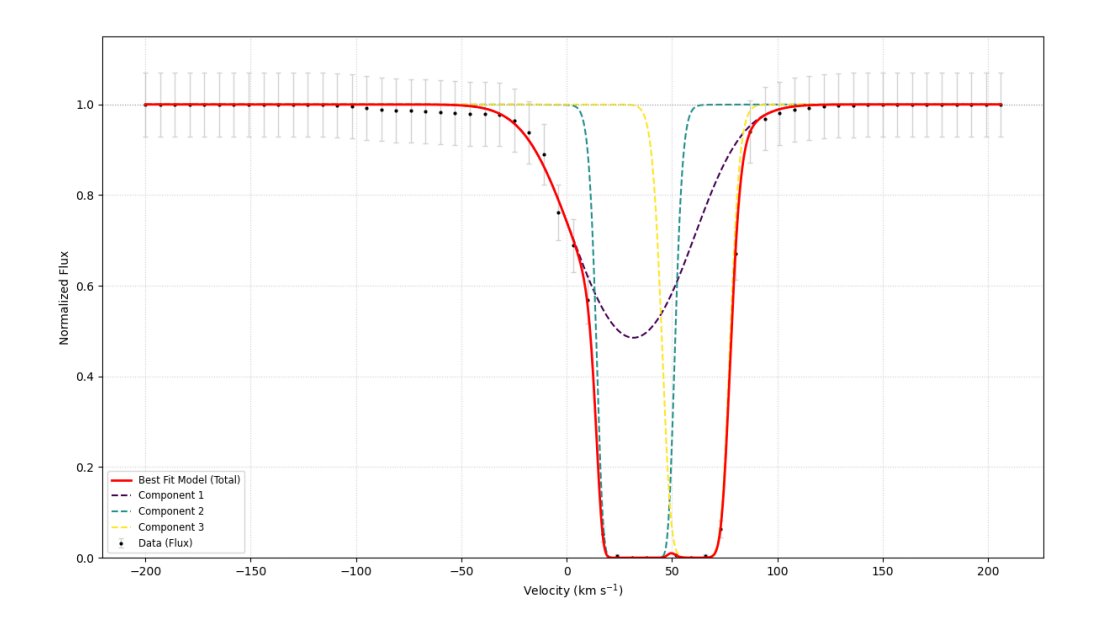


Figure 3.10: Final O VI absorption spectrum for the sight line in orange labeled in Figure 3.2. The total line profile and each component are fitted by a Voigt profile in the SciPy library in Python.

diffuse gas, like Component 1 in Figure 3.10, than the calculation of T_w of narrow, deep components from cool, dense gas. To avoid this issue for hot components, we only use the cells outside the velocity ranges of the other components when we calculate the values of T_w for the broad components. Then we calculate the thermal contribution, b_T , as

$$b_T = \sqrt{\frac{2kT_w}{m_o}},\tag{3.4}$$

where k is the Boltzmann constant, m_o is the mass of an oxygen atom.

By subtracting b_T from b in quadrature, we obtain the broadening parameter associated with the velocity gradients, b_{vg} , i.e.,

$$b_{vg} = \sqrt{b^2 - b_T^2}. (3.5)$$

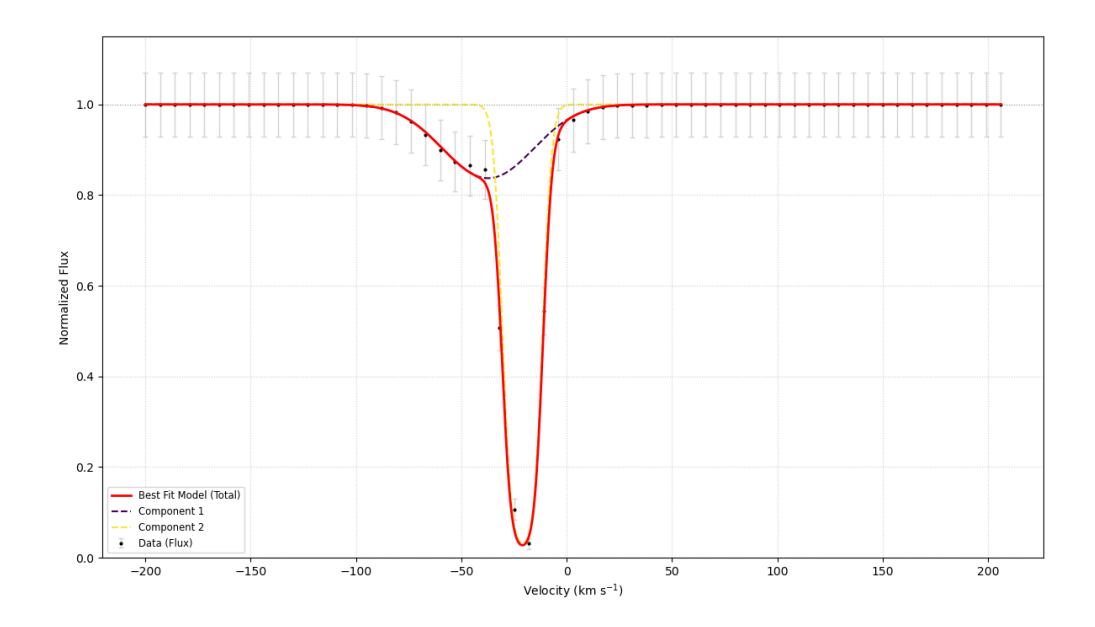


Figure 3.11: Final O VI absorption spectrum for the sight line in blue labeled in Figure 3.2. The total line profile and each component are fitted by a Voigt profile in the SciPy library in Python.

The values of v_c , b, b_T , b_{vg} , $\log N(OVI)$ and the total OVI column density directly calculated from our runs, N(O VI)_{sim} for 27 simulated sight lines through Run 1 are tabulated in Table 3.2, 3.3 and 3.4. The values for Run 2 to 10 are tabulated in the Appendix.

The values of b from Run 1 span from ~ 6 km s⁻¹ to ~ 93 km s⁻¹. This range is wide, but similar to those of the other 9 runs. Many sightlines have much wider or narrower line widths than expected from thermal broadening in CIE gas. In CIE O VI is most prevalent at $T_{CIE} = 2.93 \times 10^5$ K (Gnat & Sternberg, 2007b), hence $b_{CIE}=17.4$ km s⁻¹. For the sight lines that have $b>>b_{CIE}$, there is a clear trend that turbulent mixing dominates the total broadening. In these regions, b_{vg} is usually larger than b_T . Even for hot, mixed gas, the total line widths are still mostly due to turbulent mixing and velocity gradients. Even for the broad components, it is still rare for the temperature to reach an order of $\sim 10^6$ K.

Sight lines that have $b << b_{CIE}$ and a significant amount of O VI have gas temperatures below 10^5 K. In these sight lines, b_{vg} is also greater than b_T , indicating that mixing plays a more important role than thermal broadening. Since many cells' temperatures along these sight lines are under 10^4 K, thermal broadening should have a very limited effect on b. The reason why O VI can exist in such cool places is

Table 3.2: Run 1 at 100 Myrs

Direction		Components					$\log N(OVI)_{sim}$
		v_c (km s ⁻¹)	$b (\mathrm{km} \mathrm{s}^{-1})$	b_T (km s ⁻¹)	b_{vg} (km s ⁻¹)	$\log N(OVI)$	TOS IV (O V I)sim
у	уı	-21.8±0.2	8.6±0.2	2.2	8.3	13.87±0.01	15.18
		-1.4±0.1	13.4±0.2	2.0	13.2	14.65±0.01	
	y2	-3.1±0.1	15.9±0.2	2.4	15.7	14.70±0.01	14.96
	у3	-41.8±6	74.6±12.4	27.0	69.5	14.21±0.08	14.71
		-41.2±0.9	16.0±2.3	7.9	13.9	14.17±0.07	
		-4.7±0.8	6.4±1.4	3.8	5. I	13.94±0.07	
Z	ZI	-47.6±0.5	14.5±1.9	4.0	13.9	15.55±0.28	15.70
		-13.1±2.1	71.1 ± 2.7	24.I	66.9	14.73±0.03	
		7.4±0.5	13.1±1.4	2.9	12.8	14.81±0.10	
	Z2	-57.8±1.0	9.7 ± 1.7	4.9	8.4	13.66±0.08	15.28
		1.1±0.6	29.5±1.4	2.8	29.4	15.11±0.05	
	Z3	34.6±0.1	16.8±0.4	6.7	15.4	15.01±0.03	15.09
oblique	obliquei	-2.0±0.I	8.7±0.1	2.9	8.2	14.17±0.00	14.70
		6.o±0.1	21.4±0.1	3.7	21.1	13.31±0.00	
	oblique2	-70.2±8.9	93.0±21.7	20.5	90.7	13.82±0.10	14.93
		-22.9±0.4	14.7±0.7	2.5	14.5	14.25±0.02	
		3.7±0.2	8.8 ± 0.4	2.2	8.5	14.19±0.03	
	oblique3	11.4±1.1	22.0±3.0	4. I	21.6	14.79±0.09	14.95
		33.0±0.1	82.6±17.9	13.4	81.5	14.27±0.11	

that mixing brings highly ionized ambient material into contact with cool material. Heat is transferred from the hot gas to the cool gas. Since the density of the entrained ambient gas is much smaller than that of the cool cloud gas, the added heat does not greatly increase the temperature.

Another important reason for these cells remaining cool is radiative cooling (Kwak & Shelton, 2010b). Kwak & Shelton (2010b) analyzed the effects of non-equilibrium ionization and recombination in radiatively cooled, turbulent gas. The gas temperatures and densities in their suite of simulations overlapped those of ours. They found that radiative cooling is very effective and NEI increased the ionization fraction of O VI relative to the fraction in CIE gas at the same temperature. In an example cell, whose temperature was $\sim 1.5 \times 10^5$ K, the ionization fraction of O VI was ~ 100 times greater in NEI calculations than in CIE calculations. On average, along examined sightlines, the NEI O VI ionization fraction was approximately twice the CIE O VI ionization fraction. We expect that these phenomena happen in our simulations as

Table 3.3: Run 1 at 150 Myrs

Direction		Components					$\frac{1}{1} = M(O UI)$
		v_c (km s ⁻¹)	$b (\mathrm{km} \mathrm{s}^{-1})$	b_T (km s ⁻¹)	b_{vg} (km s ⁻¹)	$\log N(OVI)$	$\log N(OVI)_{sim}$
y	уı	-21.9±0.1	8.3±0.2	5.8	5.9	13.25±0.01	14.96
		-2.2±0.1	9.4±0.1	2. I	9.2	14.26±0.01	
	y2	-13.3±0.1	16.9±0.3	2. I	16.8	14.91±0.02	15.03
	у3	-37.3±3.2	41.3±4.3	17.7	37.3	13.55±0.06	14.53
		-21.0±0.1	10.7±0.2	5.4	9.2	14.26±0.01	
Z	ZI	11.9±0.3	26.5±0.7	3.4	26.3	15.69±0.01	15.84
		60.7±0.3	17.1±0.5	6.2	15.9	14.79±0.03	
	Z2	31.6±1.8	47.6±1.8	16.7	44.6	14.23±0.05	15.54
		32.8±0.3	13.3±0.8	3.4	12.9	15.39±0.06	
		61.4±0.2	14.2±0.4	4.0	13.6	14.84±0.02	
	Z3	-7.7±2.2	17.8±4.6	16.6	6.4	12.83±0.10	15.21
		42.2±0.2	25.I±0.4	3.7	24.8	15.06±0.20	
		72.2±0.8	10.4±1.1	8.2	6.4	13.33±0.10	
oblique	obliquei	-9.5±0.1	9.7±0.1	1.9	9.5	14.34±0.01	14.93
		17.3±0.8	16.0±1.8	I2.O	10.6	12.53±0.04	
	oblique2	5.6±0.1	17.1±0.3	2. I	17.0	15.13±0.02	15.12
		42.3±0.4	10.4±1.0	4.0	9.6	13.20±0.03	
	oblique3	28.1±0.1	9.2 ± 0.2	3.3	8.6	14.12±0.01	14.85
		45.5±0.1	10.4±0.1	4.8	9.2	14.37±0.01	
		59.3±1.1	58.9±1.5	27.6	52.0	13.82±0.01	

Note: The entries under "Components" correspond to the sight lines labeled in Figure 3.2. The first, second, and third entries for sight lines in the y direction are related to the lowest, middle and highest sight lines in the first panel of Figure 3.2. Likewise for the oblique sight lines and the third panel of Figure 3.2. The first, second, and third entries for sight lines in the z direction are related to the leftmost, middle, rightmost sight lines in the second panel of Figure 3.2.

well. I.e., NEI, mixing and radiative cooling enable a significant amount of cool O VI to exist on some sight lines, resulting in $b_T < b_{vg}$.

3.4 Discussion

We investigate the impacts of NEI and mixing on the presence of O VI along simulated sight lines. We find a notable trend in the oxygen ion population in cells with temperatures below 10⁴ K. Most of these

Table 3.4: Run 1 at 200 Myrs

Direction			$\log N(OVI)_{sim}$				
		v_c (km s ⁻¹)	$b (\mathrm{km} \mathrm{s}^{-1})$	b_T (km s ⁻¹)	b_{vg} (km s ⁻¹)	$\log N(OVI)$	$\int \log IV (O V I)_{sim}$
y	уı	-20.8±1.2	30.9±1.6	3.7	30.7	13.07±0.03	14.64
		-10.0±0.1	$8.8\pm$ o.ı	3. I	8.2	14.21±0.01	
	y2	-25.6±1.9	18.8±2.0	2.3	18.7	14.50±0.07	15.06
		-6.1±0.7	10.7±1.4	2.2	10.5	14.83±0.17	
	у3	-3.3±0.1	7.9±0.1	1.7	7.7	14.03±0.01	14.7
Z	ZI	46.4±0.3	36.1±1.5	2.4	36.0	16.60±0.18	16.47
	Z2	70.2±0.1	25.4±0.4	3.5	25.2	15.95±0.01	15.83
	Z3	96.3±0.2	31.6±0.4	18.3	25.8	13.59±0.01	13.47
oblique	obliquei	-1.9±0.1	8.4±0.1	2.0	8.2	14.08±0.01	14.51
		25.4±0.1	13.3±0.3	2.2	13.1	13.85±0.01	
	oblique2	п.8±о.і	7.5±0.2	2.2	7.2	14.11±0.02	14.78
		21.0±0.7	19.3±0.7	17.9	7.2	13.88±0.03	
	oblique3	15.4±0.1	14.3±0.1	1.8	14.2	14.87±0.01	15.46
		53.9±2.4	34.0±5.2	17.7	29.0	13.14±0.06	

cells have more O VII ions than O VI ions. Considering the prevalence of O VII, the cool O VI is likely the result of recombination from higher ionization states.

To explain this process, consider hot diffuse ambient gas, which has a temperature of 2×10^6 K and is rich in O VII and O VIII. It mixes with cold dense cloud gas and it radiatively cools, causing its temperature to drop sharply. The oxygen ion population does not immediately reach equilibrium, due to NEI effects. Instead, there is a temporal delay before the ionization and recombination rates approach their expected values. This process results in a significant amount of O VI that was produced through recombination from O VII, but has not yet recombined to O V. This explains why there is an overabundance of O VI in low temperature cells as seen in our simulations.

Narrow line widths have also been detected in observations toward HVC, CGM and IGM gas (Tripp et al., 2008a; Qu et al., 2024; Savage et al., 2014). A detailed analysis of b values in the low-redshift intergalactic medium was conducted by Tripp et al. (2008a), whose results revealed a broad overall range of b values from \sim 4 to over 100 km s⁻¹. Their study distinguished between two populations: intervening absorbers sampling the general IGM and proximate absorbers located near the background QSO. For the 70 robust intervening components, the median value of b(O VI) is 24 km s⁻¹ and the majority of lines

have $b(O~VI) < 70~{\rm km~s^{-1}}$. In contrast, the proximate absorbers were found to be statistically narrower, with a median b(O~VI) of 17 km s⁻¹. For a subset of intervening systems where O VI and H I components were kinematically aligned, Tripp et al. (2008a) performed a detailed analysis comparing the line widths to explicitly calculate the thermal and non-thermal broadening contributions. This analysis revealed two key findings for these aligned absorbers. First, the non-thermal motions are a significant and often dominant component of the line broadening. Second, many components are surprisingly cool, with 62% of them implying temperatures of $T < 10^5~{\rm K}$. These findings led them to investigate the ionization mechanism. They found that purely collisional ionization models, both in and out of equilibrium, could not account for these cool temperatures. Instead, they proposed that the O VI in these systems is likely produced by photoionization from the extragalactic UV background, potentially in combination with some collisional ionization in hybrid models.

Sembach et al. (2003b), who focused on O VI absorption features in Galactic high velocity gas, reported 2 sight lines with b values smaller than $b_{\rm CIE}$, although one of these is questionable. Sembach et al. (2003b) also mentioned that FUSE has an instrumental broadening of \sim 12 to \sim 15 km s⁻¹. This tends to make observed line widths greater than actual line widths. Qu et al. (2024) used the Hubble Space Telescope Cosmic Origins Spectrograph to survey the warm-hot CGM around galaxies and galaxy groups. They determined the O VI velocity dispersion ($\sigma_{O\ VI}$), where $b_{O\ VI} = \sqrt{2}\ \sigma_{O\ VI}$, for their observations. They identified 2 sight lines with $\sigma_{O\ VI}$ values that were smaller than that at the O VI CIE temperature (\sim 12.3 km s⁻¹). These studies mentioned that the observed broadening is a combination of both the thermal and non-thermal effects, but they did not explicitly calculate the non-thermal part.

Savage et al. (2014) analyzed O VI and H I absorption features from observations of IGM and CGM gas. Their results revealed a broad range of b(O VI) values, spanning from \sim 5 to \sim 79 km s⁻¹, which is approaching the range derived in our simulations (\sim 6 to \sim 107 km s⁻¹). They figured that these observed line widths (b(O VI)) were due to both a thermal component and a non-thermal component. In order to evaluate the thermal contribution, they determined the temperatures of the O VI, based on a combination of factors including the observed b and the overlap with related H I features. Of the 45 O VI components that have tabulated temperatures or upper limits on temperatures, Savage et al. (2014) found that 40 have

temperatures \leq 10^{5.5} K, the CIE temperature for O VI. Of those, 31 have temperatures \leq 10^{4.8} K (see their Table 4). Although only 7 of their O VI features have $b(O VI) < b_{CIE}$, they found that the majority of their O VI dataset has temperatures which are below T_{CIE} .

By comparing the difference in line widths between O VI and H I, Savage et al. (2014) estimated the temperatures and turbulent velocities of the gas. Based on the deduced temperatures of the gas, Savage et al. (2014) classified the origins of the O VI absorption features as being photoionization, a combination of photoionization and collisonal ionization, or just collisional ionization. They argued that some of the gas may be out of CIE, explaining some O VI in gas whose temperature is below T_{CIE} . The O VI may have yet to recombine to O V and lower ions. They noted that producing substantial column densities of O VI via photoionization from the extragalactic background requires the clouds to have very low densities and very long path lengths.

However, Sembach et al. (2003b) concludes that photoionization is not likely to be the reason for the presence of O VI in the regions that they studied, i.e. HVCs near the Milky Way. The extragalactic background UV radiation is not strong enough to explain the quantity of observed O VI in those HVCs. In addition, their photoionization models would require very low cloud volume densities, and thus very large sizes.

Our simulations reproduce the narrow O VI line widths due to recombination in cooling gas without requiring photoionization. Furthermore, our simulation scenario does not require the cloud density to be extremely low (see Table 3.1).

Table 4 in Savage et al. (2014) also listed the non-thermal contribution to the total b values, which they call b_{NT} . For what they called photoionization absorbers, they got a range from 5 to 55 km s⁻¹. For what they called collisional ionization absorbers, they got a range from <10 to 56 km s⁻¹. Tripp et al. (2008a) used the same method to calculate the thermal broadening and non-thermal broadening, b_{NT} , but their sight lines were observed by different spectrographs. Tripp et al. (2008a)'s full sample yields a non-thermal broadening range of b_{NT} from 6 to 75 km s⁻¹, which is somewhat larger than those found by Savage et al. (2014). However, when the FUSE data are removed, due to its lower spectral resolution, from the Tripp et al. (2008a) dataset, leaving only the STIS data, the b_{NT} range shrinks considerably to 6–30 km s⁻¹. This

range is very different from those of Savage et al. (2014). Comparing with the above O VI observations, our HVC O VI has a larger non-thermal broadening range (from \sim 4 km s⁻¹ to \sim 106 km s⁻¹) showing even more substantial contributions from turbulence.

3.5 Summary

We develop a method to calculate the Doppler broadening parameter b in clouds that were simulated by the FLASH code. In our simulations, cool clouds quickly move through and mix with the hot ambient gas. Our results reveal plentiful amounts of O VI and a wide range of b values. The narrow b values are of particular interest. Here we provide an explanation for them. Radiative cooling rapidly lowers the temperature of the ambient gas once it mixes with the cloud gas. However, due to NEI and mixing effects, the ionization and recombination rates do not immediately reach equilibrium at the new temperature. This temporal delay results in recombination rates from O VII to O VI and from O VI to O V that are lower than those under CIE conditions. Consequently, an overabundance of O VI is observed as it remains in a transitional state, waiting for recombination to O V in relatively cool regions. These processes may explain the narrow line widths observed in various astrophysical environments, such as HVCs, CGM, and IGM.

3.6 Author Contributions

Dr. Robin Shelton helped me develop the basic idea of making simulated absorption spectra. I designed and wrote the codes for fitting, plotting and calculations. I wrote the draft under the supervision of Dr. Shelton.

CHAPTER 4

A STUDY OF C IV AND SI IV IONS

DISTRIBUTED OVER A WIDE

TEMPERATURE RANGE IN HIGH

VELOCITY CLOUDS I

Wang. C, Goetz, E. H., & Shelton, R. L. To be submitted to the Astrophysical Journal. For more details about the completeness of this project, please see Section 4.5

Abstract

We calculate the total amount of material in quickly moving clouds within circumgalactic and intergalactic medium from C IV and Si IV measurements with our previous developed method. We calculate the time-dependent carbon and silicon ionization populations from our simulations of high-velocity clouds (HVCs) modeled by the FLASH hydrodynamic code. Similar to the analysis of O VI, we find that our ratio of C IV/carbon ($f_{\rm CIV}$) and ratio of Si IV/silicon ($f_{\rm SiIV}$) are also much smaller than the values from static gas. This result shows that C VI and Si IV can also exist within a larger temperature range in our dynamic NEI clouds than previously thought. This finding implies that C IV and Si IV can not only trace ionized hydrogen but can also trace neutral hydrogen as well. We use our method to calculate the total hydrogen column density along the observed sight lines toward the Magellanic Stream and its fragments.

4.1 Introduction

High-velocity clouds (HVCs) are important components of the circumgalactic medium (CGM) and halo gas. They move fast through the environmental gas with a velocity of $|v_{LSR}| \ge 90 \text{ km s}^{-1}$ (Wakker & van Woerden, 1997) or 100 km s⁻¹ (Richter, 2017). These clouds are observed across a wide range of distances, from a few kiloparsecs to tens of kiloparsecs from the Galactic plane, and can be predominantly neutral (H I) or highly ionized (H II) (Wakker et al., 2007; Mishra et al., 2025). Well-known Galactic HVCs include the Magellanic Stream (MS), a tidal remnant of the Magellanic Clouds (Nidever et al., 2010), and Smith's Cloud, a comet-shaped HVC with a known trajectory intersecting the Galactic disk (Fox et al., 2016). Another prominent example is Complex C, which shows evidence of interaction with the Galactic halo (Wakker et al., 2007).

Observations of HVCs often reveal highly ionized species such as O VI, C IV and Si IV, indicating the presence of warm-hot, collisionally ionized gas due to the mixing. These ions are important for understanding the physical conditions and ionization states within HVCs (Fox et al., 2005b; Sembach et al., 2003b). Their detection in both dense, neutral HVCs and diffuse, highly ionized HVCs suggests a multi-phase nature, where mixing layers between cold clouds and hotter ambient gas (e.g., the Galactic halo and CGM) are prevalent (Richter et al., 2017; Marasco et al., 2022). The ionization state of these ions can be characterized by two primary regimes: collisional ionization equilibrium (CIE) and non-equilibrium ionization (NEI). In CIE, the ionization and recombination rates are balanced, typically found in stable, hot plasmas. However, for dynamic gas like HVCs interacting with the CGM and halo gas, where temperature and density can change rapidly, the gas can be out of CIE and is better described by NEI models, which can calculate the time-dependent ionization population. Tripp (2022) have shown that NEI models perform better than CIE models when comparing the line ratios to the results from the observational data.

Hydrodynamic simulations with adaptive mesh refinement codes and NEI models, like FLASH, have become powerful tools for studying the evolution and ionization states of HVCs. These tools can simulate the processes of turbulent mixing and radiative cooling as HVCs travel through the hot Galactic halo and

CGM (Kwak et al., 2009). These simulations can reproduce the column densities, number densities and ionization fraction of the ions which track the mixing regions (e.g., C IV, Si IV, O VI). The results from these simulations provide insights into the formation and survival of different ionization phases within HVCs, showing that high ions are produced in dynamic environments like turbulent mixing layers (Esquivel et al., 2006).

Building upon these conceptions and simulation tools, we develop a method to calculate the total hydrogen column density in HVCs from observed O VI (Goetz et al., 2024a). In this paper, we apply this method to the measurements of C IV and Si IV. We calculate their ionization fraction from our runs and then use these values to calculate the column density of total hydrogen in the observational sight lines based on the observed column densities of C IV and Si IV. Comparing to Goetz et al. (2024a), we select more sight lines toward Magellanic Stream and its fragments.

4.2 Methods

We use FLASH hydrodynamic code to run our simulations and the version is 4.6.2. We have the same basic settings and initial conditions for cloud and ambient materials as described in Goetz et al. (2024a). Since the toolchains used to build libraries on our High Performance Computing systems on GACRC Sapelo2 have been updated, all of our ten runs ends at 200 Myrs as we desire. The initial parameters are also tabulated in Table 4.1. In addition to oxygen ions, we add carbon and silicon ions in the simulations.

4.3 Results

4.4 Discussion

Our average value of $f_{\rm CIV}$ is smaller than the peak value in static gas by a factor of \sim 2.3 and average value of $f_{\rm SiIV}$ is smaller than the peak value in static gas by a factor of \sim 2.4. Based on these results, our estimated values for total hydrogen column density are also higher than previously thought if we use the observed column density of C IV and Si IV.

Table 4.1: Simulation Parameters
Simulation n(H) . . . T . . n(H) . . . T . .

Simulation	$n(H)_{cloud}$	$T_{ m cloud}$	$n(H)_{ambient}$	$T_{ m ambient}$	$r_{ m cloud}$	$v_{ m inflow}$
	(cm^{-3})	(K)	(cm^{-3})	(K)	(pc)	(km s^{-1})
Run 1	0.4	5000	0.001	2×10^{6}	500	150
Run 2	0.4	5000	0.001	2×10^{6}	500	100
Run 3	0.4	5000	0.001	2×10^{6}	300	150
Run 4	0.4	5000	0.001	2×10^{6}	500	300
Run 5	0.04	5000	0.0001	2×10^{6}	500	150
Run 6	0.2	5000	0.001	1×10^{6}	500	150
Run 7	2.0	1000	0.001	2×10^{6}	500	150
Run 8	I.O	1000	0.001	1×10^{6}	500	150
Run 9	0.67	3000	0.001	2×10^{6}	500	300
Run 10	0.222	9000	0.001	2×10^{6}	500	150

4.5 Author Contributions

I ran all the simulations in this project. I have finished all the figures and most of the core calculations for this project that are presented in this chapter. I anticipate continuing to work on this project under the supervision of Dr. Robin Shelton and submitting the future manuscript to the Astrophysical Journal.

	Table 4.2: $f_{ m CIV}$	
Clouds	Sight lines	$f_{\mathrm{CIV}}^{\mathrm{a}}$
Magellanic	NGC 7469	0.063
Stream	Mrk 335	0.071
	HE 0226-4110	0.071
	HE 0226-4110	0.071
	PG 0953+414	0.071
	PG 0953+414	0.070
	NGC 7714	0.052
	PHL 2525	0.067
	SDSSJ0012-1022	0.066
Magellanic	HE 0027	0.065
Stream	Ton S210	0.065
Fragments	B0120-28	0.063
	Average $f_{ m CIV}{}^{ m d}$	
	$f_{\rm CIV}$ from average H I/C IV $^{\rm e}$	

- ^a The $f_{\rm CIV}$ for each individual sight line is calculated using the H I/C IV of individual sight lines from Sembach et al. (2003a) and Fox et al. (2010a). It is the average of the values obtained from the ten simulations.
- ^b This $f_{\rm CIV}$ is the average value of the $f_{\rm CIV}$ of the nine sight lines in Complex C. It is calculated from the unrounded values.
- ^c This $f_{\rm CIV}$ is the average value of those calculated from the simulations at the epochs when H I/C IV matches the mean value of H I/C IV for the 9 sight lines listed.
- ^d This $f_{\rm CIV}$ is the average value of the $f_{\rm CIV}$ of the three sight lines in the MS. It is calculated from the unrounded values.
- ^e This $f_{\rm CIV}$ is the average value of those calculated from the simulations at the epochs when (H I/C IV) matches the mean value of H I/C IV for the three sight lines listed.

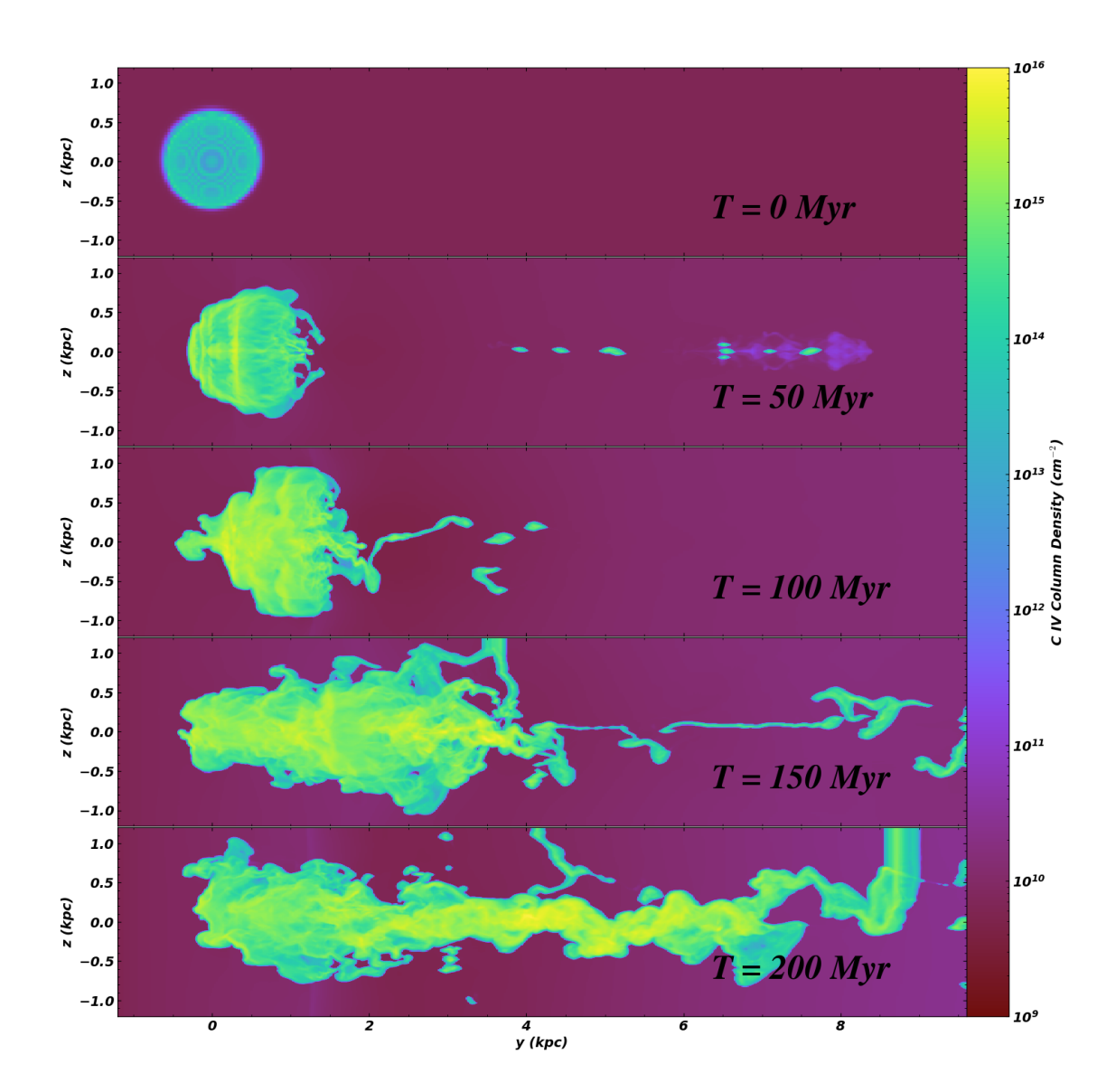


Figure 4.1: C IV column density plots for Run 1 at 5 epochs (0, 50, 100, 150, and 200 Myr). The column densities are calculated by integrating the C IV number density along sight lines directed into the page. These sight lines are in the \hat{y} direction, which is the direction in which only half the cloud was simulated. So, we have multiplied the column densities by 2 to account for having simulated only 1/2 of the cloud. The ambient gas moves to the right, interacting with the cloud gas. The resulting tail formation and hydrodynamic instabilities are apparent in this figure.

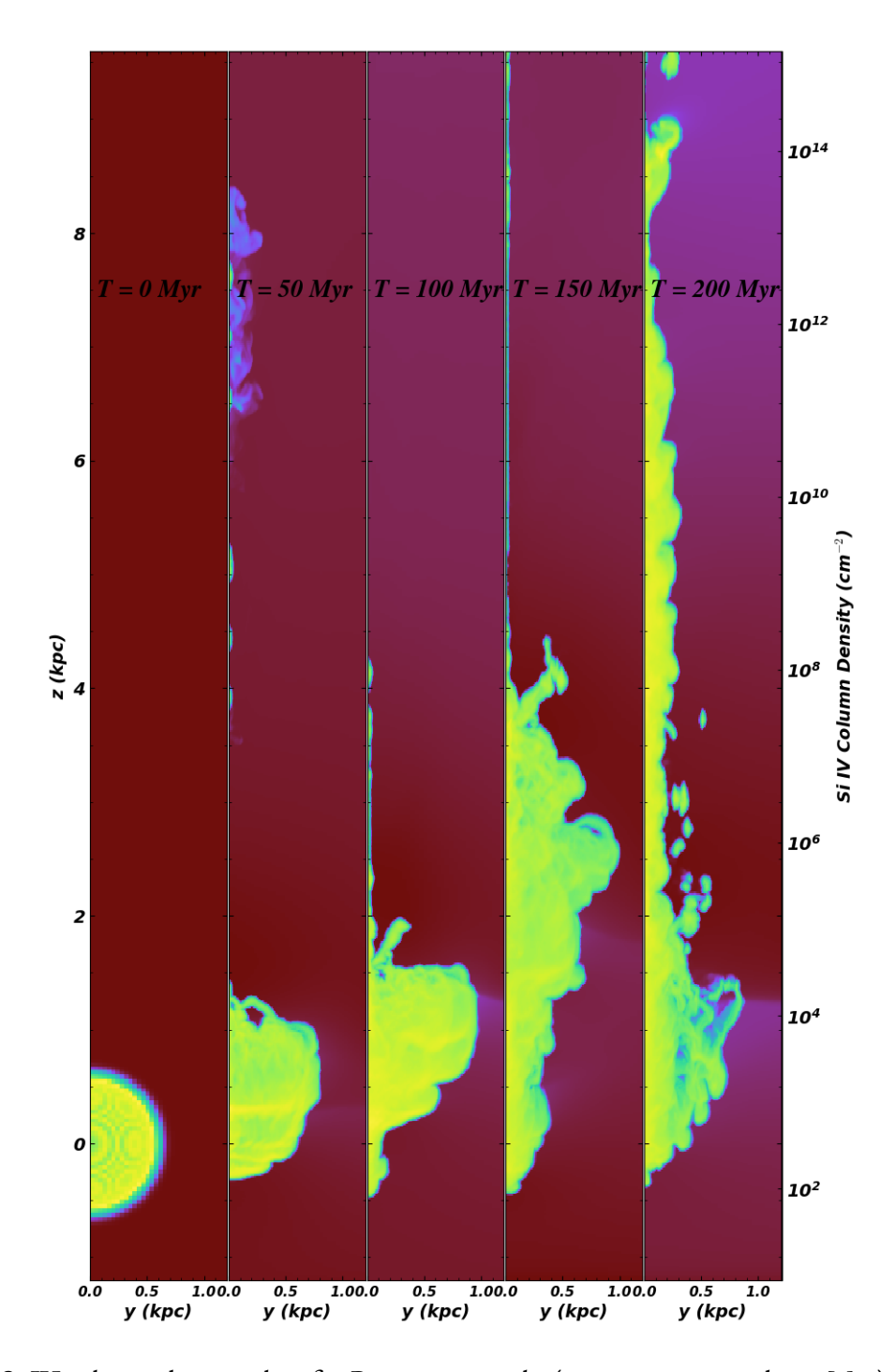


Figure 4.2: Si IV column density plots for Run 1 at 5 epochs (0, 50, 100, 150, and 200 Myr). The column densities are calculated by integrating the Si IV number density along sight lines directed into the page. These sight lines are in the \hat{x} direction. The ambient gas moves to the right, interacting with the cloud gas. The resulting tail formation and hydrodynamic instabilities are apparent in this figure.

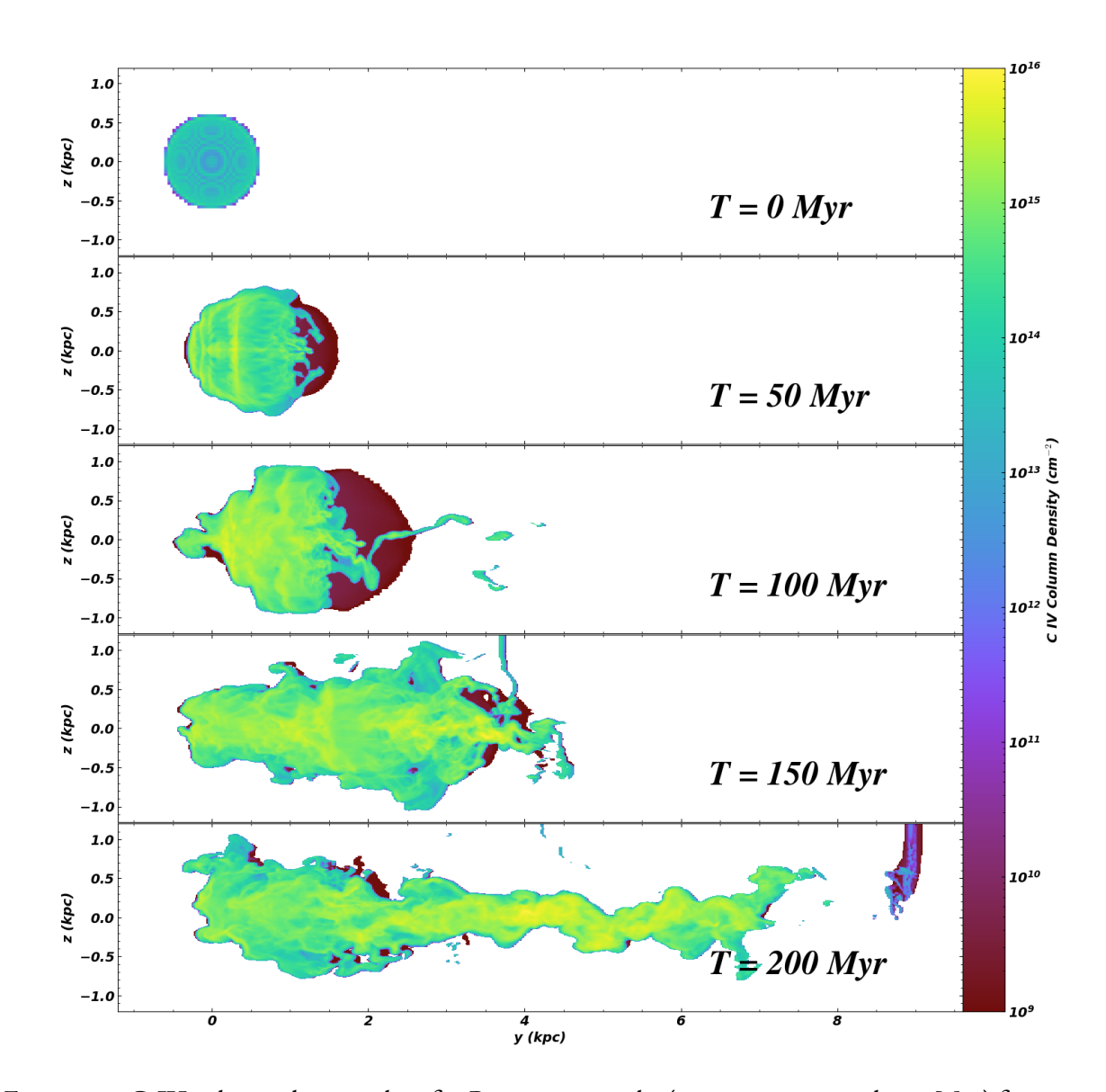


Figure 4.3: C IV column density plots for Run 1 at 5 epochs (0, 50, 100, 150, and 200 Myr) for material whose velocity in the \hat{z} direction differs by more than 100 km s⁻¹ from that of the ambient material. As in Figure 4.1, the column densities include a factor of 2. At late times, part of the cloud's tail has slowed too much to be considered part of the cloud. This can be seen by comparing Figure 4.3 with Figure 4.1.

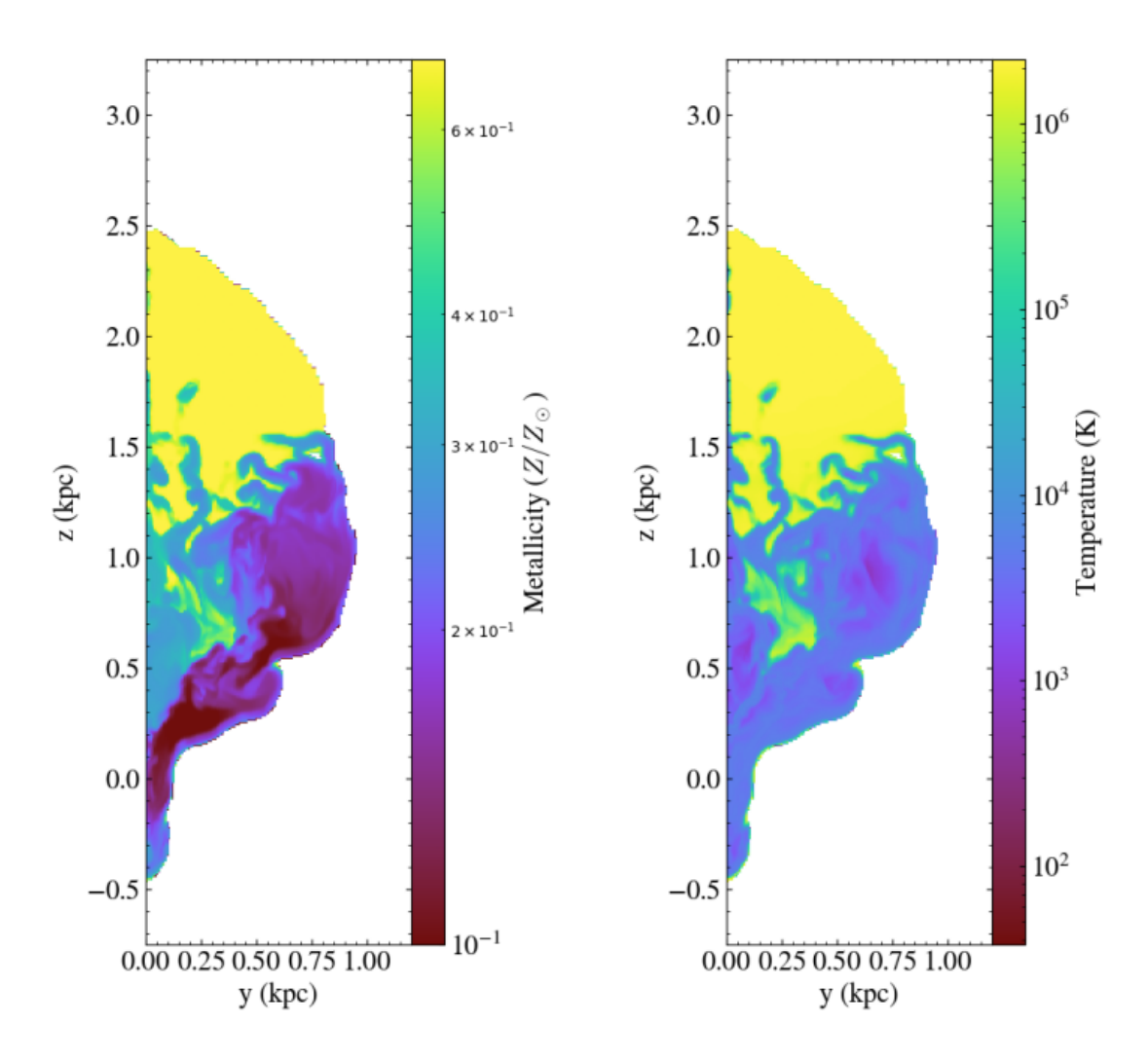


Figure 4.4: Left: Metallicity plot of the cloud in the domain at x=0 kpc. Right: Temperature plot of the cloud in the domain at x=0 kpc.

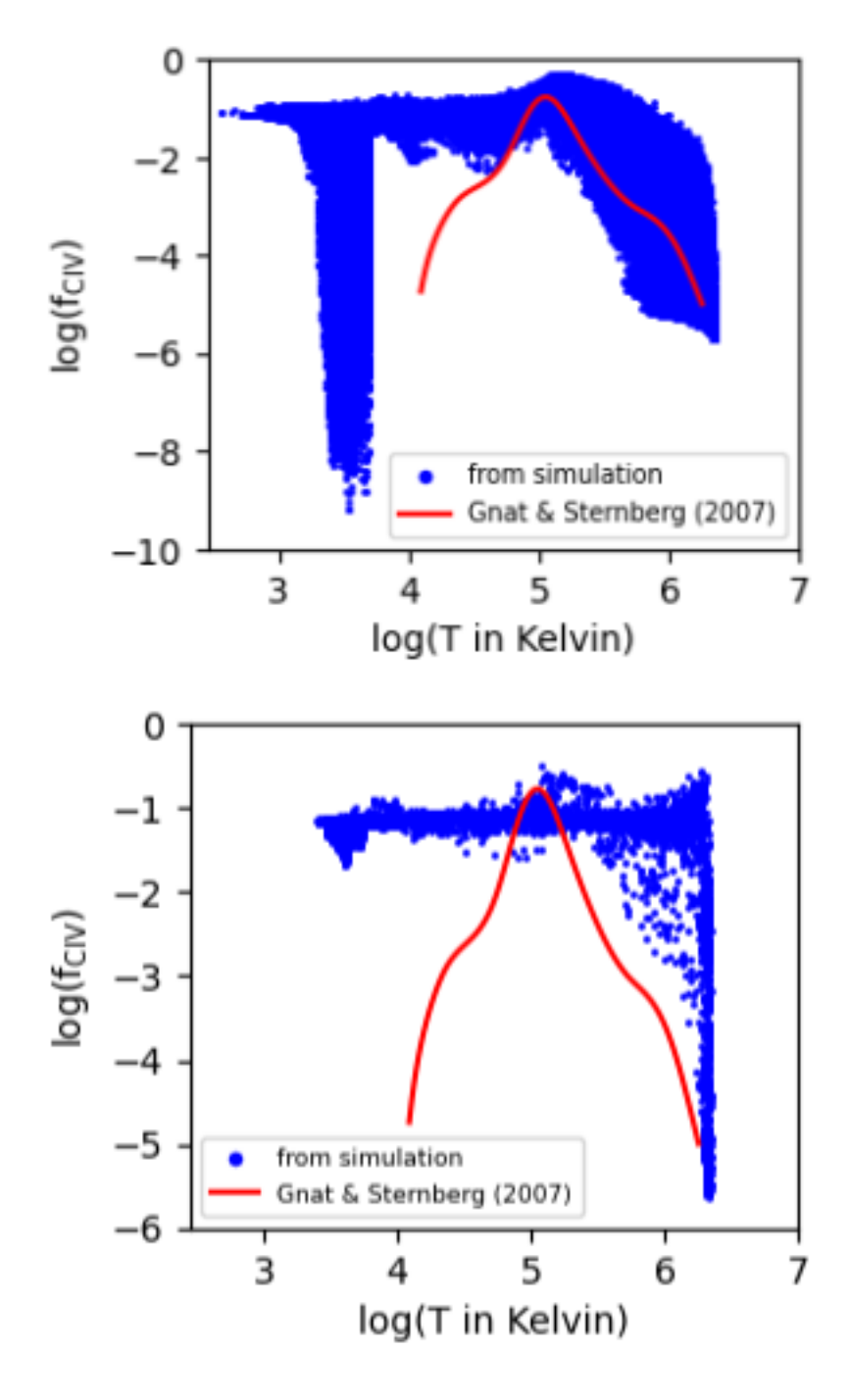


Figure 4.5: Top panel: the $f_{\rm CIV}$ and temperature are plotted with a blue dot for every cell in the cloud. Bottom panel: the $f_{\rm CIV}$ and temperature are plotted with a blue dot for every sight line through the cloud. The sight lines are oriented parallel to the x axis and the temperature is the mass-weighted average temperature along the line of sight. Both plots were made from Run I at 100 Myr. Only the material that met the cloud's velocity criterion was used to make these plots. For comparison, the $f_{\rm CIV}$ vs T curve for static gas is plotted in red. It was adopted from Gnat & Sternberg (2007a). C IV is confined to a narrower range of temperatures in the static curve than in our simulations, which include dynamic mixing of warm and hot gas.

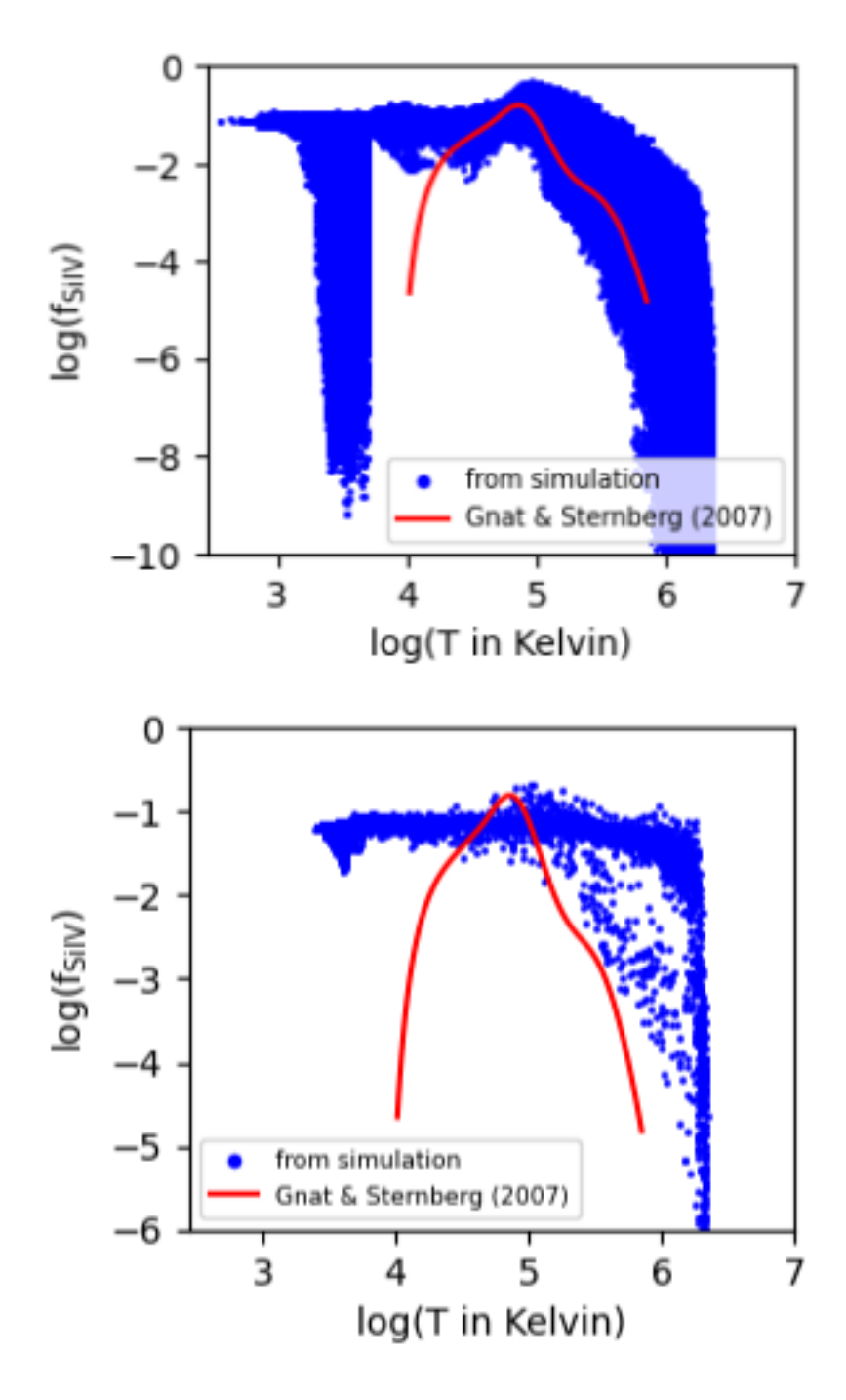


Figure 4.6: Top panel: the $f_{\rm SiIV}$ and temperature are plotted with a blue dot for every cell in the cloud. Bottom panel: the $f_{\rm SiIV}$ and temperature are plotted with a blue dot for every sight line through the cloud. The sight lines are oriented parallel to the x axis and the temperature is the mass-weighted average temperature along the line of sight. Both plots were made from Run 1 at 100 Myr. Only the material that met the cloud's velocity criterion was used to make these plots. For comparison, the $f_{\rm SiIV}$ vs T curve for static gas is plotted in red. It was adopted from Gnat & Sternberg (2007a). Si IV is confined to a narrower range of temperatures in the static curve than in our simulations, which include dynamic mixing of warm and hot gas.

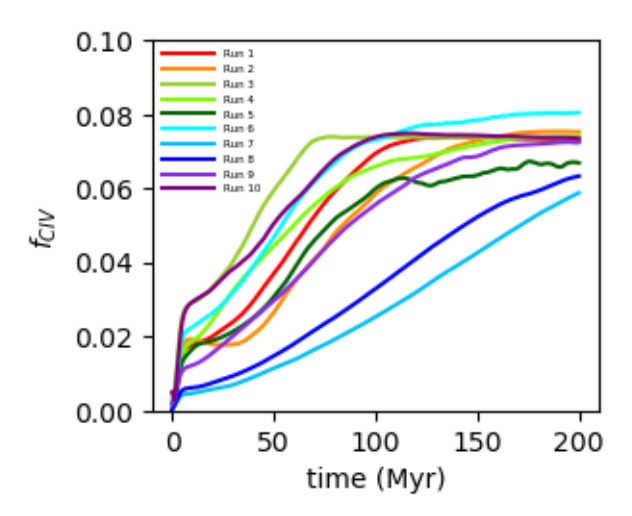


Figure 4.7: Plot of the cloud-averaged $f_{\rm CIV}$ for each simulation as a function of time. Generally, $f_{\rm CIV}$ increases with time as the cloud mixes with the ambient material.

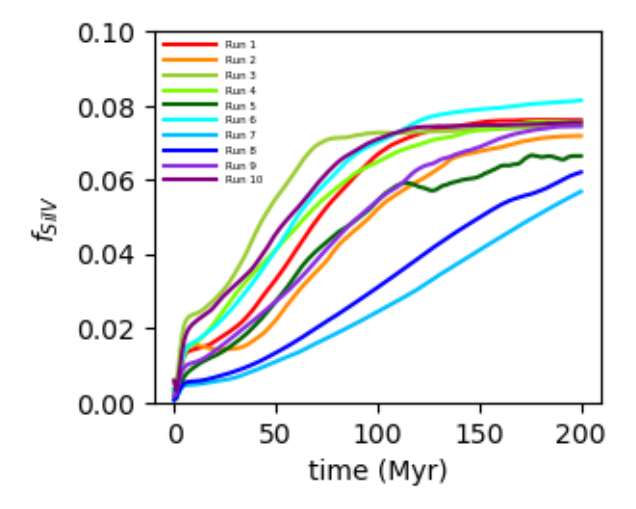


Figure 4.8: Plot of the cloud-averaged $f_{\rm SiIV}$ for each simulation as a function of time. Generally, $f_{\rm SiIV}$ increases with time as the cloud mixes with the ambient material.

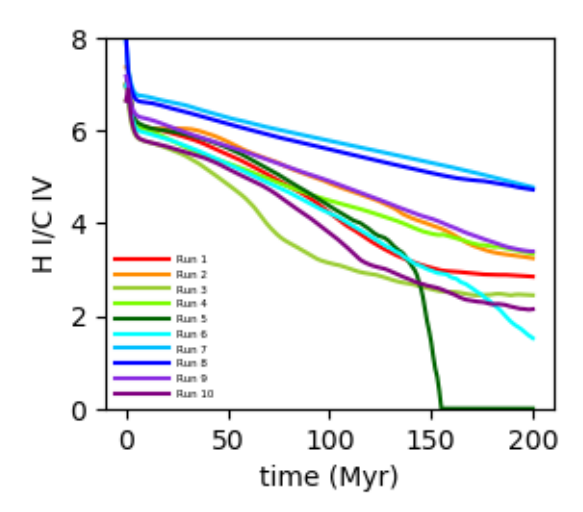


Figure 4.9: Plots of H I/C IV for each simulation as a function of time. Generally, H I/C IV decreases with time as hydrogen is ionized and $f_{\rm CIV}$ increases (see Figure 4.7).

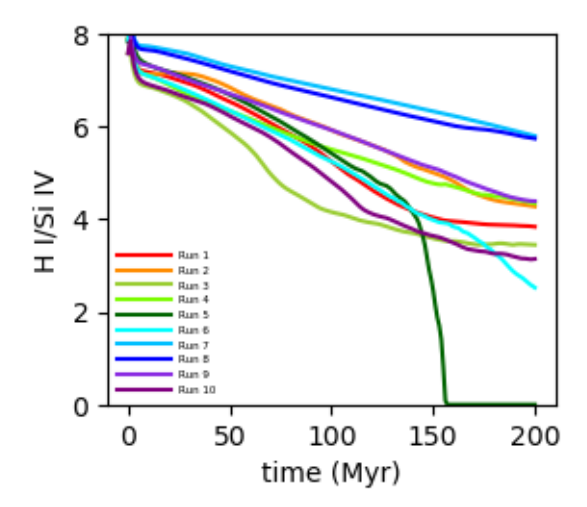


Figure 4.10: Plots of H I/Si IV for each simulation as a function of time. Generally, H I/Si IV decreases with time as hydrogen is ionized and $f_{\rm SiIV}$ increases (see Figure 4.8).

	Table 4.3: $f_{\rm SiIV}$	
Clouds	Sight lines	$f_{ m SiIV}{}^{ m a}$
Magellanic	NGC 7469	0.064
Stream	Mrk 335	0.070
	HE 0226-4110	0.071
	HE 0226-4110	0.070
	PG 0953+414	0.070
	NGC 7714	0.062
	PHL 2525	0.066
	SDSSJ0012-1022	0.067
Magellanic	HE 0027	0.067
Stream	Ton S210	0.065
Fragments	B0120-28	0.064
	Average $f_{ m SiIV}{}^{ m d}$	
	$f_{ m SiIV}$ from average H I/Si IV $^{ m e}$	

- ^a The $f_{\rm SiIV}$ for each individual sight line is calculated using the H I/Si IV of individual sight lines from Sembach et al. (2003a) and Fox et al. (2010a). It is the average of the values obtained from the ten simulations.
- ^b This $f_{\rm SiIV}$ is the average value of the $f_{\rm SiIV}$ of the nine sight lines in Complex C. It is calculated from the unrounded values.
- ^c This $f_{\rm SiIV}$ is the average value of those calculated from the simulations at the epochs when H I/Si IV matches the mean value of H I/Si IV for the 9 sight lines listed.
- ^d This $f_{\rm SiIV}$ is the average value of the $f_{\rm SiIV}$ of the three sight lines in the MS. It is calculated from the unrounded values.
- $^{\rm e}$ This $f_{\rm SiIV}$ is the average value of those calculated from the simulations at the epochs when (H I/Si IV) matches the mean value of H I/Si IV for the three sight lines listed.

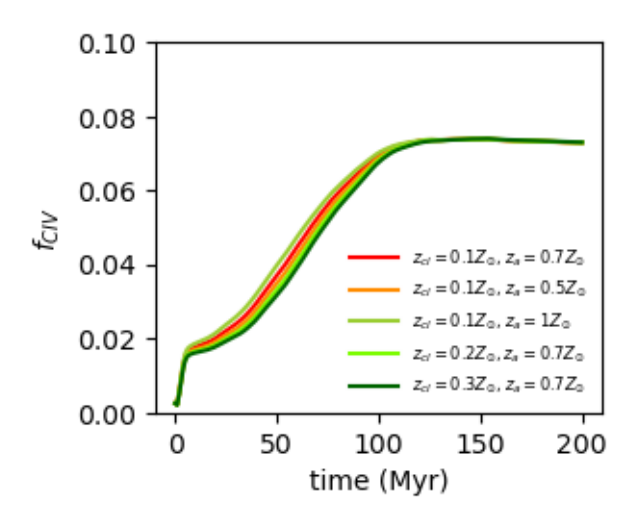


Figure 4.11: Plot of $f_{\rm CIV}$ for Run 1 for a variety of cloud and ambient metallicities. Changing the ambient metallicity has little effect on the curve. Changing the cloud metallicity has a more noticeable but still insignificant effect.

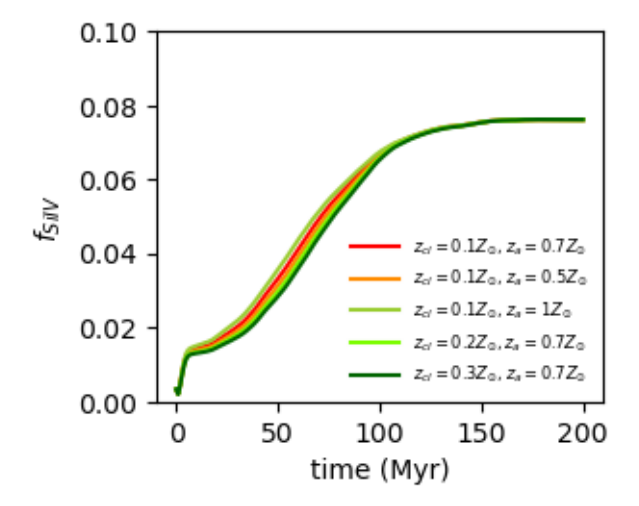


Figure 4.12: Plot of $f_{\rm SiIV}$ for Run 1 for a variety of cloud and ambient metallicities. Changing the ambient metallicity has little effect on the curve. Changing the cloud metallicity has a more noticeable but still insignificant effect.

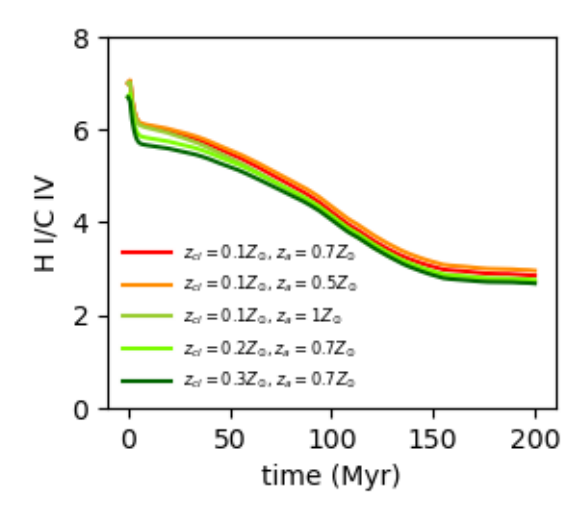


Figure 4.13: Plots of H I/C IV for Run 1 for a variety of cloud and ambient metallicities. As for $f_{\rm CIV}$, changing the ambient metallicity has little effect on the curve. Changing the cloud metallicity has a more noticeable, but still small effect.

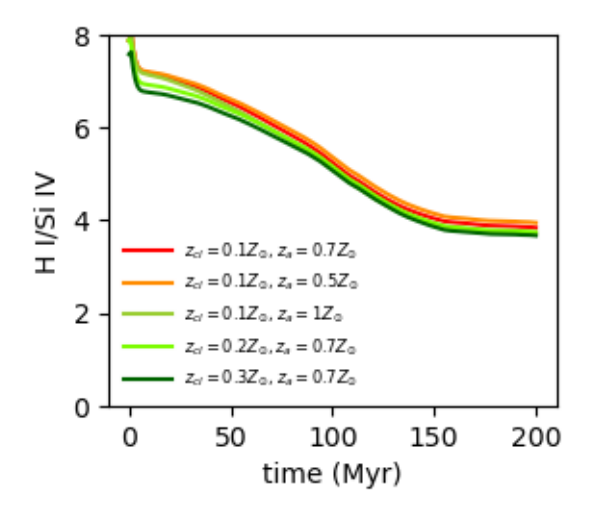


Figure 4.14: Plots of H I/Si IV for Run 1 for a variety of cloud and ambient metallicities. As for $f_{\rm SiIV}$, changing the ambient metallicity has little effect on the curve. Changing the cloud metallicity has a more noticeable, but still small effect.

CHAPTER 5

THE O VI EMISSION FROM THE EXTENDED DISK OF NGC 1068 ¹

¹Shelton, R. L & Wang, C., 2025, to be submitted to the Astrophysical Journal.

Abstract

We report null detections of emission from interstellar O VI in the disk and halo of the well known starburst and Seyfert galaxy NGC 1068, also known as M86, and from the Milky Way. The observations used long FUSE exposures, during which the low resolution aperture was pointed toward NGC 1068's extended disk, \sim 8.32 kpc from that galaxy's AGN and a similar distance from its starburst regions. We found no O VI emission from NGC 1068, which is surprising. The 1σ upper limits on the O VI doublet ($\lambda\lambda$ 1032, 1038) are 154 ± 328 and 7 ± 292 photons s⁻¹ cm⁻² sr⁻¹, respectively. The observation also placed very tight upper limits (-44 ± 307 , and -66 ± 283 photons s⁻¹ cm⁻² sr⁻¹) on the O VI intensity of the Milky Way's halo. This line of sight is the dimmest yet examined with a long FUSE observation. This and other measurements indicate that the Milky Way halo's O VI is distributed very inhomogeneously and that the O VI nearer to the disk is denser and more emissive, while the O VI at greater heights is much more plentiful. We derived a value of $4.6^{+18}_{-4.6} \times 10^{-4}$ cm⁻³ for the average electron density of the O VI-bearing gas, and a value of $9.3^{+37}_{-9.3} \times 10^{-4}$ cm⁻³ if the gas is beyond the extincting material.

5.1 Introduction

Starburst galaxies, as a class, exhibit vigorous star formation. It is commonly thought that they have much higher star formation rates per gas surface density than typical disk galaxies (Kennicutt, 1998; Daddi et al., 2010), or alternatively, especially plentiful supplies of star-forming gas (Scoville et al., 2016).

Starburst activity tends to be strongly correlated with galactic mergers and tidal interactions (Kennicutt, 1998). Mergers trigger the infall of gas, which instigate bursts of star formation. This phenomenon was extensively explored by Di Matteo et al. (2005), Springel et al. (2005). See also Scoville et al. (2016).

The prolific creation of new stars quickly results in greater stellar wind activity and numerous supernova explosions. They heat substantial quantities of gas (Strickland et al., 2004) and drive strong outflows, referred to as feedback and superwinds (Heckman et al., 1990; Lehnert & Heckman, 1996; Hoopes et al., 2003). Starbursts also redistribute gas within galaxies, thus profoundly influencing the evolution of both the stellar population and the galaxies themselves. The resulting outflows can thermally, chemically (Heckman et al., 1990; Hoopes et al., 2003; Grimes et al., 2009; Heckman et al., 2017) and magnetically (Lopez-Rodriguez et al., 2021) modify the circumgalactic medium.

Starburst galaxies are prolific emitters of X-rays (Grimes et al., 2005) and UV photons (Meurer et al., 1997) For instance, in the well-studied starburst galaxy M82, the observed X-ray luminosity is 4×10^{40} erg s⁻¹ and the estimated intrinsic luminosity is 4 times that value. The accompanying hot gas has temperatures reaching 10^7 K (Moran & Lehnert, 1997; Lehnert et al., 1999). Some compact starburst galaxies have UV surface brightnesses of $\sim 10^9$ L $_{\odot}$ kpc⁻² (Hoopes et al., 2007).

A common tracer of hot gas, O VI, is more prevalent in starburst galaxies. Grimes et al. (2009) measured an average O VI column density of $\sim 10^{15}$ cm $^{-2}$ in their sample of 16 low redshift starburst galaxies, which is \sim 4.2 times greater than the average O VI column density on high latitude Milky Way sight lines in the Savage et al. (2003) survey, which is $\sim 2.4 \times 10^{14}$ cm $^{-2}$. In addition, the (Tumlinson et al., 2011) analysis of COS HST survey data shows that more O VI is detected in galaxies with star-forming activity than in galaxies with less or no star-forming activity.

O VI can exist both in and above the disks of galaxies (Heckman et al., 2002a). For starburst galaxies, the distribution of O VI ions varies, depending on the properties of the galaxies, but is typically associated with regions of great star-formation activity and the resulting outflowing superwinds (Hoopes et al., 2003; Grimes et al., 2006). On top of that, feedback inflow from the circumgalactic medium (CGM) should also contain O VI (Bordoloi et al., 2017).

Most observations of starburst-driven superwinds are limited to within 10 kpc of the main body of the galaxy Heckman et al. (2017). In this paper, we search for O VI photons originating at roughly 8.32 kpc from the center of one of the brightest and most well-studied starburst galaxies, NGC 1068, also known as M77. The results are relevant to studies of the transport of hot gas in starburst galaxies. Considering that NGC 1068 also has a bright AGN, it is also important to know whether the AGN hot gas has a big effect on this region.

This paper uses data from the Far Ultraviolet Spectroscopic Explorer (FUSE). FUSE made several observations of NGC 1068 (Zheng et al., 2008, 2009). During most of the observations, FUSE's high resolution aperture (HIRS) was pointed toward the center of NGC 1068 (Zheng et al., 2008, 2009) and FUSE's low resolution aperture (LWRS) was pointed several kpc from the center. Owing to NGC 1068's $\sim 25^{\circ}$ tilt, the off-center sight line went through both the disk and the halo of NGC 1068. In this paper, we analyze this LWRS data.

The O VI ion's strongest transitions are the doublet at 1031.93 Å (${}^2S_{\frac{1}{2}}$ - ${}^2P_{\frac{3}{2}}^0$) and 1037.62 Å (${}^2S_{\frac{1}{2}}$ - ${}^2P_{\frac{1}{2}}^0$) (Kaufman & Martin, 1989). The atomic physics factor for the 1032 Å transition is twice that of the 1038 Å transition. This favors 1032 Å emission by a factor of 2, unless there is so much O VI that there is self screening (Shelton et al., 2001). Here we report tight 2 σ upper limits on the intensity of the O VI ${}^2S_{\frac{1}{2}}$ - ${}^2P_{\frac{3}{2}}^0$ and ${}^2S_{\frac{1}{2}}$ - ${}^2P_{\frac{1}{2}}^0$ emission lines seen through FUSE's LWRS aperture at the redshift of NGC 1068, z=0.0038, with a velocity of 1.14 \times 10 3 km s $^{-1}$.

They are 7 ± 584 and 154 ± 656 LU, respectively. These values are noticeably dim compared with those of off-center regions of other starburst galaxies.

NGC 1068 is well separated in velocity from the Milky Way (MW), enabling FUSE to simultaneously record O VI emission from the Galactic halo along the line of sight to $(\ell, b) = (172.15^{\circ}, -51.93^{\circ})$.

We measure the intensity, finding 2 σ upper limits on the 1032 Å and 1038 Å emission of 168 \pm 586 and -66 \pm 566 LU, respectively. These values are much less than typical high latitude O VI intensities, but the O VI column density observed toward NGC 1068's center, only \sim 107.8 arcsec away, is about 0.4 of the average found on high latitude sight lines (Savage et al., 2003).

These results can be understood as the consequence of a highly inhomogeneous distribution of O VI in the galactic halo, in which the thermal pressure, and therefore the emissivity per ion, decreases with height. On the typical line of sight, gas in the lower halo contributes most of the O VI photons, while gas at greater heights contributes most of the O VI ions. What is special about the NGC 1068 sight line is that it passes through a hole in the lower halo's patchy O VI distribution and so demonstrates that the lower halo's O VI distribution is patchy enough for such holes to exist.

5.2 Observation

FUSE observed NGC 1068 for two observing programs, PIII and AI39. The PIII observing program required the 900 arcsec² LWRS to be pointed toward the AGN in the center of NGC 1068. Zheng et al. (2008) used these data to measure the AGN's O VI brightness. The 25 arcsec² HIRS aperture was pointed ~107.8 arcsec away, toward NGC 1068's disk. However, because of that aperture's small size, the HIRS data did not yield enough photons to be useful in measuring the brightness of the disk.

The A139 observations required the HIRS aperture to be pointed toward NGC 1068's AGN. Zheng et al. (2008) incorporated these data into their analysis of the AGN and Wakker et al. (2003) and Savage et al. (2003) used the AGN's emission as a distant light source for their measurement of the Milky Way's O VI column density. The LWRS aperture was pointed toward NGC 1068's disk, ~107.8 arcsec away. Dixon et al. (2006) analyzed the LWRS data to calculate the intensity of O VI at the MW's redshift. But until now these data have not been used to analyze the intensity of O VI at the redshift of NGC 1068, and this is the first time to analyze the O VI intensity from NGC 1068. Here, we use the low resolution aperture data to measure the intensities of O VI resonance line photons (1032, 1038 Å) and those of other ions at the redshifts corresponding to NGC 1068 and the Milky Way.

FUSE's program ID139 data were taken between November 29, 2001 and December 1, 2001. The FUSE data were taken in five sessions that were archived under program identification numbers A1390201, A1390202, A1390203, A139204, and A139205. Detector 1 recorded photons for a total of 97 ksec, of which 77 ksec were during the night phase of the satellite's orbit. Detector 2 was de-powered for about 20% of this time, and so recorded photons for only 78 ksec in total, of which 61 ksec occurred during the night phase of the orbit.

The headers of the FUSE A139 data files list the RA and dec (i.e., RA=02:42:40.501, Dec=-00:00:51.70) of the target aperture chosen by the original observer. Since the HIRS aperture was the target aperture, we will refer to these coordinates as RA_{HIRS} and dec_{HIRS} .

The pointing direction of the LWRS aperture is displaced and rotated relative to that of the HIRS aperture. According to the FUSE Archival Instrument Handbook (Kaiser et al., 2009), the angular separation between the HIRS and the LWRS aperture is $\Delta\theta=107.8''$. Also according to the handbook, the instrument was rotated east of north by the roll angle, which is equal to 270° — APER_PA. The FUSE data files list APER_PA as 129° . Thus, for these observations, the roll angle is 141° . Following the technique in the handbook, the HIRS-to-LWRS axis is oriented counter-clockwise of east by the angle 180° — roll angle, thus 39° .

The coordinates of the LWRS aperture's pointing direction, which we will call RA_{LWRS} and dec_{LWRS} , can be found trigonometrically from:

$$RA_{LWRS} = RA_{HIRS} + \Delta\theta \cos(dec_{HIRS})\cos(39^{\circ})$$

$$Dec_{LWRS} = Dec_{HIRS} - \Delta\theta \sin(39^{\circ}).$$

These equations yield RA_{LWRS} = 02:42:46.09 and Dec_{LWRS} = -00:01:59.54.

Figure 5.1 shows the LWRS pointing direction overlayed on an image of NGC 1068. For a distance to NGC 1068 of 14.4 Mpc (Tully, 1988; Bland-Hawthorn et al., 1997), an angular separation between the LWRS pointing direction and NGC 1068's center of 107.8" (Kaiser et al., 2009) correlates to 7.54 kpc on the plane of the sky. Given NGC 1068's $\sim 25^{\circ}$ tilt, the line of sight intersects the disk at a location of 8.32 kpc from that galaxy's center.

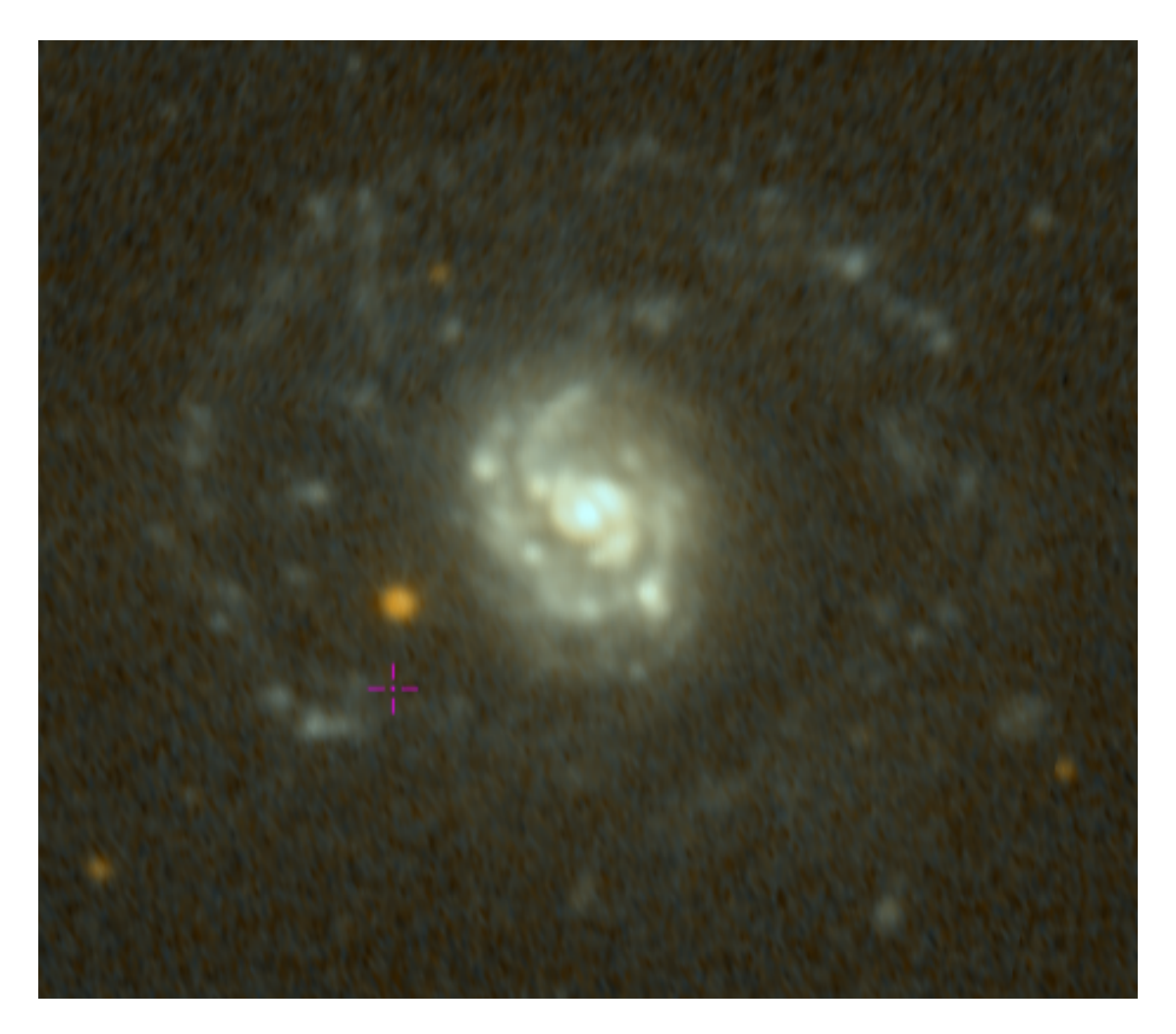


Figure 5.1: Optical image of NGC 1068 from GALEX. The purple cross marks the center location of the FUSE LWRS aperture.

5.3 Results

NGC 1068 is a barred spiral galaxy located approximately 14.4 Mpc from Earth (Tully, 1988; Bland-Hawthorn et al., 1997). It has one of the brightest AGN observed (Ogle et al., 2003; Müller Sánchez et al., 2009). It has a 1 kpc long radio jet and lobe that emanates from the nucleus (Wilson & Ulvestad, 1987). A ring of massive, star-forming clouds and young stars surrounds the nucleus at a radius of \sim 1 kpc (Bruhweiler et al., 1991; Rico-Villas et al., 2021; Sánchez-García et al., 2022). In addition to this starburst

ring, there are additional starburst knots 2.5 kpc to the NE and SW from the center (Bruhweiler et al., 1991).

NGC 1068 has been well observed in multiple wavebands. ROSAT and Chandra observed its X-ray emission (Wilson et al., 1992; Young et al., 2001; Evans et al., 2010). The brightest emission is from the AGN in the center of the galaxy. The X-ray surface brightness decreases with radius out to roughly 1 kpc, where the starburst ring is located (Wilson et al., 1992; Young et al., 2001). In addition, there are less bright asymmetric regions that extend approximately 6.6 kpc in the plane of the sky along a NE-SW axis and form an elliptical shape (Wilson et al., 1992; Young et al., 2001). The ultimate source of this emission is thought to be starburst activity. Neither the bright center nor the extended ellipse overlaps with the FUSE observations presented in this paper, as the pointing direction of the LWRS aperture was approximately 7.54 kpc SE of the nucleus in the plane of the sky and away from the NE-SW aligned ellipse.

Previous studies have found strong O VI doublet emission within the nuclear region of NGC 1068, which they attributed to the bright AGN (Zheng et al., 2009). Observations also show that NGC 1068 has strong starburst activity in its inner disk. In order to determine how widely distributed the hot gas due to the AGN and starbursting activity is, off center regions must be examined for the presence of O VI. Here we find that the O VI intensity emitted by gas 7.54 kpc SE of the nucleus on the plane of the sky is remarkably low. This measurement implies that the AGN and starburst activity have only negligible effects on the rest of the disk and the halo above it.

Here, we compare NGC 1068's O VI intensity with those of several other galaxies for which there are FUSE and/or HST observations: four starburst galaxies (NGC 1705, M82, Haro 11, and SDSS J115630.63+500822.1), the extraplanar plumes of two star forming galaxies (NGC 891 and NGC 4631, which may be a starburst galaxy).

Starburst galaxies NGC 1705 and M82 have large upper limits on their O VI intensities. For NGC 1705, an irregular dwarf starburst galaxy, located 5.1 Mpc (Tosi et al., 2001) to 6.0 Mpc (Tully, 1988) away, Heckman et al. (2001) reported an extinction corrected O VI 1032 Å intensity upper limit of 2.5×10^4 photons⁻¹ s⁻¹ cm⁻² sr⁻¹, assuming 0.3 mag of extinction. The exposure time of their FUSE observation was 21.3 ks and about 95% of it was during the orbital night. M82, a starburst galaxy with a prominent

superwind (Yoshida et al., 2011), is located 3.5 Mpc (Karachentsev et al., 2004; Vacca et al., 2015) to 3.9 Mpc (Sakai & Madore, 1999) away, but possibly as far as 5 Mpc Tully (1988) away. FUSE observed four regions of the superwind above M82's optical disk using the LWRS aperture. Hoopes et al. (2003) reported a 3σ upper limit extinction corrected O VI 1032 Å flux for each pointing. Converting their values into intensities by dividing by the LWRS solid angle yields a range of upper limits from 1.52×10^5 LU to 1.87×10^5 LU. The looseness of these constraints on the intensity are due to the relatively short exposure times of \sim 8 to \sim 12 ks.

Haro II and JII5630.63+500822.1 fit entirely within the FUSE and HST apertures, respectively. Haro II is a blue compact starburst galaxy located \sim 87 Mpc from Earth (Bergvall et al., 2006; Engelbracht et al., 2008). At such a great distance, the entire galaxy fits within the FUSE LWRS aperture. Grimes et al. (2007) reported O VI intensities from the coronal gas of I_{1032} =5.65±1.96×10⁴ LU and I_{1038} =3.44±1.23×10⁴ LU. The exposure time of the LiF IA channel was \sim 15 ks, of which \sim 12 ks was during the satellite-night time.

SDSS JII5630.63+500822.1, is a starburst galaxy, located 1200 Mpc away, with z=0.235 Hayes et al. (2016). With an angular size of 2", the entire galaxy fits within HST's field of view. The observation is carried by ASC, WFC3 and COS together, which have multiple pixels to do mapping. Hayes et al. (2016) spatially resolved and mapped the O VI doublet emission. The O VI emitting regions extend extensively into the halo, reaching radii of 23 kpc. Hayes et al. (2016) reported a O VI 1038 Å luminosity of $20.5^{+1.8}_{-1.2} \times 10^{40}$ erg s⁻¹ and a central O VI surface brightness of $5.3^{+1.2}_{-1.1} \times 10^{-17}$ erg s⁻¹ cm⁻² arcsec⁻², which, after the unit conversion to an intensity, rounds to $1.2^{+0.27}_{-0.24} \times 10^5$ LU They fit the surface brightness measurement with an exponential profile of scale length 7.5 kpc. Such an exponential decay implies that at a distance of d=8.4 kpc the surface brightness would be $3.8^{+0.87}_{-0.79} \times 10^4$ LU. To be consistent with measurements in other observation, we estimate the value of I_{1032} based on the ratio $\frac{I_{1032}}{I_{1038}} \approx 2$.

FUSE also observed two well studied edge-on galaxies that have bright plumes above their disks, NGC 891 and NGC 4631. NGC 4631, also known as the Whale Galaxy, is an edge-on spiral galaxy, with X-ray bright plumes above its disk (Chung et al., 2021) and some obvious star formation regions (Guo et al., 2023). It is 6.9 Mpc (Tully, 1988) to 7.6 Mpc from Earth (Seth et al., 2005). In this case, the FUSE LWRS

observed five fields positioned between 1.6 and 4.9 kpc above the galactic disk. Both research groups confirm the presence of O VI emission, with O VI 1032 Å intensities ranging from 2900 ± 1000 LU to 8600 ± 1800 LU. The range of the exposure times of the five fields is about 9 to 30 ks and at least 60% of the observation time is during the night time. NGC 891 is an edge-on spiral galaxy with an X-ray bright plume of hot gas above its disk (Hodges-Kluck et al., 2018). Although it has obvious star formation regions (Hodges-Kluck et al., 2018), there is some controversy about whether NGC 891 is a starburst galaxy (Yoon et al., 2021). Considering that NGC 891 is located at a distance of 9.1 Mpc (Radburn-Smith et al., 2011) to 10.8 Mpc (Tully et al., 2009), the three fields observed by the FUSE LWRS lie approximately 1.5 to 2.1 kpc above the galactic disk and are toward to a soft X-rays bubble. Otte et al. (2003) did not detect O VI 1032 Å emission to a level greater than 3 σ . in any of these fields, but Chung et al. (2021) expanded upon that work by incorporating additional unexamined fields and employing an updated methodology. With their new analysis, they found O VI emission in one of the fields and measured an intensity in the O VI 1032 Å line of I_{1032} =2300 \pm 700 LU, while the other two fields still have a 3 σ upper limit with a tightest value of 2200 LU. The range of the exposure times for the three fields is \sim 18 to \sim 32 ks. At least 85% of the observation time is during the night time.

Table 5.1 summarizes the O VI observations of these star-forming galaxies. Table 5.2 lists the pointing directions, the angular separations and distances (d) between the galactic centers and the pointing directions, and the distances (z) between the disks and the pointing directions for the aforementioned observations. The apertures toward the Haro II, NGC 1705 and JII5630.63+500822.1 overlap or cover the galactic disks, so the angular separation cannot be determined and thus their information is not tabulated here.

Compared with these results, our derived values of the O VI doublet emission are extremely small. This is an interesting results considering that the observed location is not very far from the AGN and the starburst regions.

The upper limit on the intensity of NGC 1068's disk 7.54 kpc from that galaxy's center is dimmer than the companion observations of other starburst galaxies. These are 4 regions in the extraplanar wind of M82, for which there is an upper limit of $\sim 2 \times 10^5$ LU for the 1032 Å line, majority part of the galactic

disk of NGC 1705, for which there is an upper limit of 2.5 \times 10⁴ LU, all of Haro 11, for which there is a measurement of 5.65 \pm 1.96 \times 10⁴, and all of J115630.63+500822, for which there is a measurement of $3.8^{+0.87}_{-0.79} \times 10^4$. We also compared with the bright plumes of gas above NGC 891 and NGC 4631, whose range of intensities are < 2700 and from 2900 \pm 1000 to 8600 \pm 1800, respectively.

5.4 Discussion

The NGC 1068 sight line passes through two interesting regions, NGC1068's extended disk and the Milky Way's patchy halo. Owing to the long FUSE exposure time, we are able to place very tight upper limits on the O VI 1032 and 1038 Å emission intensities produced in both regions.

Our upper limits for NGC 1068's extended disk are less than the detections and upper limits found for comparison star-forming and starburst galaxies (i.e. NGC 1705, M82, Haro II and SDS JII5630.63+500822.1) and less than the bright plumes above the disks of star-forming galaxy NGC 891 and actively star-forming NGC 4631. It is also dimmer than the typical Milky Way halo intensity seen from the Earth's location. The sight line is 107.8" from the center of NGC 1068. Given NGC 1068's distance of 14.4 Mpc. This is 7.54 kpc beyond the starburst regions. Compensating for the disk's tilt, the sight line intersects the disk 8.32 kpc from the galactic center and passes through extraplanar regions on either side of the disk at somewhat lesser and greater distances from the galactic center. As NGC 1068 is both a starburst galaxy and a Seyfert galaxy, these observations place limits on the influences of the AGN and starburst activity. The AGN's and starburst's hot gas do not successfully circulate to the outer disk or the halo above it. If they circulate, they do not remain hot during the process. Likewise, the disturbances that instigated the AGN and starburst activities do not extend to the outer disk, or the halo above it, with enough power to produce hot gas.

5.5 Author Contributions

Dr. Robin Shelton did all of the measurements of O VI emission intensity and wrote the first version of the draft. I did the literature review for starburst galaxies, especially for NGC 1068. I also made the

literature search for O VI emission in other starburst galaxies, converted the units of the intensity into line unit, and calculated the position of FUSE LWRS aperture. All co-authors agree that the work can be included in this dissertation.

Table 5.1: O VI emission

Target Name	$I_{OVI,1032}^{a}$ (photon s ⁻¹ cm ⁻² sr ⁻¹)	Instrument
NGC 4631 ^b	(photon's cm si)	
NGC 4631 Field A	6000 ± 1200	FUSE LWRS
NGC 4631 Field B	8300 ± 1300	FUSE LWRS
NGC 4631 Field F	2900 ± 1000	FUSE LWRS
NGC 4631 Field H	4700 \pm 1000	FUSE LWRS
NGC 4631 Field I	8600 ± 1800	FUSE LWRS
NGC 891 ^b		
NGC 891 Field 1	< 2200	FUSE LWRS
NGC 891 Field 2	2300 ± 700	FUSE LWRS
NGC 891 Field 3	< 2700	FUSE LWRS
M82 ^c		
M82 Pointing A	$<$ 1.87 \times 10 5	FUSE LWRS
M82 Pointing B	$<$ 1.87 \times 10 5	FUSE LWRS
M82 Pointing C	$<$ 1.52 $ imes$ 10 5	FUSE LWRS
M82 Pointing D	$<$ 1.55 \times 10 5	FUSE LWRS
Haro 11 ^d	5.65 ± 1.96 × 10 ⁴	FUSE LWRS
NGC 1705 ^e	$<$ 2.5 $ imes$ 10 4	FUSE
J1156 ^f	$3.8^{+0.87}_{-0.79} \times 10^4$	HST/COS ACS/SBC

 $^{^{\}rm a}\,$ Intensities of the O VI 1032 Å emission line.

^b The flux values are taken from Chung et al. (2021).

The flux values are taken from Hoopes et al. (2003). The original unit of the flux is erg s⁻¹ cm⁻² and we convert the flux value into unit of LU. We use the whole area of the aperture to do the unit conversion based on the map provided by MAST.

 $^{^{}m d}$ The flux values are taken from Grimes et al. (2007). The original unit of the flux is erg s $^{-1}$ cm $^{-2}$ and we convert the flux value into unit of LU. We use the whole area of the aperture to do the unit conversion based on the map provided by MAST.

^e The flux value is taken from Heckman et al. (2001).

 $^{^{\}rm f}$ The flux value of I_{1038} is taken from Hayes et al. (2016). The original unit of the flux is erg s $^{-1}$ cm $^{-2}$ and we convert the flux value into unit of LU. Instead of using the whole area of the aperture in the unit conversion, we estimate and use the area occupied by the observed object within the aperture based on the map provided by MAST. The estimated value of this occupied area is 32 arcsec 2 . We estimate the value of I_{1032} based on the ratio $\frac{I_{1032}}{I_{1038}}\approx 2$.

Table 5.2: FUSE LWRS Apertures toward Galaxies

Target Name	Angular Separation ^a (arcsec)	s ^a (kpc)	z^{b}	RAc	DECc
7100		(kpc)	(kpc)		
NGC 1068	108.0	7.54		02:42:46.09	-00:01:59.54
NGC 4631 ^d					_
NGC 4631 Field A	126.9	4.46	4.9	12:42:08.80	+32:34:36.00
NGC 4631 Field B	67.4	2.37	2.7	12:42:08.80	+32:33:36.00
NGC 4631 Field F	148.8	5.23	2.8	12:42:18.00	+32:33:48.00
NGC 4631 Field H	157.6	5.54	2.4	12:41:56.00	+32:33:12.00
NGC 4631 Field I	44.4	1.56	1.6	12:42:10.00	+32:33:06.00
NGC 891 ^e					
NGC 891 Field 1	51.0	2.46	2.0	02:22:29.00	+42:21:12.00
NGC 891 Field 2	123.8	5.91	1.5	02:22:40.00	+42:22:36.00
NGC 891 Field 3	146.1	7.05	4. I	02:22:44.80	+42:22:12.00
M82 ^f					
M82 Pointing A	60.8	1.09	1.04	09:55:57.10	+69:39:49.50
M82 Pointing B	96.4	1.73	1.67	09:56:00.00	+69:39:17.10
M82 Pointing C	128.8	2.31	2.22	09:55:52.30	+69:42:54.50
M82 Pointing D	129.3	2.32	1.94	09:56:03.10	+69:38:48.00

^a The angular separation between the pointing direction and the galaxy's center, in the plane of the sky

b The pointing direction's height above the galaxy's disk

^c The pointing direction of the FUSE LWRS aperture

^d The values of z for FUSE apertures are given in Chung et al. (2021). We convert the value of angular separation and s from values of z based on the averaged distance from Tully (1988) and Seth et al. (2005).

^e The values of z for FUSE apertures are given in Chung et al. (2021). We convert the value of angular separation and s from values of z based on the averaged distance from Radburn-Smith et al. (2011) and Tully et al. (2009).

f We estimate the value of angular separation, s, and z based on the averaged distance from Karachentsev et al. (2004) and Sakai & Madore (1999).

CHAPTER 6

Conclusion

This dissertation has investigated the complex physical nature of the CGM by focusing on the interaction between cool, dense HVCs and the hot, diffuse ambient gas. Through a suite of hydrodynamic simulations utilizing the FLASH code, coupled with a non-equilibrium ionization (NEI) module and a table for radiative cooling, we have developed a more physically robust framework for interpreting observational data of the turbulent and ionized material that pervades the outer halos of galaxies.

A primary contribution of this work is the development of a new methodology for estimating the total mass of Galactic HVCs and intergalactic clouds from observations of highly ionized species. Our simulations demonstrate that in the dynamic environment of turbulent mixing layers, the ionization fractions of O VI, C IV, and Si IV are significantly lower than the peak values predicted by static CIE models. This finding has profound implications, suggesting that the total hydrogen mass associated with observed column densities of these ions has been systematically underestimated. When applied to observations of prominent HVCs like Complex C and the Magellanic Stream, our revised ionization fractions yield substantially higher mass estimates, indicating that these structures represent a much larger reservoir of baryonic material than previously accounted for.

Furthermore, this research provides a compelling physical explanation for the long-standing puzzle of narrow O VI absorption lines observed in the CGM and IGM. Our models show that NEI effects, specifically the time lag in recombination as hot gas mixes with cool gas and radiatively cools, allow for a

significant amount of O VI to exist in cool gas ($T\ll 10^5~{\rm K}$). By generating synthetic absorption spectra from our simulations, we successfully reproduced a wide range of Doppler broadening parameters (b values), from the very narrow to the very broad. The narrow components, which are difficult to explain with traditional models, arise naturally from this cool, recombining O VI within the multiphase mixing layers. This result demonstrates that turbulent mixing and NEI are key mechanisms shaping the thermal and kinematic properties of the CGM.

The scope of this dissertation also extends to observational constraints on the distribution of hot gas in active galaxies. We performed a case study of the starburst galaxy NGC 1068, analyzing archival FUSE data to search for O VI emission. Our analysis yielded very low emission intensity measurements, placing stringent upper limits on the emission from the galaxy's extended disk, approximately 8.3 kpc from its active nucleus. These tight constraints indicate that the powerful outflows from the central AGN and starburst activity do not necessarily enrich the entire outer disk and halo with hot, emissive gas. This result, particularly the uncommonly low O VI emission intensity when compared to other starburst or star-forming galaxies, underscores the inhomogeneous nature of energy and metal transport from a galaxy's central engine into the CGM.

In summary, this work contributes to our understanding of the CGM by demonstrating the critical role of dynamic mixing and non-equilibrium physics. The methodologies and insights presented here enable a more physically grounded interpretation of observational data. Compared to the predictions from static CIE or photoionization models, this work reveals a CGM that is more massive, more thermally complex, and more kinematically turbulent.

APPENDIX A

FITTING AND ESTIMATED RESULTS FOR RUN 2 TO RUN 10

Table A.i: Run 2 at 100 Myrs

	Table A.I: Ruii 2 at 100 Myrs							
Dir	ection			Componen	ts		$\log N(O VI)$	
Dire	ection	v_c (km s ⁻¹)	$b (\mathrm{km} \mathrm{s}^{-1})$	b_T (km s ⁻¹)	b_{vg} (km s ⁻¹)	$\log N(OVI)$	$\log N(OVI)_{sim}$	
у	yı	-0.7±0.1	7.8±0.1	1.9	7.6	14.06±0.01	15.08	
	y2	-3.7±0.1	11.7±0.1	1.9	11.5	14.58±0.01	15.16	
	у3	-II.5±0.2	30.7±0.4	18.7	24.3	13.11±0.01	13.91	
		-1.9±0.1	7.1±0.1	5.7	4.2	13.69±0.01		
Z	ZI	-17.4±8.7	54.4±11.3	8.7	53.7	13.07±0.13	15.87	
		-1.4±0.1	15.5±0.2	2.3	15.3	15.03±0.01		
	Z2	-1.5±0.1	13.8±0.1	2. I	13.6	14.65±0.01	15.28	
	Z 3	-5.4±5.1	17.6±2.5	2.5	17.4	14.24±0.32	15.19	
		1.8±0.2	11.3±1.7	2.4	II.O	14.76±0.04		
oblique	obliquei	-8.7±0.1	8.6±0.1	1.8	8.4	14.15±0.01	15.02	
	oblique2	1.1±0.1	14.8±0.1	1.9	14.7	14.88±0.01	15.40	
	oblique3	0.6±0.1	7.9±0.1	2. I	7.6	13.98±0.01	14.93	

Table A.2: Run 2 at 150 Myrs

	Components							
Dire	ection	Components					$\log N(OVI)_{sim}$	
		v_c (km s ⁻¹)	$b ({\rm km \ s^{-1}})$	$b_T (\mathrm{km} \mathrm{s}^{-1})$	b_{vg} (km s ⁻¹)	$\log N(OVI)$		
у	уı	-0.2±0.1	10.3±0.1	2. I	IO.I	14.38±0.01	15.16	
	y2	-4.8±0.1	11.7±0.1	1.8	11.6	14.57±0.01	15.13	
	у3	-8.1±0.1	13.6±0.2	2.2	13.4	14.85±0.02	15.47	
Z	ZI	6.4±0.1	18.4±0.5	2.4	18.2	15.59±0.04	16.18	
		19.0±1.0	33.9±4.0	3.0	33.8	13.79±0.32		
	Z2	7.2±0.1	16.6±0.2	2.2	16.5	15.39±0.02	15.72	
	Z 3	-13.6±9.9	36.3±13.9	22.6	28.4	13.02±0.20	15.51	
		13.5±0.1	15.0±0.1	2.5	14.8	14.87±0.01		
oblique	obliquei	1.1±0.1	12.I±0.3	2.0	11.9	14.59±0.02	15.00	
		26.6±1.1	9.4±1.6	3.0	8.9	12.95±0.08		
	oblique2	-0.6±0.1	9.5±0.1	1.9	9.3	14.32±0.01	15.31	
	oblique3	7.5±0.2	12.2 ± 0.8	2.6	11.9	14.77±0.06	15.57	
		42.0±0.2	17.3±0.5	3.4	17.0	14.86±0.03		

Table A.3: Run 2 at 200 Myrs

	Table 11.3. Rull 2 at 200 1/1/15							
Dire	ection			Componen	its		$\log N(OVI)_{sim}$	
Dire	Ction	v_c (km s ⁻¹)	$b (\mathrm{km} \mathrm{s}^{-1})$	b_T (km s ⁻¹)	b_{vg} (km s $^{-1}$)	$\log N(OVI)$	$\int \log IV (O V I)_{sim}$	
у	уı	4.3±0.1	10.6±0.1	2.0	10.4	14.52±0.01	15.37	
	y2	-6.3±0.1	10.4±0.1	2. I	10.2	14.36±0.01	15.35	
	у3	2.I±0.I	8.1±0.1	1.5	8.0	14.12±0.01	15.10	
Z	ZI	15.0±0.1	19.4±0.2	2.2	19.3	15.35±0.02	16.39	
	Z2	14.8±0.1	18.3±0.1	2. I	18.2	15.32±0.01	16.21	
	Z 3	5.9±2.3	37.1±2.6	36.7	5.4	13.28±0.05	15.55	
		25.5±0.1	13.5±0.1	2.6	13.2	14.66±0.01		
oblique	obliquei	-3.5±0.1	10.4±0.1	2.0	10.2	14.46±0.01	15.32	
	oblique2	10.3±0.1	13.4±0.1	2. I	13.2	14.69±0.01	15.36	
	oblique3	4.4±0.1	9.8±0.1	1.5	9.7	14.34±0.01	15.17	

Table A.4: Run 3 at 100 Myrs

Din	ection			Componen	ts		$\log N(OVI)_{sim}$
Dire	ction	v_c (km s ⁻¹)	$b (\mathrm{km} \mathrm{s}^{-1})$	b_T (km s ⁻¹)	b_{vg} (km s ⁻¹)	$\log N(OVI)$	$\log N (O V I)_{sim}$
y	уı	-5.I±0.3	18.5±0.6	6.4	17.4	13.44±0.03	14.70
		-3.6±0.1	6.8±0.2	2.4	6.4	14.03±0.01	
	y2	-17.6±2.1	23.7 ± 2.5	2.5	23.6	14.08±0.06	14.93
		-0.7±0.2	10.7±0.4	2.0	10.5	14.41±0.03	
	у3	-21.9±1.3	36.7±1.9	26.4	25.5	13.19±0.03	15.14
		-2.6±0.1	8.9±0.1	2.2	8.6	14.22±0.01	
Z	ZI	27.8±0.1	26.6±0.5	2.4	26.5	16.36±0.15	16.21
	Z2	32.4±0.2	22.2 ± 0.7	3.6	21.9	15.27±0.01	15.32
		77.I±2.2	18.1±4.6	15.3	9.7	13.34±0.09	
	Z3	26.5±0.7	10.1±0.7	3.0	9.6	14.21±0.06	14.71
		45.6±0.6	16.4±0.8	3.8	16.0	14.78±0.03	
oblique	obliquei	-2.6±0.1	12.7±0.2	2.2	12.5	14.46±0.01	14.99
	oblique2	4.0±0.1	13.2±0.1	1.9	13.1	14.63±0.01	14.97
	oblique3	14.4±0.1	п.6±о.і	2.2	II . 4	14.48±0.01	15.25
		32.5±0.9	13.5±1.4	2.4	13.3	12.68±0.05	

Table A.5: Run 3 at 150 Myrs

Die	ection			Componen	ts		$\log N(OVI)_{sim}$
Dill	ection	v_c (km s ⁻¹)	$b (\mathrm{km s^{-1}})$	b_T (km s ⁻¹)	b_{vg} (km s ⁻¹)	$\log N(OVI)$	$\int \log IV (O V I)_{sim}$
y	yı	-6.5±0.2	10.5±0.4	2.2	10.3	14.22±0.02	I4.34
	y2	-11.6±0.6	15.3±0.5	2.3	15.1	13.81±0.03	14.71
		-2.7±0.1	6.7±0.2	2.2	6.3	13.95±0.02	
	у3	-10.9±0.2	24.4±0.3	9.0	22.7	12.94±0.01	15.05
		-2.7±0.1	8.2±0.1	2. I	7.9	14.11±0.01	
Z	ZI	49.5±0.1	24.6±0.2	2.4	24.5	16.08±0.03	16.18
	Z2	51.0±0.3	19.1±1.0	3.2	18.8	15.06±0.05	15.66
		51.1±1.2	48.2±4.7	14.1	46.I	14.31±0.08	
	Z 3	49.0±0.3	10.7±0.4	5.2	9.4	14.31±0.05	15.71
		57.9±2.3	50.0±7.8	15.2	47.6	13.54±0.12	
		61.8±1.8	19.5±2.0	5.6	18.7	14.15±0.09	
oblique	obliquei	7.0±0.1	11.9±0.1	2.2	11.7	14.51±0.01	15.00
		28.9±0.1	8.3±0.3	3. I	7.7	13.26±0.01	
	oblique2	16.8±0.1	14.8±0.2	2.3	14.6	14.62±0.01	14.72
		53.5±0.9	12.0±1.7	10.4	6.0	13.13±0.06	
	oblique3	15.6±0.1	8.7±0.1	1.8	8.5	14.21±0.01	14.97

Table A.6: Run 3 at 200 Myrs

		I		11.0. 16411) 46 2			
Dire	ection			Componen	ts		$\log N(OVI)_{sim}$
Dire	ction	v_c (km s ⁻¹)	$b (\mathrm{km} \mathrm{s}^{-1})$	b_T (km s ⁻¹)	b_{vg} (km s ⁻¹)	$\log N(OVI)$	$\log N (O V I)_{sim}$
y	уı	-5.2±0.2	11.4±0.2	2.0	II.2	14.33±0.01	14.78
	y2	1.1±0.1	10.0±0.2	1.9	9.8	14.36±0.01	14.96
	у3	-0.9±0.1	9.5±0.1	2.2	9.2	14.33±0.01	14.88
Z	ZI	66.0±0.1	19.1±0.2	2.3	19.0	15.65±0.03	16.14
	Z2	69.7±0.1	18.6±0.2	2.5	18.4	15.33±0.02	15.98
	Z3	69.2±0.1	17.5±0.2	2.2	17.4	15.44±0.03	15.96
oblique	obliquei	19.7±0.1	13.8±0.3	1.9	13.7	14.63±0.02	14.77
		44.6±0.6	7.3±0.9	2.8	6.7	13.28±0.04	
	oblique2	22.6±0.1	11.5±0.1	1.9	11.3	14.47±0.01	14.78
		37.7±0.1	7.1±0.1	2.7	6.6	13.47±0.01	
	oblique3	26.1±0.1	8.6±0.1	2. I	8.3	14.15±0.01	14.78

Table A.7: Run 4 at 100 Myrs

Dire	ection	Components					$\log N(OVI)_{sim}$
Dire	ection	v_c (km s ⁻¹)	$b (\mathrm{km} \mathrm{s}^{-1})$	b_T (km s ⁻¹)	b_{vg} (km s $^{-1}$)	$\log N(OVI)$	$\int \log IV (O V I)_{sim}$
y	yı	-10.8±1.8	17.7±1.3	16.5	6.4	13.38±0.08	15.13
		-1.5±0.1	8.9±0.1	2.7	8.5	14.18±0.01	
	y2	-45.5±0.4	13.7±0.7	2.5	13.5	14.15±0.02	15.02
		-5.4±0.2	8.3±0.4	2. I	8.0	14.10±0.03	
	у3	-21.7±0.1	8.4±0.2	5.6	6.3	13.51±0.01	14.74
		-19.8±0.5	32.4±0.9	14.5	29.0	13.53±0.02	
		-6.1±0.1	8.1±0.1	3.8	7.2	14.18±0.01	
Z	ZI	36.3±0.4	15.3±1.1	2.5	15.1	14.94±0.09	15.92
		93.8±0.8	28.2 ± 1.7	6.2	27.5	15.27±0.13	
		133.1±5.7	106.7±5.8	14.5	105.7	14.92±0.04	
	Z2	36.7±2.9	14.9±2.2	2.2	14.7	14.97±0.23	15.79
		75.0±2.1	42.4±1.7	2.3	42.3	15.32±0.04	
	Z3	138.4±0.5	11.8±1.2	II.4	3.0	14.16±0.06	14.48
		152.2±4.0	30.2±4.0	26.0	15.4	13.96±0.10	
oblique	obliquei	26.3±0.1	17.1±0.2	2. I	17.0	15.13±0.01	15.40
		55.6±1.7	23.2 ± 2.4	13.1	19.1	13.55±0.05	
	oblique2	26.3±0.1	11.2 ± 0.2	2.4	10.9	14.40±0.01	15.23
		81.3±0.3	13.0±0.6	9.3	9.1	13.78 ± 0.02	
		111.4±13.6	104.7±8.0	26.6	101.3	13.92±0.03	
	oblique3	37.4±0.2	9.0±1.3	2. I	8.8	14.28±0.03	14.76
		54.3±1.0	9.3±3.1	5.5	7.5	13.55±0.09	
		76.4±4.1	62.2±5.8	29.7	54.7	13.89±0.05	

Table A.8: Run 4 at 150 Myrs

Direction			$\log N(OVI)_{sim}$				
	Direction		$b (\mathrm{km} \mathrm{s}^{-1})$	b_T (km s ⁻¹)	b_{vg} (km s ⁻¹)	$\log N(OVI)$	$\log N (O V I)_{sim}$
y	yı	-2.0±0.1	15.1±0.4	2. I	15.0	14.79±0.03	15.41
	y2	-30.2±0.4	8.7±0.6	3.6	7.9	13.27±0.03	15.11
		-1.1±0.1	12.7±0.2	2. I	12.5	14.48±0.01	
	у3	-14.2±1.8	23.6±2.2	15.4	17.9	13.20±0.06	15.26
		2.7±0.1	10.8±0.1	2.5	10.5	14.41±0.01	
Z	ZI	61.3±11.1	20.8±5.4	2. I	20.7	16.10±0.86	16.31
		120.0±5.1	67.3 ± 3.6	3.2	67.2	15.63±0.07	
	Z2	93.5±0.3	47.5±1.5	3.3	47.4	16.07±0.09	16.12
		208.6±2.6	49.3±5.5	18.4	45.7	14.23±0.04	
	Z 3	69.5±2.9	21.6±3.2	2.4	21.5	14.79±0.15	14.94
		96.7±8.8	35.6±8.1	4.4	35.3	14.66±0.20	
		221.6±2.5	39.4±4.9	17.4	35.3	14.05±0.05	
oblique	obliquei	25.0±0.2	13.5±0.3	2. I	13.3	14.69±0.02	15.01
		54.8±1.5	26.7±2.7	5.6	26.I	13.84±0.04	
	oblique2	34.5±0.1	12.4±0.1	2.2	12.2	14.61±0.01	15.21
	oblique3	58.3±0.1	10.8±0.3	2.2	10.6	14.42±0.01	15.15
		65.7±1.5	30.0±2.3	6.1	29.4	13.65±0.06	

Table A.9: Run 4 at 200 Myrs

Direction			$\log N(OVI)_{sim}$				
Dire	ction	v_c (km s ⁻¹)	$b (\mathrm{km} \mathrm{s}^{-1})$	b_T (km s ⁻¹)	b_{vg} (km s ⁻¹)	$\log N(OVI)$	$\int \log IV (O V I)_{sim}$
y	уı	4.5±0.1	12.4±0.1	2.2	12.2	14.60±0.01	15.30
	y2	-1.2±0.1	9.5±0.1	1.7	9.3	14.33±0.01	14.93
	у3	-31.4±2.7	23.5±5.1	16.3	16.9	13.86±0.09	15.01
		-5.5±0.3	12.0±1.1	2.3	11.8	14.71±0.09	
Z	ZI	58.6±0.8	13.9±1.0	2.2	13.7	15.76±0.18	16.31
		110.7±0.9	27.0±1.2	3.3	26.8	16.16±0.02	
		171.3±2.4	57.6±3.3	24.8	52.0	14.27±0.03	
	Z2	65.1±0.2	24.8±1.0	2.3	24.7	15.56±0.08	15.81
		130.8±0.4	23.9±1.3	8.7	22.3	14.64±0.03	
		170.3±9.9	75.4±12.3	23.5	71.6	14.30±0.10	
	Z 3	101.3±0.3	31.1±1.1	3.3	30.9	15.70±0.01	15.58
oblique	obliquei	16.4±0.2	10.3±0.4	I.4	10.2	14.28±0.02	14.84
		41.5±0.4	15.9±0.9	1.7	15.8	13.94±0.02	
		74.9±1.0	8.5±1.5	3.6	7.7	13.09±0.07	
	oblique2	37.1±0.3	п.9±0.4	3.3	II.4	14.51±0.03	15.12
		66.3±0.7	26.1±1.2	4.6	25.7	14.36±0.02	
	oblique3	56.2±0.6	9.4±1.1	2.2	9.1	14.29±0.08	15.24
		72.5±1.9	23.6±2.2	2.6	23.5	14.42±0.06	

Table A.10: Run 5 at 100 Myrs

Direction			$\frac{1}{\log N(O MI)}$				
		v_c (km s ⁻¹)	$b (\mathrm{km} \mathrm{s}^{-1})$	b_T (km s ⁻¹)	b_{vg} (km s ⁻¹)	$\log N(OVI)$	$\log N(OVI)_{sim}$
у	уı	-2.I±0.I	6.7±0.1	2.0	6.4	13.68±0.01	13.94
	y2	-0.2±0.1	7.9±0.1	1.9	7.7	13.78±0.01	13.97
	у3	2.7±0.1	10.9±0.1	2. I	10.7	14.36±0.01	14.59
Z	ZI	2.5±0.1	6.9±0.1	4.4	5.3	13.68±0.01	13.86
	Z2	5.7±0.1	7.5±0.1	3.8	6.5	13.71±0.01	13.95
	Z3	3.1±0.1	7.1±0.1	3.3	6.3	13.93±0.01	14.15
oblique	obliquei	-2.9±0.1	6.6±0.1	2. I	6.3	13.68±0.01	13.77
	oblique2	-3.2±0.1	7.6±0.1	2. I	7.3	13.88±0.01	13.96
	oblique3	-3.9±0.1	7.9±0.1	2.7	7.4	13.90±0.01	13.94

Table A.11: Run 5 at 150 Myrs

Direction							
		$v_c (\mathrm{km s^{-1}})$	$b (\mathrm{km} \mathrm{s}^{-1})$	Componen $b_T (\text{km s}^{-1})$	b_{vg} (km s ⁻¹)	$\log N(OVI)$	$\log N(OVI)_{sim}$
y	yı	-2.I±0.I	6.8±0.1	2.0	6.5	13.66±0.01	13.89
	y2	-6.0±0.1	6.9±0.1	2. I	6.6	13.78±0.01	13.95
	у3	-1.2±0.1	9.4±0.1	2.2	9.1	14.23±0.01	14.54
Z	ZI	10.8±0.1	6.3±0.1	3.3	5.4	13.78±0.01	14.17
		17.4±0.1	18.4±0.1	9.7	15.6	13.46±0.01	
	Z2	16.6±0.1	6.4±0.1	3.6	5.3	13.77±0.01	14.12
		18.3±0.1	15.5±0.1	12.0	9.8	13.67±0.01	
	z 3	16.0±0.1	7.5±0.1	5.2	5.4	13.98±0.01	14.30
		21.5±0.1	19.6±0.2	5.4	18.8	13.72±0.01	
oblique	obliquei	-4.6±0.1	6.7±0.1	2.0	6.4	13.71±0.01	13.90
	oblique2	5.7±0.1	8.1±0.1	2.3	7.8	13.84±0.01	13.87
	oblique3	1.9±0.1	10.8±0.1	2.2	10.6	14.36±0.01	14.56

Table A.12: Run 5 at 200 Myrs

Table 11.12. Rull) at 200 Wyls								
Direction			$\log N(O VI)$					
		v_c (km s ⁻¹)	$b (\mathrm{km} \mathrm{s}^{-1})$	b_T (km s ⁻¹)	b_{vg} (km s ⁻¹)	$\log N(OVI)$	$\log N(OVI)_{sim}$	
y	yı	-9.9±0.1	9.0±0.1	3.3	8.4	13.62±0.01	13.56	
	y2	-1.6±0.1	6.9±0.1	2. I	6.6	13.59±0.01	13.78	
	у3	5.1±0.3	19.1±0.5	2.2	19.0	14.44±0.01	14.35	
Z	ZI	16.1±0.2	15.8±0.3	3.9	15.3	14.63±0.01	14.86	
		34.0±0.4	10.2±0.5	4. I	9.3	13.96±0.03		
	Z2	33.5±0.2	15.2±0.4	4.6	14.5	14.28±0.01	14.30	
	Z3	37.9±0.1	10.6±0.1	5.7	8.9	14.04±0.01	14.06	
oblique	obliquei	4.I±0.I	7.7±0.1	2.4	7.3	13.62±0.01	13.59	
	oblique2	3.1±0.1	7.1±0.1	2. I	6.8	13.71±0.01	13.87	
	oblique3	12.3±0.1	11 . 5±0.1	2.2	11.3	13.85±0.01	13.76	

Table A.13: Run 6 at 100 Myrs

Dir	ection			Componen	ts		$\log N(OVI)_{sim}$
Dire	Ction	v_c (km s ⁻¹)	$b (\mathrm{km} \mathrm{s}^{-1})$	b_T (km s ⁻¹)	b_{vg} (km s $^{-1}$)	$\log N(OVI)$	$\int \log IV (O V I)_{sim}$
y	уı	-0.5±0.1	9.5±0.1	2.3	9.2	14.30±0.01	14.97
	y2	-11.6±0.2	13.0±0.2	2. I	12.8	14.95±0.06	14.92
	у3	-22.0±0.2	9.2±0.4	3.8	8.4	13.43±0.02	14.74
		-3.0±0.1	10.2±0.2	2. I	10.0	14.39±0.01	
Z	ZI	21.0±0.9	67.0±1.1	16.8	64.9	14.23±0.01	15.43
		26.9±0.1	14.3±0.2	4.4	13.6	14.78±0.01	
		56.7±0.1	16.7±0.2	5.4	15.8	14.83±0.01	
	Z2	36.2±0.1	16.6±0.2	2.8	16.4	14.93±0.02	15.34
		64.8±0.1	9.2±0.2	6.0	7.0	14.20±0.01	
	Z3	49.4±0.1	16.9±0.3	2.4	16.7	15.30±0.02	15.15
oblique	obliquei	12.8±0.1	13.9±0.2	1.9	13.8	15.02±0.02	15.07
	oblique2	19.7±0.1	14.3±0.3	2.2	14.1	14.98±0.03	15.03
	oblique3	27.5±3.2	15.1±1.9	2.4	14.9	14.83±0.06	14.98
		46.1±3.0	10.9±1.6	2.4	10.6	14.50±0.27	

Table A.14: Run 6 at 150 Myrs

D:				Componen	<u> </u>		low M(O I/I)
Dire	ection	$v_c (\mathrm{km \ s^{-1}})$	$b (\mathrm{km} \mathrm{s}^{-1})$	$b_T (\mathrm{km s^{-1}})$	b_{vg} (km s ⁻¹)	$\log N(OVI)$	$\log N(OVI)_{sim}$
y	уı	-8.6±1.4	12.6±0.6	2.2	12.4	13.79±0.12	14.73
		-3.2±0.1	9.2±0.2	2.2	8.9	14.14±0.06	
	y2	-10.5±0.1	11.0±0.1	2. I	10.8	14.42±0.01	14.82
	у3	-0.4±0.1	8.3±0.1	2.2	8.0	14.04±0.01	14.61
Z	ZI	59.8±0.1	27.6±0.6	2.2	27.5	16.22±0.15	16.07
	Z2	78.3±0.1	16.6±0.4	2.6	16.4	14.87±0.03	14.87
	Z 3	90.3±0.1	11.9±0.2	2.2	11.7	14.40±0.01	14.43
oblique	obliquei	22.3±0.1	13.1±0.1	2. I	12.9	14.59±0.01	14.89
		47.7±0.3	11.4±0.6	5. I	10.2	13.24±0.02	
	oblique2	17.0±0.1	9.9±0.1	2. I	9.7	14.33±0.01	14.88
		37.0±0.1	9.4±0.1	2.3	9.1	14.17±0.01	
	oblique3	-3.2±0.3	7.3±0.6	2.2	7.0	13.95±0.07	14.42
		4.2±1.6	16.7±1.3	2.3	16.5	13.88±0.08	

Table A.15: Run 6 at 200 Myrs

	Table 11.15. Teuri o at 200 iviyis									
Die	ection			Componen			$\log N(OVI)_{sim}$			
Dire	ection	v_c (km s ⁻¹)	$b (\mathrm{km} \mathrm{s}^{-1})$	b_T (km s ⁻¹)	b_{vg} (km s $^{-1}$)	$\log N(OVI)$	$\int \log W(O V I)_{sim}$			
y	yı	-9.6±3.3	14.7±2.2	1.9	14.6	13.78±0.20	14.68			
		-0.9±0.3	8.6 ± 0.8	1.9	8.4	14.15±0.08				
	y2	-6.9±0.1	13.4±0.1	2. I	13.2	13.69±0.01	14.71			
		-2.6±0.1	7.3±0.1	2. I	7.0	14.02±0.01				
	у3	1.8±0.1	11.0±0.1	1.9	10.8	14.40±0.01	14.62			
Z	ZI	65.7±0.2	25.8±0.7	2.0	25.7	16.23±0.21	16.08			
	Z2	65.7±0.2	28.5±0.8	2.3	28.4	15.85±0.16	15.70			
	Z 3	54.3±0.7	16.1±0.9	2. I	16.0	14.86±0.05	15.25			
		81.9±0.8	16.9±0.8	2.2	16.8	14.87±0.05				
oblique	obliquei	13.5±0.1	14.0±0.2	2.3	13.8	14.89±0.02	15.06			
	oblique2	27.7±0.1	15.2±0.1	2. I	15.1	14.76±0.01	14.73			
	oblique3	25.7±0.1	11.4±0.1	2.1	II.2	14.53±0.01	14.85			

Table A.16: Run 7 at 100 Myrs

D:				Componen	ts		low N(O I/I)
Dire	ection	v_c (km s ⁻¹)	$b (\mathrm{km} \mathrm{s}^{-1})$	$b_T (\mathrm{km} \mathrm{s}^{-1})$	b_{vg} (km s ⁻¹)	$\log N(OVI)$	$\log N(OVI)_{sim}$
y	yı	-6.5±0.5	28.8±0.6	19.1	21.6	13.27±0.02	15.22
		1.1±0.1	8.4±0.1	2.3	8.1	14.19±0.01	
	y2	-23.3±0.6	8.5±1.0	4.9	6.9	12.95±0.04	15.12
		2.4±0.1	12.5±0.2	1.7	12.4	14.55±0.01	
	у3	-8.7±0.1	17.0±0.4	1.7	16.9	15.53±0.02	15.38
Z	ZI	-23.I±1.3	72.4±3.9	31.6	65.1	13.78±0.03	15.86
		-18.6±0.1	21.3±0.2	2.9	2I.I	15.75±0.02	
	Z2	-25.0±3.3	71.9±11.8	19.8	69.1	13.80±0.09	15.35
		8.4±0.3	18.6±0.5	2.5	18.4	14.80±0.02	
	Z3	-19.0±1.6	17.2±3.4	2.5	17.0	12.80±0.07	15.52
		15.6±0.1	17.3±0.2	2.8	17.1	14.93±0.01	
		47.0±0.4	13.0±0.8	6.6	II.2	13.22±0.03	
oblique	obliquei	-1.5±0.1	8.8±0.1	2.0	8.6	14.15±0.01	14.96
		12.4±1.6	40.8±2.4	22.0	34.4	12.95±0.03	
	oblique2	-12.3±0.1	17.3±0.1	1.7	17.2	14.92±0.01	15.30
	oblique3	-16.2±0.5	14.8±0.6	1.6	14.7	14.70±0.02	15.35
		4.4±0.5	12.8±0.6	1.6	12.7	14.46±0.03	

Table A.17: Run 7 at 150 Myrs

Dina	ati an			Componen			$\log N(O VI)$
Dire	ection	v_c (km s ⁻¹)	$b (\mathrm{km} \mathrm{s}^{-1})$	$b_T (\mathrm{km} \mathrm{s}^{-1})$	b_{vg} (km s $^{-1}$)	$\log N(OVI)$	$\log N(OVI)_{sim}$
y	yı	-5.1±2.8	15.1±1.0	4.7	14.3	13.23±0.22	15.41
		0.4±0.1	8.3±0.3	1.8	8.1	14.19±0.02	
	y 2	-25.I±0.5	6.5±0.6	3.4	5.5	13.00±0.02	15.17
		2.0±0.1	13.8±0.1	1.5	13.7	14.76±0.01	
	у3	-120.5±5.0	38.4±10.9	16.3	34.8	13.26±0.10	14.79
		-73.1±0.6	16.6±1.4	13.0	10.3	13.67±0.03	
		-47.4±0.5	7.0±0.6	2.7	6.5	13.33±0.04	
		-3.9±0.1	9.6±0.3	2.0	9.4	14.12±0.01	
Z	ZI	-27.7±8.1	77.0±13.5	30.7	70.6	13.87±0.11	15.82
		-14.6±0.2	23.2±0.5	2.5	23.I	15.16±0.02	
		78.8±2.4	44.4±4.I	3.7	44.2	13.98±0.04	
		94.7±0.2	9.0±0.2	3.0	8.5	14.05±0.02	
	Z2	-103.1±4.4	73.3±5.9	20.0	70.5	13.97±0.05	15.70
		-9.6±0.3	24.0±0.7	2.0	23.9	15.21±0.05	
		42.4±1.5	9.1±2.8	4.I	8.1	13.09±0.11	
	z 3	-26.7±1.5	14.9±2.9	13.0	7.3	13.45±0.07	15.44
		20.3±0.3	22.5±0.5	2.4	22.4	14.95±0.02	
oblique	obliquei	-4.7±0.1	11.5±0.2	1.5	II.4	14.66±0.02	15.63
	oblique2	-16.5±0.1	11.2±0.1	1.8	II.I	14.58±0.01	15.30
		3.5±0.1	8.8±0.1	1.7	8.6	14.23±0.01	
	oblique3	5.8±0.3	15.4±1.0	2.2	15.2	15.17±0.08	15.22
		46.o±5.8	53.0±9.7	21.1	48.6	13.99±0.08	

Table A.18: Run 7 at 200 Myrs

Dire	ection			Componen	ts		$\log N(OVI)_{sim}$
	ction	v_c (km s ⁻¹)	$b (\mathrm{km} \mathrm{s}^{-1})$	b_T (km s ⁻¹)	b_{vg} (km s ⁻¹)	$\log N(OVI)$	$\log N (O V I)_{sim}$
у	уı	1.0±0.1	10.4±0.1	2. I	IO.2	14.36±0.01	15.34
	y2	-2.5±0.2	11.3±0.4	1.6	II.2	14.34±0.02	15.34
	у3	-2.2±0.I	11.5±0.1	1.7	II.4	14.56±0.01	14.94
		13.6±0.3	15.2±0.3	1.7	15.1	14.09±0.01	
Z	ZI	-67.2±8.1	44.9±0.1	23.6	38.2	13.65±0.14	15.85
		-12.9±0.4	17.5±1.2	2.2	17.4	15.13±0.10	
		54.6±1.1	43.8±2.2	3. I	43.7	14.65±0.02	
	Z2	24.5±0.1	19.4±0.3	3.0	19.2	15.48±0.03	15.73
		27.6±1.1	55.0±4.2	16.1	52.6	13.99±0.05	
	Z3	31.9±0.7	12.I±1.4	2.5	11.8	14.49±0.08	15.07
		42.7±2.0	23.7±1.4	3.0	23.5	14.46±0.08	
oblique	obliquei	-5.5±0.1	9.5±0.1	1.8	9.3	14.31±0.01	15.24
		7.5±0.1	8.1±0.1	1.8	7.9	13.57±0.01	
	oblique2	-3.5±0.1	15.5±0.2	1.6	15.4	15.09±0.02	15.32
	oblique3	35.8±0.2	8.o±o.6	2.4	7.6	13.93±0.02	14.94
		83.8±0.2	п.6±0.5	2.5	11.3	14.39±0.02	
		118.7±35.3	60.9±18.8	23.6	56.1	13.49±0.13	

Table A.19: Run 8 at 100 Myrs

Dir	Direction			Componen	ts		$\log N(OVI)_{sim}$
Dire	cction	v_c (km s ⁻¹)	b (km s ⁻¹)	b_T (km s ⁻¹)	b_{vg} (km s $^{-1}$)	$\log N(OVI)$	$\log N (O V I)_{sim}$
y	yı	3.6±0.1	10.1±0.1	2.2	9.9	14.36±0.01	15.10
		14.2±2.6	52.6±4.9	28.5	44.2	12.86±0.04	
	y2	-11.9±0.1	13.2±0.2	2.2	13.0	14.69±0.02	14.70
	у3	-9.3±0.2	13.8±0.3	2.0	13.7	14.50±0.02	14.95
Z	ZI	10.6±0.5	26.9±1.0	2.6	26.8	14.86±0.03	15.79
		67.4±0.4	20.I±0.9	2.7	19.9	15.03±0.06	
	Z2	7.6±0.3	17.0±0.8	1.8	16.9	14.89±0.06	15.38
		52.5±0.5	21.6±0.9	3.7	21.3	14.55±0.02	
	Z3	20.7±0.3	18.2 ± 1.0	2.5	18.0	15.22±0.09	15.40
		69.8±1.5	25.6±3.2	8.5	24.I	13.95±0.05	
oblique	obliquei	8.6±0.6	18.6±1.5	2. I	18.5	14.61±0.04	15.58
		37.3±2.3	14.3±5.5	2.2	14.1	13.63±0.15	
		57.3±1.3	9.4±3.3	2.6	9.0	13.43±0.12	
	oblique2	8.5±0.1	13.2±0.2	2.2	13.0	14.37±0.01	14.64
		26.5±0.1	9.2 ± 0.2	2.2	8.9	14.20±0.01	
	oblique3	23.6±0.2	10.5±0.4	1.8	10.3	14.27±0.02	14.96

Table A.20: Run 8 at 150 Myrs

Dina	ection			Componen	ts		$\log N(O VI)$
Dire	ection	$v_c (\mathrm{km s^{-1}})$	$b (\mathrm{km s^{-1}})$	b_T (km s ⁻¹)	b_{vg} (km s ⁻¹)	$\log N(OVI)$	$\log N(OVI)_{sim}$
y	yı	-3.4±0.2	12.8±0.3	1.6	12.7	14.49±0.02	I4.72
	y2	-30.I±2.8	45.5±4.8	3.2	45.4	13.26±0.04	15.39
		-2.5±0.1	9.3±0.1	2.0	9.1	14.16±0.01	
	у3	1.5±0.1	8.5±0.1	1.9	8.3	14.17±0.01	14.93
Z	ZI	9.9±0.2	21.0±0.6	2.6	20.8	15.21±0.05	16.24
		72.I±0.2	28.6±0.7	2.5	28.5	15.50±0.04	
	Z2	9.9±0.2	9.0±0.5	1.3	8.9	15.25±0.38	15.48
		29.9±0.3	11.1±0.5	2. I	10.9	14.10±0.02	
		60.4±0.2	п.6±0.3	4.2	10.8	14.05±0.01	
	Z 3	20.8±0.2	14.3±0.5	1.6	14.2	14.68±0.03	15.27
		64.0±0.5	8.1±2.4	5.0	6.4	13.62±0.08	
		82.4±3.0	43.3±4.2	4.7	43.0	13.97±0.05	
oblique	obliquei	8.2±0.9	14.7±1.9	2.2	14.5	14.36±0.15	14.64
		22.6±4.4	25.0±3.4	2.3	24.9	14.36±0.15	
	oblique2	7.4±0.6	11.3±0.8	2.2	II.I	14.41±0.05	14.66
		26.0±0.1	15.4±3.8	3.9	14.9	13.85±0.12	
	oblique3	29.3±0.1	11.7±0.2	1.9	11.5	14.26±0.01	I4.40

Table A.21: Run 8 at 200 Myrs

Dire	ection			Componen	ts		$\log N(OVI)_{sim}$
Dire	Ction	$v_c (\mathrm{km} \mathrm{s}^{-1})$	$b (\mathrm{km} \mathrm{s}^{-1})$	$b_T (\mathrm{km} \mathrm{s}^{-1})$	b_{vg} (km s ⁻¹)	$\log N(OVI)$	$\int \log IV (O V I)_{sim}$
y	уı	-II.4±5.3	20.6±4.4	10.0	18.0	13.01±0.20	15.11
		-0.4±0.1	9.2±0.2	2.7	8.8	14.24±0.01	
	y2	-7.2±0.1	17.3±0.3	2.0	17.2	14.86±0.02	14.87
	у3	-54.7±1.8	32.2 ± 3.9	9.1	30.9	13.70±0.04	14.60
		-8.3±0.2	15.7±0.4	2.2	15.5	14.55±0.02	
Z	ZI	45.8±0.2	30.1±1.1	2.2	30.0	16.26±0.03	16.11
	Z2	26.0±0.3	20.7±0.8	1.8	20.6	15.51±0.12	15.66
		75.8±0.3	18.1±0.7	4.9	17.4	14.48±0.02	
	Z 3	30.1±0.4	16.6±0.8	1.8	16.5	14.79±0.04	15.29
		65.4±5.1	35.1±0.3	2.0	35.0	13.79±0.11	
oblique	obliquei	4.9±0.1	14.2±0.1	1.7	I4.I	14.73±0.01	15.30
	oblique2	15.5±0.2	18.8±0.4	2.2	18.7	14.85±0.02	15.10
	oblique3	-7.1±0.1	10.2±0.1	2.0	10.0	14.25±0.01	14.94
		12.6±3.7	35.2±5.0	15.6	31.6	13.25±0.08	

Table A.22: Run 9 at 100 Myrs

Dim	ection			Componen	ts		$\log N(O MI)$
Dire	ection	v_c (km s ⁻¹)	$b (\mathrm{km} \mathrm{s}^{-1})$	b_T (km s ⁻¹)	b_{vg} (km s ⁻¹)	$\log N(OVI)$	$\log N(OVI)_{sim}$
y	уı	-7.7±0.1	13.5±0.2	2.I	13.3	14.86±0.02	15.39
	y2	-17.2±3.3	16.7±2.6	2.2	16.6	14.54±0.17	15.01
		-4.3±1.7	11.2±1.3	2.2	II.O	14.49±0.21	
	у3	-30.1±1.6	17.5±3.4	7.4	15.9	12.79±0.07	14.93
		-0.4±0.1	9.2±0.1	1.8	9.0	14.19±0.01	
Z	ZI	33.2±1.3	20.0±1.1	2.3	19.9	15.57±0.09	16.20
		84.5±2.4	30.6±2.5	3.5	30.4	15.35±0.06	
		120.1±6.5	91.4±5.8	28.6	86.8	14.67±0.06	
	Z2	35.0±0.5	9.0±2.2	1.9	8.8	15.27±0.97	15.67
		52.7±1.5	29.9±1.4	2.3	29.8	14.54±0.04	
		96.5±0.3	20.8±0.5	5.4	20.I	14.69±0.01	
		173.5±12.9	96.7±27.7	34.4	90.4	13.52±0.10	
	Z3	50.1±0.9	31.3±1.3	2.2	31.2	15.64±0.06	15.79
		113.6±1.0	28.5±2.4	3.2	28.3	15.41±0.09	
		163.5±0.7	14.0±1.3	6.8	12.2	14.00±0.04	
oblique	obliquei	4.7±0.3	9.7±0.7	2.0	9.5	14.23±0.03	15.21
		34.3±0.5	17.8±0.8	1.9	17.7	14.48±0.02	
	oblique2	16.2±0.5	12.0±0.7	2.2	11.8	14.54±0.04	15.22
		49.9±0.6	25.0±1.4	2.4	24.9	14.87±0.03	
	oblique3	31.5±0.1	8.2±0.1	1.8	8.0	14.17±0.01	15.00
		59.3±0.1	9.0±0.3	3.5	8.3	13.18±0.01	
		125.1±0.5	35.4±1.0	18.9	29.9	13.26±0.01	

Table A.23: Run 9 at 150 Myrs

Dim	ection			Componen	ts		$\log N(OVI)_{sim}$
Dire	ection	$v_c (\mathrm{km s^{-1}})$	$b (\mathrm{km} \mathrm{s}^{-1})$	b_T (km s ⁻¹)	b_{vg} (km s ⁻¹)	$\log N(OVI)$	$\log N(O V I)_{sim}$
у	yı	-0.6±0.1	15.4±0.3	2.5	15.2	15.28±0.03	15.44
	y2	-30.8±0.7	11.7±1.0	3.0	11.3	13.50±0.05	14.94
		-13.0±0.1	11.7±0.2	2.2	11.5	14.53±0.01	
	у3	-12.7±0.5	23.2±0.5	6.7	22.2	13.01±0.02	15.24
		-2.4±0.I	8.6±0.1	2.0	8.4	14.18±0.01	
Z	ZI	56.0±0.3	30.5±1.0	2.7	30.4	15.76±0.08	16.29
		143.0±0.4	24.6±0.6	3.0	24.4	15.12±0.02	
		185.4±2.5	2I.4±4.5	15.6	14.6	13.69±0.09	
	Z2	57.0±0.3	17.9±0.7	2.9	17.7	15.15±0.06	15.30
		115.4±0.5	38.9±1.0	6.2	38.4	14.89±0.01	
	Z 3	99.3±0.1	14.1±0.1	2.9	13.8	14.70±0.01	15.14
		122.3±0.2	18.0±0.3	7.0	16.6	14.35±0.01	
		162.2±2.2	46.5±4.0	30.7	34.9	13.37±0.04	
oblique	obliquei	13.2±0.1	13.7±0.2	2. I	13.5	14.79±0.01	15.45
		57.6±4.1	24.6±8.5	11.6	22.0	12.71±0.13	
	oblique2	23.I±0.I	16.4±0.3	2. I	16.3	15.17±0.10	15.12
		62.4±0.6	7.0±1.8	3.0	6.3	13.19±0.03	
	oblique3	19.8±0.2	9.9±0.4	2.3	9.6	14.36±0.03	15.36
		52.5±0.4	29.4±0.8	3.2	29.2	14.92±0.01	
		117.5±3.4	25.6±7.1	21.9	13.3	13.13±0.10	

Table A.24: Run 9 at 200 Myrs

D:				Componen			low M(O I/I)
Dire	ection	v_c (km s ⁻¹)	$b (\mathrm{km} \mathrm{s}^{-1})$	$b_T (\mathrm{km} \mathrm{s}^{-1})$	b_{vg} (km s $^{-1}$)	$\log N(OVI)$	$\log N(OVI)_{sim}$
у	уı	-33.0±1.6	8.2±7.1	4.2	7.0	12.70±0.17	15.09
		-4.2±0.1	12.3±0.4	2.0	12.1	14.59±0.03	
	y2	-31.5±0.8	9.0±1.1	4.2	8.0	13.34±0.07	14.92
		-II.4±0.2	12.6±0.4	2. I	12.4	14.59±0.02	
	у3	-19.0±0.7	12.7±1.1	2.0	12.5	14.41±0.04	15.06
		-2.4±0.6	8.6±0.9	2.0	8.4	14.24±0.05	
Z	ZI	35.9±0.7	13.4±0.5	2. I	13.2	14.67±0.04	16.63
		120.0±5.5	45.7±2.0	2.9	45.6	15.63±0.07	
		201.1±0.9	19.6±1.7	7.3	18.2	13.25±0.04	
	Z2	59.7±1.0	22.5±0.5	2.4	22.4	15.92±0.07	16.13
		111.3±0.6	20.6±0.9	4.7	20.I	15.98±0.11	
		155.7±1.1	60.7±1.2	29.0	53.3	14.77±0.01	
	Z3	52.7±0.1	18.1±0.4	2.8	17.9	15.42±0.05	15.67
		94.8±0.5	13.1±3.2	5.4	11.9	14.82±0.06	
		121.6±0.5	15.8±0.7	9.5	12.6	14.63±0.02	
		162.3±1.7	51.2±3.1	23.5	45.5	14.18±0.02	
oblique	obliquei	13.5±0.1	10.7±0.1	1.9	10.5	14.41±0.01	15.15
		21.1±0.1	7.1±0.1	1.9	6.8	13.94±0.01	
		41.0±0.1	10.3±0.1	3. I	9.8	13.18±0.01	
	oblique2	27.4±0.1	12.6±0.1	1.9	12.5	14.56±0.01	14.98
		54.6±0.1	13.9±0.2	3. I	13.5	14.39±0.01	
		105.6±2.9	38.6±6.2	3.7	38.4	13.12±0.06	
	oblique3	46.1±0.1	14.2±0.1	2. I	14.0	14.72±0.01	15.45

Table A.25: Run 10 at 100 Myrs

Direction							
		v_c (km s ⁻¹)	$b (\mathrm{km} \mathrm{s}^{-1})$	b_T (km s ⁻¹)	b_{vg} (km s ⁻¹)	$\log N(OVI)$	$\log N(OVI)_{sim}$
у	уı	-7.2±0.2	11.0±0.4	2.2	ю.8	14.27±0.02	14.82
	y2	-4.4±0.1	11.5±0.1	1.9	11.3	14.52±0.01	15.00
	у3	-62.4±1.2	14.3±2.3	9.1	II.O	13.25±0.06	15.07
		-23.0±0.6	18.5±1.1	3.7	18.1	14.08±0.02	
		-0.8±0.2	10.3±0.3	3.0	9.9	14.37±0.02	
Z	ZI	-20.3±2.6	102.3±4.2	25.3	99.1	14.43±0.03	15.79
		4.0±0.2	28.9 ± 0.8	4.0	28.6	15.64±0.01	
	Z2	-73.6±1.7	92.1±3.6	21.4	89.6	13.89±0.01	15.29
		21.0±0.1	п.6±о.і	2. I	II.4	14.53±0.01	
		47.5±0.3	7.1 ± 1.1	3. I	6.4	13.15±0.02	
	Z3	35.7±0.2	18.4±0.4	3.3	18.1	14.86±0.02	14.97
oblique	obliquei	-3.0±0.1	11.1±0.1	2.0	10.9	14.51±0.01	14.84
		30.8±0.3	8.i±0.4	7.3	3.5	13.31±0.02	
	oblique2	1.3±0.1	15.0±0.1	2.0	14.9	14.88±0.01	15.24
	oblique3	-39.5±10.2	59.4±7.9	20.I	55.9	13.69±0.05	15.18
		7.1±0.1	16.5±0.4	3.2	16.2	15.04±0.03	

Table A.26: Run 10 at 150 Myrs

Direction			$\log N(OVI)_{sim}$				
		v_c (km s ⁻¹)	$b ({\rm km \ s^{-1}})$	b_T (km s ⁻¹)	b_{vg} (km s ⁻¹)	$\log N(OVI)$	$ \log I (O V I)_{sim} $
y	уı	2.7±0.1	8.9±0.1	1.7	8.7	14.21±0.00	14.78
	y2	-6.2±0.1	9.2±0.1	2. I	9.0	14.19±0.01	14.69
	у3	-3.4±0.1	12.9±0.3	2. I	12.7	15.08±0.04	15.22
Z	ZI	10.0±1.1	35.I±1.2	3.9	34.9	15.31±0.04	15.97
		11.9±2.7	104.2±8.3	23.5	101.5	14.31±0.06	
		54.7±1.0	19.7±0.9	3.4	19.4	15.04±0.05	
	Z2	22.2±1.4	23.6 ± 2.4	7.3	22.4	14.82 \pm 0.21	14.67
		60.6±2.6	29.4±3.8	7.7	28.4	14.61±0.06	
	Z3	56.7±0.2	12.5±0.2	2.5	12.2	14.58±0.01	15.03
		70.2±0.6	13.1±0.5	3.2	12.7	14.07±0.04	
oblique	obliquei	-5.8±0.1	п.8±о.і	2.2	11.6	14.50±0.00	15.05
		20.4±0.6	12.9±1.2	12.4	3.6	12.38±0.03	
	oblique2	11.3±0.2	11.4±0.3	2.2	II.2	14.42±0.01	14.77
		27.2±0.6	7.3±0.6	2.6	6.8	13.51±0.06	
	oblique3	23.6±0.1	10.3±0.1	2.2	IO.I	14.36±0.01	14.99
		40.0±0.2	7.7±0.3	2.8	7.2	13.47±0.02	

Table A.27: Run 10 at 200 Myrs

Direction			$\log N(OVI)_{sim}$				
		v_c (km s ⁻¹)	$b (\mathrm{km s^{-1}})$	b_T (km s ⁻¹)	b_{vg} (km s ⁻¹)	$\log N(OVI)$	$ \log IV(O V I)_{sim}$
y	yı	-7.6±0.1	16.9±0.1	6.2	15.7	13.18±0.01	14.98
		-2.7±0.1	7.8±0.1	2.0	7.5	14.07±0.01	
	y2	-1.8±0.1	12.2±0.1	2.0	12.0	14.52±0.01	15.18
	у3	-2.6±0.1	8.4±0.1	2.0	8.2	14.15±0.01	14.87
Z	ZI	36.5±5.8	89.5 ± 12.2	29.3	84.6	13.79±0.10	16.38
		50.1±0.1	27.9±0.4	2.5	27.8	16.33±0.05	
	Z2	27.5±2.0	72.4 ± 2.3	25.7	67.7	13.95±0.03	16.21
		33.7±0.5	19.9±0.3	2.6	19.7	15.69±0.04	
		72.I±0.3	16.6±0.2	2.4	16.4	15.18±0.02	
	Z3	24.3±0.2	8.2±0.3	5.7	5.9	14.09±0.02	15.40
		62.0±1.4	37.6±1.5	4.5	37.3	14.55±0.03	
		76.9±0.4	15.0±0.7	4. I	14.4	14.89±0.05	
oblique	obliquei	10.4±0.2	13.3±0.4	2.2	13.1	14.51±0.01	14.61
		31.9±1.4	13.5 ± 2.2	4.5	12.7	13.45±0.08	
	oblique2	16.0±0.1	11.5±0.1	2.0	11.3	14.46±0.01	15.03
	oblique3	21.5±0.1	11.5±0.1	2.0	11.3	14.46±0.01	15.08
		45.0±0.1	6.7±0.1	2.4	6.3	13.50±0.01	

BIBLIOGRAPHY

Ahoranta, J., Finoguenov, A., Bonamente, M., et al. 2021, , 656, A107, doi: 10.1051/0004-6361/202038021

Anders, E., & Grevesse, N. 1989, , 53, 197, doi: 10.1016/0016-7037(89)90286-X

Asplund, M., Grevesse, N., Sauval, A. J., & Scott, P. 2009a, , 47, 481, doi: 10.1146/annurev.astro. 46.060407.145222

-. 2009b, , 47, 481, doi: 10.1146/annurev.astro.46.060407.145222

Begelman, M. C., & Fabian, A. C. 1990, , 244, 26P

Bergvall, N., Zackrisson, E., Andersson, B. G., et al. 2006, , 448, 513, doi: 10.1051/0004-6361: 20053788

Bland-Hawthorn, J., Gallimore, J. F., Tacconi, L. J., et al. 1997, , 248, 9, doi: 10.1023/A: 1000567831370

Bordoloi, R., Wagner, A. Y., Heckman, T. M., & Norman, C. A. 2017, , 848, 122, doi: 10.3847/1538-4357/aa8e9c

Bruhweiler, F. C., Truong, K. Q., & Altner, B. 1991, , 379, 596, doi: 10.1086/170532

Cashman, F. H., Fox, A. J., Wakker, B. P., et al. 2023, , 944, 65, doi: 10.3847/1538-4357/acaaa5

Chung, H., Vargas, C. J., & Hamden, E. 2021, , 916, 7, doi: 10.3847/1538-4357/ac04af

Collins, J. A., Shull, J. M., & Giroux, M. L. 2007, , 657, 271, doi: 10.1086/510770

Cox, A. 2000, Allen's astrophysical quantities; 4th ed. (New York, NY: AIP), doi: 10.1007/978-1-4612-1186-0

Daddi, E., Elbaz, D., Walter, F., et al. 2010, , 714, L118, doi: 10.1088/2041-8205/714/1/L118

Di Matteo, T., Springel, V., & Hernquist, L. 2005, , 433, 604, doi: 10.1038/nature03335

Dixon, W. V. D., Sankrit, R., & Otte, B. 2006, , 647, 328, doi: 10.1086/505168

Drazin, P. G. 2002, Introduction to Hydrodynamic Stability, Cambridge Texts in Applied Mathematics (Cambridge University Press), doi: 10.1017/CB09780511809064

Engelbracht, C. W., Rieke, G. H., Gordon, K. D., et al. 2008, , 678, 804, doi: 10.1086/529513

Esquivel, A., Benjamin, R. A., Lazarian, A., Cho, J., & Leitner, S. N. 2006, , 648, 1043, doi: 10.1086/

Evans, D. A., Ogle, P. M., Marshall, H. L., et al. 2010, in Astronomical Society of the Pacific Conference Series, Vol. 427, Accretion and Ejection in AGN: a Global View, ed. L. Maraschi, G. Ghisellini, R. Della Ceca, & F. Tavecchio, 97, doi: 10.48550/arXiv.0910.3023

Ferland, G. J., Chatzikos, M., Guzmán, F., et al. 2017, , 53, 385, doi: 10.48550/arXiv.1705.10877

Field, G. B., & Steigman, G. 1971, , 166, 59, doi: 10.1086/150941

Fielding, D. B., Ostriker, E. C., Bryan, G. L., & Jermyn, A. S. 2020, , 894, L24, doi: 10.3847/2041-8213/ab8d2c

Fox, A. J., Richter, P., Ashley, T., et al. 2019, , 884, 53, doi: 10.3847/1538-4357/ab40ad

Fox, A. J., Richter, P., Wakker, B. P., et al. 2013a, , 772, 110, doi: 10.1088/0004-637X/772/2/110

—. 2013b, The Messenger, 153, 28

Fox, A. J., Savage, B. D., & Wakker, B. P. 2006, , 165, 229, doi: 10.1086/504800

Fox, A. J., Savage, B. D., Wakker, B. P., et al. 2004, , 602, 738, doi: 10.1086/381024

Fox, A. J., Wakker, B. P., Savage, B. D., et al. 2005a, , 630, 332, doi: 10.1086/431915

—. 2005b, , 630, 332, doi: 10.1086/431915

Fox, A. J., Wakker, B. P., Smoker, J. V., et al. 2010a, , 718, 1046, doi: 10.1088/0004-637X/718/2/1046

—. 2010b, , 718, 1046, doi: 10.1088/0004-637X/718/2/1046

Fox, A. J., Lehner, N., Lockman, F. J., et al. 2016, , 816, L11, doi: 10.3847/2041-8205/816/1/L11

Fryxell, B., Olson, K., Ricker, P., et al. 2000a, , 131, 273, doi: 10.1086/317361

—. 2000b, , 131, 273, doi: 10.1086/317361

Fukugita, M., Hogan, C. J., & Peebles, P. J. E. 1998, , 503, 518, doi: 10.1086/306025

Fukugita, M., & Kawasaki, M. 2003, , 340, L7, doi: 10.1046/j.1365-8711.2003.06507.x

Galyardt, J., & Shelton, R. L. 2016, , 816, L18, doi: 10.3847/2041-8205/816/1/L18

Ganguly, R., Sembach, K. R., Tripp, T. M., & Savage, B. D. 2005, , 157, 251, doi: 10.1086/428350

Gnat, O., & Sternberg, A. 2007a, , 168, 213, doi: 10.1086/509786

—. 2007b, , 168, 213, doi: 10.1086/509786

Goetz, E., Wang, C., & Shelton, R. L. 2024a, , 960, 66, doi: 10.3847/1538-4357/ad0df7

—. 2024b, , 960, 66, doi: 10.3847/1538-4357/ad0df7

Grimes, J. P., Heckman, T., Hoopes, C., et al. 2006, , 648, 310, doi: 10.1086/505680

Grimes, J. P., Heckman, T., Strickland, D., & Ptak, A. 2005, , 628, 187, doi: 10.1086/430692

Grimes, J. P., Heckman, T., Strickland, D., et al. 2007, , 668, 891, doi: 10.1086/521353

Grimes, J. P., Heckman, T., Aloisi, A., et al. 2009, , 181, 272, doi: 10.1088/0067-0049/181/1/272

Gritton, J. A., Shelton, R. L., & Galyardt, J. E. 2017, , 842, 102, doi: 10.3847/1538-4357/aa756d

Gritton, J. A., Shelton, R. L., & Kwak, K. 2014a, , 795, 99, doi: 10.1088/0004-637X/795/1/99

—. 2014b, 795, 99, doi: 10.1088/0004-637X/795/1/99

Grønnow, A., Tepper-García, T., Bland-Hawthorn, J., & McClure-Griffiths, N. M. 2017, , 845, 69, doi: 10.3847/1538-4357/aa7ed2

Guo, J., Wu, J., Feng, H., et al. 2023, , 946, 72, doi: 10.3847/1538-4357/acaddd

Hafen, Z., Faucher-Giguère, C.-A., Anglés-Alcázar, D., et al. 2019, , 488, 1248, doi: 10.1093/mnras/stz1773

Haislmaier, K. J., Tripp, T. M., Katz, N., et al. 2021, , 502, 4993, doi: 10.1093/mnras/staa3544

Harrison, C. M. 2017, Nature Astronomy, 1, 0165, doi: 10.1038/s41550-017-0165

Hayes, M., Melinder, J., Östlin, G., et al. 2016, , 828, 49, doi: 10.3847/0004-637X/828/1/49

Heckman, T., Borthakur, S., Wild, V., Schiminovich, D., & Bordoloi, R. 2017, , 846, 151, doi: 10.3847/1538-4357/aa80dc

Heckman, T. M., Armus, L., & Miley, G. K. 1990, , 74, 833, doi: 10.1086/191522

Heckman, T. M., Norman, C. A., Strickland, D. K., & Sembach, K. R. 2002a, , 577, 691, doi: 10.1086/

—. 2002b, , 577, 691, doi: 10.1086/342232

Heckman, T. M., Sembach, K. R., Meurer, G. R., et al. 2001, , 554, 1021, doi: 10.1086/321422

Henley, D. B., Gritton, J. A., & Shelton, R. L. 2017, , 837, 82, doi: 10.3847/1538-4357/aa5df7

Henley, D. B., & Shelton, R. L. 2015, , 808, 22, doi: 10.1088/0004-637X/808/1/22

Hodges-Kluck, E. J., Bregman, J. N., & Li, J.-t. 2018, , 866, 126, doi: 10.3847/1538-4357/aae38a

Holweger, H. 2001, in American Institute of Physics Conference Series, Vol. 598, Joint SOHO/ACE workshop "Solar and Galactic Composition", ed. R. F. Wimmer-Schweingruber, 23–30, doi: 10. 1063/1.1433974

Hoopes, C. G., Heckman, T. M., Strickland, D. K., & Howk, J. C. 2003, , 596, L175, doi: 10.1086/

Hoopes, C. G., Heckman, T. M., Salim, S., et al. 2007, , 173, 441, doi: 10.1086/516644

Howk, J. C., Wotta, C. B., Berg, M. A., et al. 2017, , 846, 141, doi: 10.3847/1538-4357/aa87b4

Hummels, C. B., Smith, B. D., & Silvia, D. W. 2017, , 847, 59, doi: 10.3847/1538-4357/aa7e2d

Ji, S., Oh, S. P., & Masterson, P. 2019, , 487, 737, doi: 10.1093/mnras/stz1248

Kaiser, M. E., Kruk, J., Ake, T., et al. 2009, FUSE Archival Instrument Handbook. https://archive.stsci.edu/fuse/ih.html

Karachentsev, I. D., Karachentseva, V. E., Huchtmeier, W. K., & Makarov, D. I. 2004, , 127, 2031, doi: 10. 1086/382905

Kaufman, V., & Martin, W. C. 1989, Journal of the Optical Society of America B Optical Physics, 6, 1769, doi: 10.1364/JOSAB.6.001769

Kennicutt, Robert C., J. 1998, , 498, 541, doi: 10.1086/305588

Kwak, K., Henley, D. B., & Shelton, R. L. 2011, , 739, 30, doi: 10.1088/0004-637X/739/1/30

Kwak, K., & Shelton, R. L. 2010a, , 719, 523, doi: 10.1088/0004-637X/719/1/523

—. 2010b, , 719, 523, doi: 10.1088/0004-637X/719/1/523

Kwak, K., Shelton, R. L., & Raley, E. A. 2009, , 699, 1775, doi: 10.1088/0004-637X/699/2/1775

Lehner, N., & Howk, J. C. 2007, 377, 687, doi: 10.1111/j.1365-2966.2007.11631.x

Lehnert, M. D., & Heckman, T. M. 1996, , 462, 651, doi: 10.1086/177180

Lehnert, M. D., Heckman, T. M., & Weaver, K. A. 1999, , 523, 575, doi: 10.1086/307762

Lopez-Rodriguez, E., Guerra, J. A., Asgari-Targhi, M., & Schmelz, J. T. 2021, , 914, 24, doi: 10.3847/ 1538-4357/abf934

Marasco, A., Fraternali, F., Lehner, N., & Howk, J. C. 2022, 515, 4176, doi: 10.1093/mnras/stac1172

Meurer, G. R., Heckman, T. M., Lehnert, M. D., Leitherer, C., & Lowenthal, J. 1997, , 114, 54, doi: 10. 1086/118452

Miller, M. J., & Bregman, J. N. 2015, , 800, 14, doi: 10.1088/0004-637X/800/1/14

Miller, M. J., Hodges-Kluck, E. J., & Bregman, J. N. 2016, , 818, 112, doi: 10.3847/0004-637X/818/2/

Mishra, S., Fox, A. J., Smoker, J. V., Lucchini, S., & D'Onghia, E. 2025, , 984, 104, doi: 10.3847/1538-4357/adc68a

Moran, E. C., & Lehnert, M. D. 1997, , 478, 172, doi: 10.1086/303795

Morton, D. C. 1991, , 77, 119, doi: 10.1086/191601

Müller Sánchez, F., Davies, R. I., Genzel, R., et al. 2009, , 691, 749, doi: 10.1088/0004-637X/691/1/749

Nidever, D. L., Majewski, S. R., Butler Burton, W., & Nigra, L. 2010, , 723, 1618, doi: 10.1088/0004-637X/723/2/1618

Ogle, P. M., Brookings, T., Canizares, C. R., Lee, J. C., & Marshall, H. L. 2003, , 402, 849, doi: 10.1051/0004-6361:20021647

Otte, B., Murphy, E. M., Howk, J. C., et al. 2003, , 591, 821, doi: 10.1086/375535

Plöckinger, S., & Hensler, G. 2012, , 547, A43, doi: 10.1051/0004-6361/201218767

Putman, M. E., Peek, J. E. G., & Joung, M. R. 2012, , 50, 491, doi: 10.1146/annurev-astro-081811-125612

Qu, Z., Chen, H.-W., Johnson, S. D., et al. 2024, , 968, 8, doi: 10.3847/1538-4357/ad410b

Radburn-Smith, D. J., de Jong, R. S., Seth, A. C., et al. 2011, , 195, 18, doi: 10.1088/0067-0049/195/2/18

Richter, P. 2017, in Astrophysics and Space Science Library, Vol. 430, Gas Accretion onto Galaxies, ed. A. Fox & R. Davé, 15, doi: 10.1007/978-3-319-52512-9_2

Richter, P., Savage, B. D., Sembach, K. R., & Tripp, T. M. 2006, , 445, 827, doi: 10.1051/0004-6361: 20053636

Richter, P., Savage, B. D., Tripp, T. M., & Sembach, K. R. 2004, 153, 165, doi: 10.1086/421297

Richter, P., Sembach, K. R., Wakker, B. P., et al. 2001, , 559, 318, doi: 10.1086/322401

Richter, P., Nuza, S. E., Fox, A. J., et al. 2017, , 607, A48, doi: 10.1051/0004-6361/201630081

Rickman, E., & Brown, J. 2024, in STIS Instrument Handbook for Cycle 33 v. 24, Vol. 24, 24

Rico-Villas, F., Martín-Pintado, J., González-Alfonso, E., et al. 2021, , 502, 3021, doi: 10.1093/mnras/stab197

Sakai, S., & Madore, B. F. 1999, , 526, 599, doi: 10.1086/308032

Sánchez-García, M., García-Burillo, S., Pereira-Santaella, M., et al. 2022, , 660, A83, doi: 10.1051/0004-6361/202142396

Sander, B., & Hensler, G. 2021, , 501, 5330, doi: 10.1093/mnras/staa3952

Savage, B. D., Kim, T. S., Wakker, B. P., et al. 2014, , 212, 8, doi: 10.1088/0067-0049/212/1/8

Savage, B. D., Sembach, K. R., Wakker, B. P., et al. 2003, , 146, 125, doi: 10.1086/346229

Scoville, N., Sheth, K., Aussel, H., et al. 2016, , 820, 83, doi: 10.3847/0004-637X/820/2/83

Sembach, K. R., Tripp, T. M., Savage, B. D., & Richter, P. 2004, , 155, 351, doi: 10.1086/425037

Sembach, K. R., Wakker, B. P., Savage, B. D., et al. 2003a, 146, 165, doi: 10.1086/346231

—. 2003b, , 146, 165, doi: 10.1086/346231

Seth, A. C., Dalcanton, J. J., & de Jong, R. S. 2005, , 129, 1331, doi: 10.1086/427859

Shelton, R. L., Kruk, J. W., Murphy, E. M., et al. 2001, , 560, 730, doi: 10.1086/322478

Shull, J. M., Smith, B. D., & Danforth, C. W. 2012, 759, 23, doi: 10.1088/0004-637X/759/1/23

Shull, J. M., Stevans, M., Danforth, C., et al. 2011, , 739, 105, doi: 10.1088/0004-637X/739/2/105

Springel, V., Di Matteo, T., & Hernquist, L. 2005, , 361, 776, doi: 10.1111/j.1365-2966.2005.

Stocke, J. T., Keeney, B. A., Danforth, C. W., et al. 2019, , 240, 15, doi: 10.3847/1538-4365/aaf73d

Strickland, D. K., Heckman, T. M., Colbert, E. J. M., Hoopes, C. G., & Weaver, K. A. 2004, , 151, 193, doi: 10.1086/382214

Sutherland, R. S., & Dopita, M. A. 1993a, , 88, 253, doi: 10.1086/191823

—. 1993b, , 88, 253, doi: 10.1086/191823

Tosi, M., Sabbi, E., Bellazzini, M., et al. 2001, 122, 1271, doi: 10.1086/322104

Tripp, T. M. 2022, 511, 1714, doi: 10.1093/mnras/stac044

Tripp, T. M., & Savage, B. D. 2000, , 542, 42, doi: 10.1086/309506

Tripp, T. M., Savage, B. D., & Jenkins, E. B. 2000, , 534, Li, doi: 10.1086/312644

Tripp, T. M., Sembach, K. R., Bowen, D. V., et al. 2008a, , 177, 39, doi: 10.1086/587486

—. 2008b, , 177, 39, doi: 10.1086/587486

Tripp, T. M., Wakker, B. P., Jenkins, E. B., et al. 2003, , 125, 3122, doi: 10.1086/374995

Troitsky, S. 2017, , 468, L36, doi: 10.1093/mnrasl/slx022

Tully, R. B. 1988, Nearby galaxies catalog

Tully, R. B., Rizzi, L., Shaya, E. J., et al. 2009, 138, 323, doi: 10.1088/0004-6256/138/2/323

Tumlinson, J., Peeples, M. S., & Werk, J. K. 2017, , 55, 389, doi: 10.1146/annurev-astro-091916-055240

Tumlinson, J., Thom, C., Werk, J. K., et al. 2011, Science, 334, 948, doi: 10.1126/science.1209840

Turk, M. J., Smith, B. D., Oishi, J. S., et al. 2011, The Astrophysical Journal Supplement Series, 192, 9, doi: 10.1088/0067-0049/192/1/9

Vacca, W. D., Hamilton, R. T., Savage, M., et al. 2015, , 804, 66, doi: 10.1088/0004-637X/804/1/66

Wakker, B. P., & Savage, B. D. 2009, , 182, 378, doi: 10.1088/0067-0049/182/1/378

Wakker, B. P., & van Woerden, H. 1997, 35, 217, doi: 10.1146/annurev.astro.35.1.217

Wakker, B. P., Howk, J. C., Savage, B. D., et al. 1999, , 402, 388, doi: 10.1038/46498

Wakker, B. P., Savage, B. D., Sembach, K. R., et al. 2003, , 146, 1, doi: 10.1086/346230

Wakker, B. P., York, D. G., Howk, J. C., et al. 2007, , 670, L113, doi: 10.1086/524222

Werk, J. K., Prochaska, J. X., Cantalupo, S., et al. 2016, , 833, 54, doi: 10.3847/1538-4357/833/1/54

Wilson, A. S., Elvis, M., Lawrence, A., & Bland-Hawthorn, J. 1992, , 391, L75, doi: 10.1086/186402

Wilson, A. S., & Ulvestad, J. S. 1987, , 319, 105, doi: 10.1086/165436

Yao, Y., Shull, J. M., & Danforth, C. W. 2011a, , 728, L16, doi: 10.1088/2041-8205/728/1/L16

—. 2011b, , 728, L16, doi: 10.1088/2041-8205/728/1/L16

Yoon, J. H., Martin, C. L., Veilleux, S., et al. 2021, , 502, 969, doi: 10.1093/mnras/staa3583

Yoshida, M., Kawabata, K. S., & Ohyama, Y. 2011, , 63, 493, doi: 10.1093/pasj/63.sp2.S493

Young, A. J., Wilson, A. S., & Shopbell, P. L. 2001, , 556, 6, doi: 10.1086/321561

Zech, W. F., Lehner, N., Howk, J. C., Dixon, W. V. D., & Brown, T. M. 2008, , 679, 460, doi: 10.1086/

Zheng, W., Kriss, G. A., Wang, J. X., et al. 2009, in American Institute of Physics Conference Series, Vol. 1135, Future Directions in Ultraviolet Spectroscopy: A Conference Inspired by the Accomplishments of the Far Ultraviolet Spectroscopic Explorer Mission, ed. M. E. van Steenberg, G. Sonneborn, H. W. Moos, & W. P. Blair, 52–54, doi: 10.1063/1.3154085

Zheng, W., Wang, J.-X., Kriss, G. A., et al. 2008, , 686, 881, doi: 10.1086/591547